Alma Mater Studiorum · Università di Bologna

Scuola di Scienze
Corso di Laurea Magistrale in Fisica del Sistema Terra

Role of Transient Deformation in Glacial Isostatic Adjustment

Relatore:
Prof. Giorgio Spada

Correlatore:
Dott. Daniele Melini

Presentata da:
Anastasia Consorzi

Sessione II

Anno Accademico 2020/2021

Sommario

L'aggiustamento isostatico post-Glaciale (in inglese Glacial Isostatic Adjustment, o GIA) è uno dei fenomeni principi della geofisica alle basse frequenze. Esso consiste nella deformazione della superficie terrestre e del geoide in seguito allo scioglimento di masse ghiacciate. Studiando il GIA i geofisici sono in grado di determinare le caratteristiche salienti dell'interno della Terra, risolvendo un problema inverso in cui le variabili note sono le deformazioni osservate, mentre le incognite sono la struttura interna della Terra e la descrizione spazio-temporale dello scioglimento del ghiaccio. Tuttavia, per la natura stessa dei problemi inversi, è estremamente difficile ottenere una soluzione unica; inoltre, numerosi fenomeni geofisici di diversa natura "inquinano" i dati di spostamento, rendendo la risoluzione di tale problema estremamente complessa.

In questa tesi studierò quali conseguenze comporta, in termini di spostamento atteso, l'assunzione di un modello reologico con un transiente nel mantello terrestre. Nelle reologie transienti la risposta di un corpo a sollecitazioni esterne varia nel tempo: inizialmente si nota una risposta rapida, che progressivamente si esaurisce, lasciando il posto ad una risposta stazionaria. La scelta della reologia transiente è ricaduta sul modello di Andrade, introdotto dall'omonimo fisico nel 1910 per descrivere la deformazione di alcuni materiali poli-cristallini ad alta temperatura, ed attualmente utilizzata per lo studio delle defromazioni planetarie. Ovviamente, per caratterizzare Andrade, avremo bisogno di considerare altre reologie, perciò anche altri modelli reologici saranno esaminati, con particolare uso di quello di Maxwell. Tale scelta è motivata dal fatto che, nella risoluzione classica del problema del GIA, quando non si considera la possibilità di effetti transienti nel mantello, si usa descriverne il comportamento tramite il corpo di Maxwell. Al contrario, quando gli effetti transienti sono considerati, in letteratura si è fatto largo uso del modello di Burgers.

Alla conoscenza del relatore e dell'autrice di questa tesi, non risulta in letteratura nessuna descrizione esplicita, in termini di numeri di Love, del rilassamento post-glaciale di una Terra omogenea (sfera di Kelvin) con reologia di Andrade. Per questo motivo in questa tesi si indagherà proprio tale possibilità.

Lo scopo principale che vuole adempiere questo lavoro è determinare, dopo averne ben descritto le caratteristiche principali, come i profili di spostamento generati da modelli di Terra che considerano reologie transienti (Andrade) nel mantello, si discostano da modelli in cui sono presenti reologie steady-state; soprattutto si vuole cercare di capire in che momento della simulazione, e in che punto della superficie della terra rispetto alla massa ghiacciata considerata, gli effetti transienti sono meglio distinguibili. Verranno considerate sia deformazioni dovute a glaciazioni passate, sia quelle dovute all'attuale cambiamento climatico.

Abstract

Glacial Isostatic Adjustment (GIA) is one of the most important phenomena of low frequency geophysics. It consists in the deformation of the Earth's surface and the geoid in response to ice-sheets melting. By studying GIA, geophysicists are able to infer the main characteristics of the Earth's interior, by solving an inverse problem whose known variables are the observed surface displacements, while the unknowns are the Earth's internal structure and the space-temporal ice melting description. Nevertheless, by the nature of inverse problems, it is extremely difficult to obtain a unique solution; moreover, a vast number of diverse geophysical phenomena taints displacement data, making the resolution of the problem very complicated.

In this thesis I will study the consequences, in terms of displacement, that the assumption of a model with a transient rheology in the Earth's mantle entails. In transient rheologies the response of a body to external factors varies with time: at the beginning, a fast response occurs, but it decreases progressively over time. In this thesis I will consider Andrade's transient rheology, introduced in 1910 by the homonymous physicist to describe the deformation of some poly-crystalline materials at high temperatures, and currently used for the study of planetary deformations. In order to characterize Andrade rheology, we will need to compare it with other rheologies, especially Maxwell body. This choice is motivated by the fact that, in classical GIA problems, when the possibility of transient effects in the mantle is discarded, the Maxwell body is the one generally used. On the contrary, when the effects of a transient are considered, the Burgers body is the one usually adopted in literature.

To the knowledge of the supervisor and the author of this thesis, an explicit description, in terms of Love numbers, of the post-glacial relaxation of an homogeneous (Kelvin's sphere) Earth with Andrade rheology, does not exist. For this reason, in this thesis, I will investigate this possibility.

The main purpose of this work is to determine how displacement profiles generated by Earth model which consider transient rheologies in the mantle differ from models in which steady-state rheologies are accounted. We would like to understand at which moment of the simulation, and in which position with respect the considered ice load, the

effects of the transient rheology will be better discernible from those due to steady-state rheologies. Both the cases of deformation due to past deglaciations and those due to present-day climate change will be taken into account.

Contents

Motivations **3**

1 Basic rheological laws **5**
1.1 The compositional structure of the Earth 5
1.2 A few words about rheology 7
1.3 Correspondence Principle 20
1.4 Earth rheological Structure 21
1.5 The problem of Mantle rheology 23
1.6 Andrade Rheology 25

2 Love Numbers **30**
2.1 The origin of Love numbers 30
2.2 Elastic Load Love Numbers 32
2.3 Viscoelastic Load Love Numbers 37
2.4 Generic Heaviside Load Love Numbers 38
2.5 Analytical form of Load Love Numbers 42
2.6 Andrade's Load Love numbers for the Kelvin's Sphere 46

3 `ALMA`: the planetary Love Numbers calculator **48**
3.1 Viscoelastic normal Mode: theory and drawbacks 49
3.2 The Post-Widder-Gaver method 52
3.3 `ALMA`: some details 53
3.4 Computing Love numbers with `ALMA` 55

4 Surface Loads: modelling Glacial Isostatic Adjustment **67**
4.1 Surface Response Function 69
4.2 Surface Response Function for axis-symmetric loads 76
4.3 Surface Response Function for disc loads 79

5 Results of the simulations **82**
5.1 Experiment 1: Heaviside time-history, 3-layer Earth 82
5.2 Experiment 2: realistic step-function time-history, 3-layer Earth 91
5.3 Experiment 3: 2-layer Mantle 96
5.4 Experiment 4: present day ice melting 107

6 Conclusions **116**

Bibliografia **121**

Motivations

In 1731, A. Celsius marked on a costal rock at Lovgrund, Sweden, the sea level. There the uplift of Earth's surface was a well known phenomenon, but we ought to Celsius the first scientific measurement. The mark is still visible and almost 1.7 m over current sea level. During those years, many scholars explored a number of explanations for the change in the height of the land, and the idea that an ice sheet could have depressed it was first proposed by Jamieson (1865) [1, 2]. Nowadays we are aware that what Celsius and the Sweden population were experiencing, were the effects of Glacial Isostatic Adjustment (GIA).

In the last fifty years, our knowledge in terms of GIA has progressed considerably, thanks to the work of many scientists and to the technological innovation. Now we know that the surface deformation measured in many lands, especially at the high latitudes, is due to the viscoelastic response of the Earth under the effect of the ancient ice-sheets melting, that occurred thousands of years ago. Indeed, the weight of an ice sheet is able to depress the solid Earth below it and also to deform the neighbouring areas. This is due to the rheology of Earth's interior: the lithosphere, that we can consider as a thin and elastic superficial layer, bends and, if time is sufficient, the material in the mantle, that for long time-scales could be defined as a viscoelastic body, flees from the position of the applied load to its neighbours, creating a sort of swelling called "*forebulge*".

GIA is a topic of fundamental importance in Geophysics not only because it allows us to deepen our knowledge of the cryosphere-geosphere interactions, but also (and especially) because it offers the possibility to study the Earth rheological response on intermediate and long time scales. It is often confused with Post Glacial Rebound (PGR), while, actually, PGR, the movement of the Earth's crust in response to the melting of continental ice sheets, represents only one of its numerous aspects. GIA includes indeed a wide range of phenomena connected to the loading and unloading of the Earth's surface

caused by the periodical variation of continental ice masses, such as global and regional temporal variations of the Earth's gravity field, fluctuations of the Earth's rotation axis, or the sea level change [1].

The most common viscoelastic body, and even one of the most used to model the Earth's mantle in GIA problems, is the Maxwell body. It exhibits, after the action of a constant stress, an instantaneous elastic deformation followed by a constant strain rate, called steady-state creep [3, 4].

Since the late 1970s, satellite measurements allow scientists to deepen the analysis of GIA effects. However, several inconsistencies that arose from this new data instilled in some of them the doubt that the observed deformations where not the result of the action of a steady state response, and the idea that "*transient effects*" must be considered started peeking out. A transient in rheology is a time dependent-behaviour, that marks the passage from a regime (like the instantaneous elastic response), to another (like the steady state-creep).

There exists in literature many examples of rheologies which account for a transient stage, like that of Burgers, but to probe new possibilities I will focus the attention upon the Andrade's rheology, widely used in the study of tidal deformation, but not much in the field of load deformations. This choice is motivated by the fact that it represents a more realistic rheological model than the Burgers body, since it has actually been observed in experiments on metals and polycrystalline materials at high temperature [5]. Nevertheless, a fully analytical approach is not possible for Andrade's rheology. The work of this thesis will investigate if this rheological model is able to represent well the observed deformation, focusing the attention not only on the physics that this hypothesis involves, but also on another important question: if a transient effect is indeed present, are we able to see it by observing GIA at the Earth's surface ?

Chapter 1

Basic rheological laws

This chapter is a brief introduction regarding basic Earth's rheological properties, drawing inspiration from [6] and [7]. After few words about the Earth's compositional structure, I will introduce some aspects of rheology which are essential for the following chapters of this thesis. Basic rheological models will be analysed, with the aim of defining a rheological stratification for the Earth. After a brief discussion about the problem of mantle rheology, and the actual presence of a transient, Andrade rheological model will be introduced.

1.1 The compositional structure of the Earth

The Earth is the third planet of the Solar System. It belongs to the family of the rocky planets, and following the *nebular theory*, it generated by the union of planetesimals by accretion. Then the gravitational differentiation, the energy released from the impact of meteors and from the radioactive decay were able to warm the planet until the complete fusion. The lighter elements and the ones with low melting point migrated to the surface of the liquid planet, forming the crust once the temperatures cooled; the heavier elements, like iron and nickel, were further pushed towards the interior. This explains why the Earth appears layered in mineralogical terms [8].

The compositional layers are:

- **Crust** - composed mainly by silicon oxide, Al, Na and K. It separated by the mantle by the so called *Mohorovicic discontinuity*, (or *Moho*), depth at which seismologists

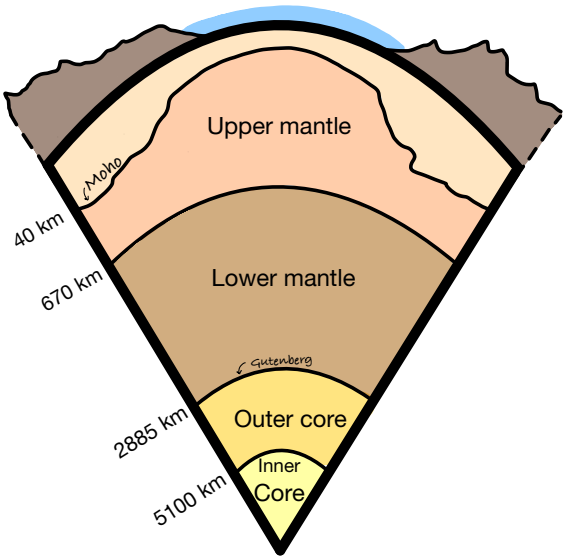

Figure 1.1: Earth's compositional structure. *Adapted from [7].*

register a sharp increase in the seismic wave velocity. One can distinguish the continental crust, with a mean thickness of 30 km, and a oceanic crust, only 10 km thick. The continental crust can be split as well into two components: a superficial one, mostly composed by granite, and a deeper one, mainly basaltic. In general, the crust mean density is less than 3000 kg/m^3 [7].

- **Mantle** - below the Moho, we find the mantle, a layer that extends until a depth of 2885 km. We can distinguish an upper mantle (from the moho to 670 km), hosting mainly phase transitions of silicates, whose most common is olivine, and a lower part (from 670 km to 2885 km), more homogeneous and mainly composed of iron oxides, Si and Mg [7].

- **Core** - at depth of 2885 km, the Gutenberg discontinuity marks the boundary between the mantle and the core. Also the core is divided into two portions at a depth of 5100 km: the external one, the outer core, is fluid, and composed of Fe and other lighter elements, and the internal core, solid, composed of Fe and Ni [7].

Knowing the composition of Earth's interior is fundamental for many reasons, but as regard the work of this thesis, considering its mechanical and dynamical behaviour is more suitable. That's why I will present, in the next section, an alternative Earth's structure,

called "*rheological structure*". But first, a few introductory words about rheology.

1.2 A few words about rheology

Rheology is a interdisciplinary science that studies the deformation and flow of materials. From the Greek $\rho\acute{\epsilon}\omega$ - flow - and $\lambda o\gamma\acute{\iota}\alpha$ - study of - it literally means study of the flow. The rheology of a material does not depend only on its characteristics or its atomic structure, but also on external parameters like temperature, pressure, and especially time. In rheology, the terms *solid* and $fluid$ take a different meaning with respect the common use: a material is fluid when under a given *stress* is able to $flow$ [3].

The main purpose in rheology is to write the so called *constitutive equations*, mathematical relationships that express the deformation that a body undergoes in response to a given stress. The deformation - strain - (indicated by ϵ) is a kinematic quantity that describes the changes in shape and volume of a continuum. The *stress* τ is a dynamical quantity connected to the traction exerted on the body. Stress and strain are not the only terms that appear in a constitutive equation: with them we find often the intrinsic material parameters (such as the viscosity η, the rigidity μ and others). Generally, a constitutive equation has the form [9]:

$$\mathcal{R}(\epsilon, \dot{\epsilon}, \ddot{\epsilon}; \tau, \dot{\tau}, \ddot{\tau}, \{P\}) = 0 \tag{1.1}$$

where $\mathcal{R}$ is called "*rheological function*", and $\{P\}$ refers to the intrinsic material parameters.

In rheology there are two possible approaches [3]: a solid-state one, in which from considerations regarding how particles are dispose and how they move in the lattice, it is possible to determine the constitutive equations, and the continuum mechanics approach, where the rheological properties of materials are deduced macroscopically and phenomenologically. For the topics that will be presented in this thesis, I will consider only the second approach. There is a vast variety of rheological behaviours; the most common rheological laws are Hooke's law (elasticity), Newtonian law (viscous fluids) and the Maxwell law for visco-elastic materials. However, other important laws exist, of importance for this thesis.

In order to define the rheology of a material, several reference tests can be established:

Creep Test

In a creep test, the stress $\sigma(t)$ is applied at time $t = 0$ and it is held constant afterwards: $\sigma(t) = \sigma_0 H(t)$, where σ_0 is a constant stress and $H(t)$ is the Heaviside's function. In general, the response of materials to a creep test can be split in three steps: a primary creep (or a *transient* creep), a secondary creep, or a *steady - state* creep and a tertiary creep, which precede the fracture. During all this time the strain is a non-decreasing function [9].

Stress-relaxation Test

In a relaxation test, the strain $\epsilon(t)$ is applied at time $t = 0$ and it is held constant afterwards: $\epsilon(t) = \epsilon_0 H(t)$, where ϵ_0 is a strain constant value. Typically, the stress decays with time: the phenomenon is known as "*stress relaxation*" [9].

Stress-recovery Test

In a stress-recovery test, a constant stress σ_0 is applied at a time $t = t_1$ and held constant until time $t = t_2 = t_1 + T$, where $T > 0$ is the duration of the test. Thus, the stress is: $\sigma(t) = \sigma_0(H(t - t_1) - H(t - t_2))$. This is a variant of the creep test, in which the material is loaded and subsequently un-loaded [9].

Cyclic Test

In a cyclic test, for $t \geqslant 0$ the stress is imposed to vary with time according to a harmonic function $\sigma(t) = \sigma_0 H(t) \sin(\omega t + \phi)$. For a general (inelastic) rheology, a phase lag δ is observed between strain and stress, physically associated with the energy dissipation within the continuum [9].

On the basis of the response to these tests, we can gather materials into classes. Here is a brief description of the main ones: linear elasticity, newtonian fluids and, as regard viscoelasticity, I will consider the Maxwell body, the Kelvin-Voigt body and the Burgers body.

Linear Elasticity

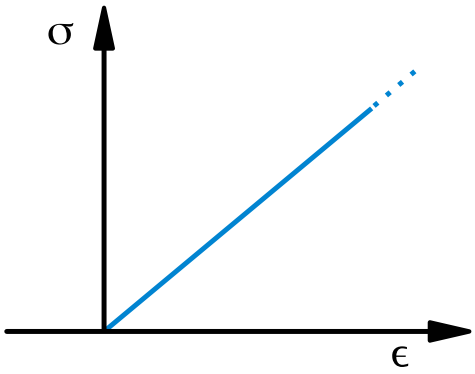

Figure 1.2: In linear elasticity, the relationship between strain and stress is linear.

Hooke's law of linear elasticity

$$\sigma_{ij} = C_{ijkl}\epsilon_{kl} \tag{1.2}$$

was the first written constitutive equation. Here is reported in the continuous mechanics form, were σ_{ij} is the stress tensor, C_{ijkl} the elastic constants tensor and ϵ_{ij} is the strain. Linear elastic materials deform proportionally to the applied stress (Figure 1.2), and once the external force is removed, they recover totally, coming back to the unperturbed state. Basically, almost all solid bodies exhibit elastic deformation under small and short-time stresses. In rheology the linear elasticity is represented with a spring.

Let's consider the response of a linear elastic body in a creep test. In one dimension, since $\sigma(t) = \sigma_0 H(t)$, from the 1D constitutive equation $\sigma = \mu\epsilon$, were μ is the elastic rigidity, we obtain

$$\sigma_0 H(t) = \mu\epsilon \quad \Rightarrow \quad \epsilon = \frac{\sigma_0}{\mu} \quad for\ t \geqslant 0 \tag{1.3}$$

In a stress-relaxation test we have $\epsilon(t) = \epsilon_0 H(t)$, hence we obtain

$$\sigma = \mu\epsilon_0 H(t) \quad \Rightarrow \quad \sigma = \epsilon_0\mu \quad for\ t \geqslant 0. \tag{1.4}$$

For a visualisation of these two results see Figure 1.3 and 1.4.

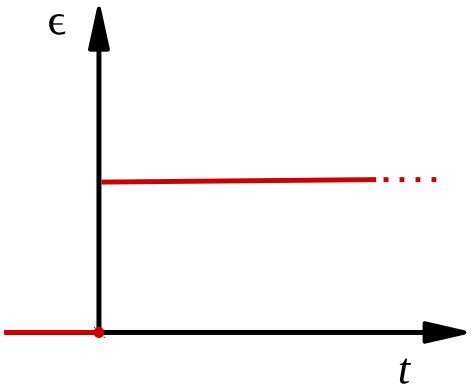

Figure 1.3: sketch representation of the result of a creep test on a linear elastic material. The strain remains constant at the value $\epsilon = \frac{\sigma_0}{\mu}$ since the stress is applied.

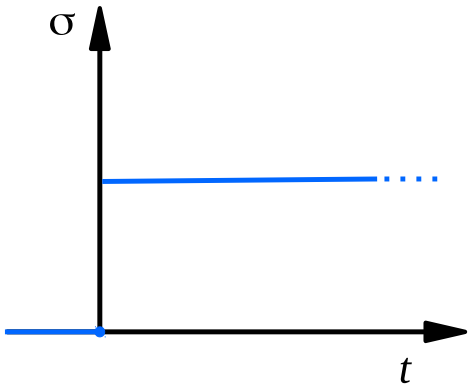

Figure 1.4: Sketch representation of the result of a a stress-relaxation test on a linear elastic material. In this case, it is the stress that remains constant at the value $\sigma = \epsilon_0 \mu$ since the strain is applied.

Newtonian fluids

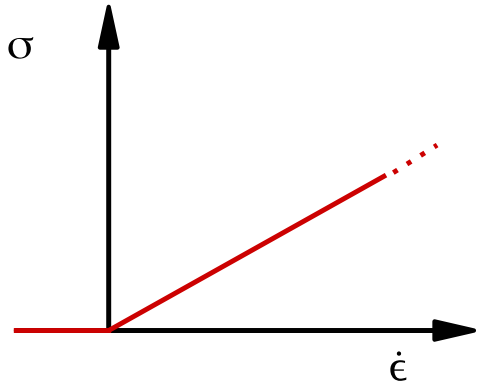

Figure 1.5: In a Newtonian fluid there is linearity between the stress and the time derivative of the strain.

A Newtonian fluid is a material able to flow, in other words it deforms indefinitely after the application of a finite stress (Figure 1.5). The constitutive equation is:

$$\sigma_{ij} = \eta \dot{\epsilon}_{ij}, \tag{1.5}$$

where σ_{ij} is the stress tensor, η is the viscosity and $\dot{\epsilon}_{ij}$ is the strain rate. Almost all fluids we encounter in every-day life are newtonian fluids. Viscosity is a parameter that depends on the material properties, and it is measured in units of $Pa \cdot s$. Differently from elastic materials, newtonian fluids are not able to recover the original state. In rheology, newtonian fluids are conventionally represented with a damper or a dashpot.

If we consider the response of a Newtonian fluid under the effects of a creep test, from the 1D constitutive equation $\sigma = \eta \dot{\epsilon}$ we obtain

$$\sigma_0 H(t) = \eta \dot{\epsilon} \quad \Rightarrow \quad \epsilon = \int \frac{\sigma_0 H(t)}{\eta} dt = \frac{\sigma_0}{\eta} t \quad for\ t \geqslant 0\ . \tag{1.6}$$

In Figure 1.6 this result is schematically displayed. We also note that, since in a stress-relaxation test we have $\epsilon(t) = \epsilon_0 H(t)$, the stress is

$$\sigma = \eta \epsilon_0 \delta(t) \quad \text{since} \quad \frac{dH(t)}{dt} = \delta(t) \quad for\ t \geqslant 0. \tag{1.7}$$

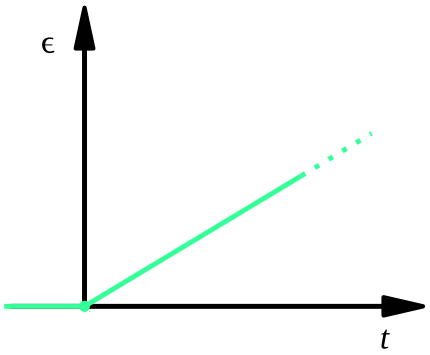

Figure 1.6: Result of a creep test on a Newtonian fluid.

Viscoelasticity

Combining together elastic and viscous behaviour we obtain viscoelastic materials. They combine the properties of an elastic body with those of a fluid.

Maxwell Body

One obtains a Maxwell fluid when a spring and a damper are coupled in series. The effect of this disposition is that the two elements are subject to the same stress, but not to the same strain. By linearity, the total strain rate $\dot{\epsilon}$ can be obtained by adding together the elastic and the fluid contributions [9]:

$$\dot{\epsilon} = \dot{\epsilon}_H + \dot{\epsilon}_N = \frac{\dot{\sigma}}{\mu} + \frac{\sigma}{\eta} \ . \tag{1.8}$$

In order to compute the response of this body to the creep test and to the relaxation test, we will make use of Laplace transform:

$$\mathcal{L}\{f(t)\} = \tilde{f}(s) = \int_{0^-}^{\infty} f(t)e^{-st}dt \tag{1.9}$$

We remark that the definition (1.9) is not the most general definition for the Laplace transform, but the more suitable for our purposes. For a further reading about Laplace

transform and their properties, see [10, 11]. By applying the Laplace transform to Eq. (1.8), we obtain

$$\tilde{\epsilon}s - \epsilon(0^-) = \frac{\tilde{\sigma}s - \sigma(0^-)}{\mu} + \frac{\tilde{\sigma}}{\eta} \ , \tag{1.10}$$

and, assuming that both pre-initial conditions vanish, we have:

$$\tilde{\epsilon}s = \frac{\tilde{\sigma}s}{\mu} + \frac{\tilde{\sigma}}{\eta} \ , \tag{1.11}$$

so that, after some elementary steps, one obtains:

$$\tilde{\sigma} = \frac{\mu s}{s + \tau_M^{-1}}\tilde{\epsilon} = \tilde{\mu}_M \tilde{\epsilon} \quad \text{with } \tau_M = \frac{\eta}{\mu}. \tag{1.12}$$

The τ_M constant is called *Maxwell relaxation time* and $\tilde{\mu}_M$ is the Maxwell *complex modulus*. Curiously, Eq. (1.12) is formally identical to Hooke's law (Eq. 1.2). This is an expression of the *Correspondence Principle* of linear viscoelasticity: the Laplace transformed viscoelastic rheological equation is formally obtained from the elastic equations, provided that the elastic moduli (e.g., μ) are changed into appropriate complex moduli, like $\tilde{\mu}_M(s)$, which is a function of the Laplace variable s. The Correspondence Principle will be introduced formally in Section 1.3. Considering Eq. (1.12) we can compute the response to a creep test and to a relaxation test in the same way we do for the elastic and newtonian fluid bodies.

For the creep test, by substituting $\tilde{\sigma}$ with the Laplace transform of $\sigma(t) = \sigma_0 H(t)$ we obtain:

$$\frac{\tilde{\sigma_0}}{s} = \tilde{\mu}_M \tilde{\epsilon} \ \Rightarrow \ \frac{\tilde{\epsilon}}{\sigma_0} = \frac{1}{s\tilde{\mu}_M} \equiv \tilde{J}_M \ , \tag{1.13}$$

where $\tilde{J}_M$ is the Maxwell *creep compliance*. To obtain the body response to the Heaviside load, one should perform, on the expression found, the inverse Laplace transform, in order to retrieve the solution into the time domain. The result is:

$$\mathcal{L}^{-1}\{\tilde{J}_M\} = \mathcal{L}^{-1}\left\{\frac{1}{\mu s} + \frac{1}{\eta s^2}\right\} = J_M = \frac{1}{\mu}H(t) + \frac{t}{\eta}, \tag{1.14}$$

hence:

$$\epsilon(t) = \frac{\sigma_0}{\mu} H(t) + \frac{\sigma_0}{\eta} t. \tag{1.15}$$

In Figure 1.7 it is possible to visualize this result.

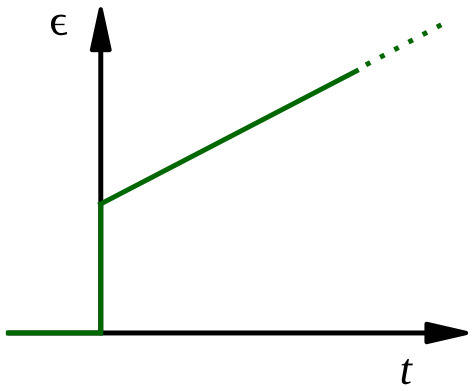

Figure 1.7: The response of a Maxwell body to a stress relaxation test. We can see the instantaneous elastic response, immediately followed by a steady-state regime.

As regard the relaxation test, starting from 1.12 and considering the Laplace transform of $\epsilon(t) = \epsilon_0 H(t)$, we have:

$$\tilde{\sigma} = \frac{\tilde{\mu}_M}{s} \epsilon_0 \;\Rightarrow\; \frac{\tilde{\sigma}}{\epsilon_0} = \frac{\tilde{\mu}_M}{s} \equiv \tilde{G}_M \tag{1.16}$$

where G_M is called *relaxation modulus*. Ratio $\tilde{\sigma}/\epsilon_0$ represents the (transformed) stress per unit strain in a relaxation experiment. It only depends upon the nature of the rheological body. Once again, performing the inverse Laplace transform, we obtain:

$$\mathcal{L}^{-1}\{\tilde{G}_M\} = \mathcal{L}^{-1}\left\{\frac{\mu}{s + \tau_M^{-1}}\right\} = G_M(t) = \mu e^{-t/\tau_M}. \tag{1.17}$$

Hence, we obtain the response of the Maxwell body under the action of a constant strain in terms of the stress:

$$\sigma(t) = \epsilon_0 \mu e^{-t/\tau_M}, \tag{1.18}$$

showing that the stress decreases exponentially, with a decay constant τ_M. The phenomenon is known as *stress relaxation.*, The function (1.18) reported in Figure 1.8.

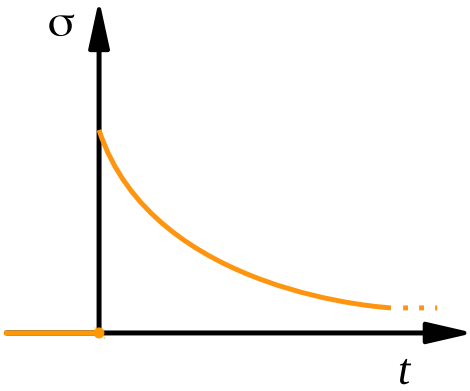

Figure 1.8: The response of a Maxwell's body to an applied constant deformation, in terms of stress.

The Kelvin-Voigt body

This rheological body is composed of the same rheological elements of the Maxwell body, but in this case they are arranged in parallel. This fact deeply modifies the behaviour of the system. This time indeed, the dash and the spring are subject to the same strain, but not to the same stress.

The stress will be the sum of two contributions:

$$\sigma = \sigma_H + \sigma_N = \mu\epsilon + \eta\dot{\epsilon} \ , \tag{1.19}$$

where η is the viscosity, and μ the rigidity. Even this time we will compute the transformed constitutive equation and we will obtain the creep compliance J_K and the relaxation modulus G_K.

By applying the Laplace transform to (1.19) one obtains:

$$\tilde{\sigma} = \eta(s\tilde{\epsilon} - \epsilon(0^-)) + \mu\tilde{\epsilon}, \tag{1.20}$$

and assuming $\epsilon(0^-) = 0$, we find:

$$\tilde{\sigma} = \tilde{\mu}_K \tilde{\epsilon}, \quad \text{with} \quad \tilde{\mu}_K = \eta \left(s + \frac{\mu}{\eta} \right) \tag{1.21}$$

where the term $\tilde{\mu}_K$ is the complex modulus for the Kelvin-Voigt model. By defining the *characteristic time* $\tau_K = \eta/\mu$, the complex modulus becomes:

$$\tilde{\mu}_K = \eta \left(s + \frac{1}{\tau_K} \right) \ . \tag{1.22}$$

Even in this case we remark that Eq. (1.21) is formally identical to Hooke's law (1.2). To determine the creep compliance J_K, in Eq. (1.21) we substitute the Laplace transform of $\sigma(t) = \sigma_0 H(t)$, that is $\tilde{\sigma} = \sigma_0/s$. It follows that:

$$\frac{\tilde{\epsilon}}{\sigma_0} = \frac{1}{s\tilde{\mu}_K} = \frac{1}{s\eta(s + \frac{1}{\tau_K})} = \tilde{J}_K \ , \tag{1.23}$$

which is the Kelvin-Voigt creep compliance. Since $\tilde{J}_K$ is the product of two transforms, to compute the inversion to the time domain it is necessary to apply the *Convolution Theorem*: $\mathcal{L}\left(f(t) * g(t)\right) = \tilde{f}(s)\tilde{g}(s)$. After some lines of straightforward calculations, one obtains:

$$J_K(t) = \frac{1}{\mu} \left(1 - e^{-t/\tau_K} \right) \ . \tag{1.24}$$

The form of this last equation describes the response of a Kelvin-Voigt body under the action of a constant stress. It is worth to note that here there is no instantaneous response, since $J_K(0) = 0$, and the subsequent flow is characterized by a transient behaviour, where the strain rate varies with time [9]. A constant strain is however reached for time $t \longrightarrow \infty$. In Figure 1.9 one can see qualitatively this kind of response. Regarding the relaxation modulus G_K, by substituting the Laplace transform of the constant strain $\epsilon(t) = \epsilon_0 H(t)$, that is $\tilde{\epsilon} = \epsilon_0/s$ and Eq. (1.21), we obtain

$$\frac{\tilde{\sigma}}{\epsilon_0} = \frac{\tilde{\mu}_K}{s} = \tilde{G}_K \ , \tag{1.25}$$

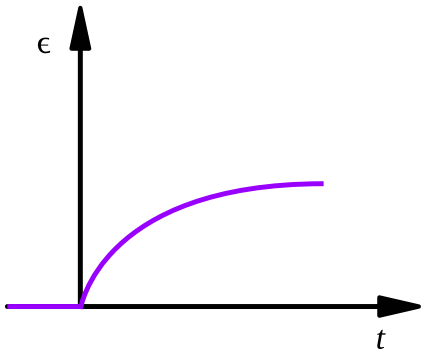

Figure 1.9: The response of a Kelvin-Voigt's body to an applied constant stress, in terms of the strain.

which is what we were looking for. The inversion to the time domain is immediate:

$$G_K(t) = \eta\delta(t) + \mu H(t), \quad t \geq 0 \ . \tag{1.26}$$

In this case, if the Kelvin-Voigt body is subject to a constant strain, it responds with a initial instantaneous elastic deformation, followed by a regime that remains on a constant value of stress: hence the Kelvin-Voigt body does not relax (Figure 1.10).

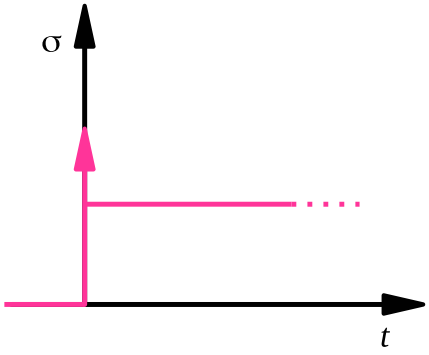

Figure 1.10: The response of a Kelvin-Voigt's body to an applied constant deformation, in terms of the stress.

The Burgers body

The Burgers body is a rheological model composed by a Maxwell body and a Kelvin-Voigt body arranged in series. Under a creep test, it exhibits an instantaneous elastic

behaviour, followed by a transient creep and damping of vibrations over the short time-scale, and a linearly viscous behaviour over the long time-scale. For this properties it was proposed as an unifying model for the rheology of the mantle, capable of accounting for vast range of phenomena [3] (from the propagation of seismic waves to PGR). It can be demonstrated that the creep compliance J_B for the Burgers body is the sum of J_M and J_K:

$$J_B(t) = \frac{1}{E_2}H(t) + \frac{1}{E_1}\left(1 - e^{-\frac{t}{\tau_K}}\right) + \frac{t}{\eta_2} \ , \tag{1.27}$$

where subscripts $_{1,2}$ refer to the Kelvin-voigt and the Maxwell component respectively. The creep compliance J_B reflects the ability of a Burgers body to respond to a finite stress with an instantaneous elastic response, then a transient, and finally a steady-state creep.

The relaxation modulus require more computational work. The final expression is:

$$G_B(t) = G_1 e^{-\frac{t}{\tau_1}} + G_2 e^{-\frac{t}{\tau_2}} \ , \tag{1.28}$$

where G_1, G_2, τ_1, τ_2 are positive constants determined by the material parameters E_1, E_2, η_1, η_2. Thus, the relaxation of a Burgers body occurs following a discrete spectrum of relaxation. In the following Figures 1.11 and 1.12, the creep compliance and the relaxation modulus are qualitatively displayed.

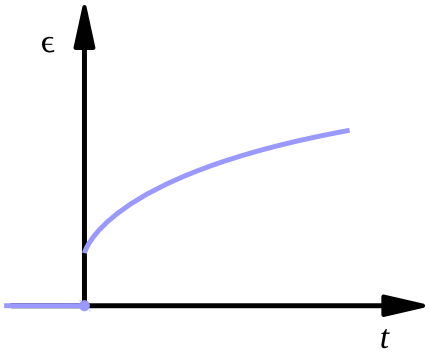

Figure 1.11: The response of a Burgers body to an applied constant stress, in terms of strain.

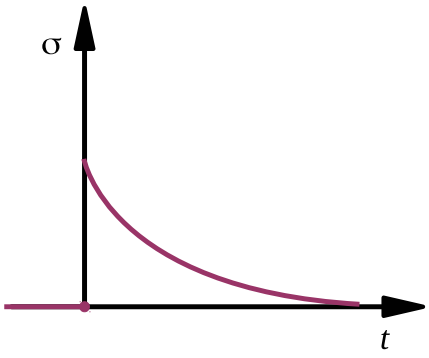

Figure 1.12: The response of a Burger body to an applied constant strain, in terms of stress.

Transient effects

Considering Eq. (1.15), valid for a Maxwell body, we can note that the transition from the elastic response to the steady state creep is virtually instantaneous, while the typical outcome of a cyclic test performed on a general polycrystalline material exhibits a smoother transition. As we can see in Figure 1.13, the more general form of response to a stress-recovery test can be split into five steps:

- When the load is applied at time $t = t_1$, there is an instantaneous elastic deformation.
- This is followed by a transient creep, where the strain increases with time at a decreasing rate.
- When conditions permit (i.e., the temperature is sufficiently high), the transient creep state may be followed by a stage of steady-state creep, characterized by a constant strain rate [3].
- Once the load is removed ($t = t_2$) there is an instantaneous recovery of the elastic strain, followed by a time-dependent recovery of the transient strain.
- At the end, the deformation acquired during the steady-state creep is permanent and unrecoverable.

This kind of history plot is typical of polycrystalline materials, but the time-dependence of the transient creep function is extremely variable, depending on material and external

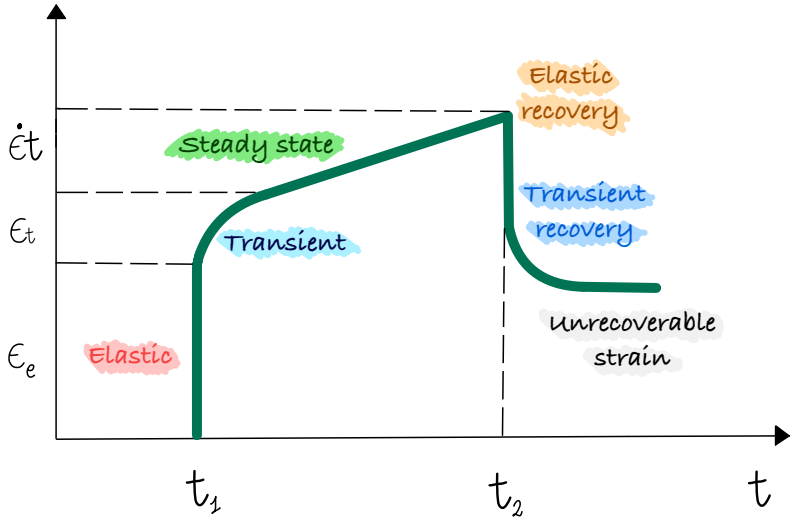

Figure 1.13: General response of polycrystalline materials in terms of deformation to a stress-recovery test.

conditions. This is why several empirical laws have been proposed, which account, in some cases, for experimental observations. Some of these are:

Exponential retardation	$\epsilon(t) = A\left[1 - e^{-\frac{t}{\tau}}\right]$
Logarithmic creep law	$\epsilon(t) = A\log(1+\alpha t)$
Modified Lomnitz law	$\epsilon(t) = \frac{\sigma}{\mu}\left(1 + \frac{q}{\alpha}[(1+\alpha)^{\alpha} - 1]\right)$,

where A, q and α are parameters that depend on the material. In this thesis I will consider a particular transient creep function, determined by Andrade in 1910 [12], that will be discussed in the next sections.

1.3 Correspondence Principle

Considering the constitutive equation of a linear viscoelastic body [13]:

$$p_0\sigma + p_1\dot{\sigma} + p_2\ddot{\sigma} + ... = q_0\epsilon + q_1\dot{\epsilon} + q_2\ddot{\epsilon} + ... \tag{1.29}$$

or, more briefly

$$\mathbf{P}\sigma(\mathbf{x},t) = \mathbf{Q}\epsilon(\mathbf{x},t) \tag{1.30}$$

where $\mathbf{P}$ and $\mathbf{Q}$ are operators of the form $F = \sum_{j=0}^{n} f_j \frac{d^j}{dt^j}$.

Taking their Laplace transforms, one obtains:

$$P(s)\tilde{\sigma}(\mathbf{x},s) = Q(s)\tilde{\epsilon}(\mathbf{x},s) \tag{1.31}$$

where P and Q now are polynomials of the variable s. Then, writing

$$\tilde{\sigma}(\mathbf{x},s) = \frac{Q(s)}{P(s)}\tilde{\epsilon}(\mathbf{x},s) = \tilde{E}(s)\tilde{\epsilon}(\mathbf{x},s) \tag{1.32}$$

we obtain an expression that is formally identical to the Hooke linear elastic law:

$$\sigma(\mathbf{x},t) = E(t)\epsilon(\mathbf{x},t)\ . \tag{1.33}$$

We have just shown that if we know the analytical solutions of the elasto-static problem (with its appropriate boundary conditions), then the solution in the Laplace domain of the quasi-static viscoelastic problem is obtained by substituting in the corresponding elastic solution the constant $E(t)$ with the appropriate $\tilde{E}(s)$. Then, in principle, the solution of the corresponding elastic problem can be anti-transformed in order to obtain the viscoelastic solution in the time domain. This principle has been used in Section 1.2 to compute the creep compliance and the relaxation modulus of Maxwell and Kelvin-Voigts bodies.

1.4 Earth rheological Structure

The Earth's rheological stratification can be inferred by laboratory experiments made upon typical mantle rocks, by studying the long period behaviour of the Earth in response to surface loading and unloading and also by seismological investigations. The seismic wave propagation demonstrate that on short time scale $(10^0 \div 10^5 s)$, the Earth interior behaves like a solid, while by studying GIA it seems that the Earth behaves like a fluid. This fact could appear ambiguous, but only considering classical definition of solid and

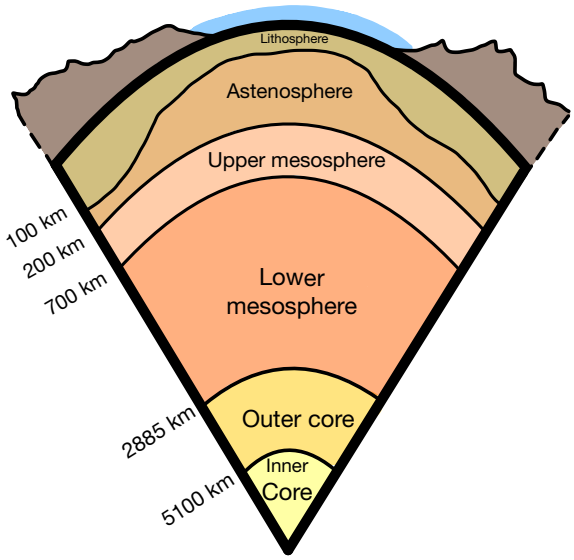

Figure 1.14: Earth's rheological structure. *Adapted from [7].*

fluid, based on the atomic structure of the materials. In rheology this fact is well known, and to describe it, Markus Reiner, one of the fathers of rheology, introduced the so-called *Deborah Number* [14]:

$$De = \frac{\tau_{rel}}{\tau_{exp}} = \frac{Relaxation\ time}{Time\ scale\ of\ the\ experiment} \ . \tag{1.34}$$

A small De is an indicator of fluid behaviour, while larger De is indicator of an elastic behaviour. The same material can thus exhibit a different behaviour under different external conditions: for instance, in the mantle, in the case of seismic waves propagation, we have $De \approx \infty$, for GIA we have $De \approx 1$, and for mantle convection $De \approx 0$. Once clarified this aspect and the importance of considering time-scales in rheology, we can try to divide the Earth on a rheological basis. We have:

- **Lithosphere.** This first layer is elastic, even on long time scale (10^8 *years*). Its lower boundary is the 1600 K isotherm: over this temperature, the rocks lose their rigidity, and start behaving plastically. The lithosphere, or *strong layer*, is fragmented in plates that move rigidly under the effect of stresses generated by mantle convection. Under the oceans, the mean lithospere thickness is 100 km, while under continents it can reach 200 km. Considering the compositional

stratification, the lithosphere includes the crust and the upper part of the mantle, usually named lithospheric mantle. The behaviour of rocks depends not only on temperature, but also on the level of applied stress. This explains why in some regions of the lithosphere, we can observe an elastic-plastic behaviour even at the depth of the lower crust or of the lithospheric mantle. Under the 1600 K isotherm we find the sub-lithospheric mantle, a zone that exhibits solid state creep, a particular behaviour that allows solid rock to flow like a fluid, under specific conditions of temperature and pressure. The layers of the Earth that exhibit solid state creep, after the application of a constant stress, are subject to a stationary flux if we consider a time scale of 10^4 yrs [7].

- **Astenosphere.** Beneath the lithosphere, we find the asthenosphere. This layer is able to sustain deviatoric stress only on very short (100 $years$) time scales, and flows on longer time scales. The thickness of the astenosphere is comparable to that of the lithosphere [7].

- **Mesosphere.** This is the part of the mantle in which convection takes place. We can distinguish an upper part, ranging from the boundary with the asthenosphere to 700 km, with a mean viscosity of 10^{21} $Pa \cdot s$, and a lower part, that arrives to the Gutenberg discontinuity, with a mean viscosity of $10^{22 \div 23} Pa \cdot s$ [7].

- **Outer core**. The absence of S-waves suggests that the outer core is fluid. This statement finds support in the existence of the Earth magnetic field: only the presence of a fluid conductor could explain it. Indeed, Fe is able to maintain its magnetic properties only under temperature below Curie point ($780°C$), but the core estimated temperature vary from $3000°C$ in the mantle-outer core boundary to $6000°C$ in the outer-inner core boundary [6].

- **Inner core.** The return of the S-waves suggest the presence of a solid, elastic inner core.

1.5 The problem of Mantle rheology

The detailed understanding of Earth's mantle behaviour is still an open topic in geophysics. Even if we dispose of a good quantity and variety of data, the complexity of

the phenomena that take place in it and the impossibility of direct observations represent important obstacles. In the late 70s, satellite data and further analysis of GIA seemed to confirm the results of previous studies of Haskell [15] in which mantle viscosity was assumed to have the almost constant value of $10^{21} Pa \cdot s$. This clashed with the conception of the Earth thermal structure: considering the Hering-Nabarro creep as the dominant mechanism for deformation in the mantle, one finds that viscosity should increase with depth [16].

An explanation for this fact is considering that the ratio of the actual temperature over the melting temperature is constant throughout the mantle, or even (and more correctly) a decreasing function of depth. Another explanation could be considering that mantle creep obeys to a power law with stresses increasing with depth, but in this case there would be a contradiction, since glacial rebound stresses decrease with depth. One possible way out of this dilemma is to bring transient creep phenomena into the analysis [16]. The first considering the idea of a transient in mantle was J. Weertman, on the base of qualitative considerations, and later Peltier, in 1985, provided a mathematical support for this hypothesis [17].

If the transient is present, and if we assume that the mantle has a linear rheological response, then a suitable model for describing it would be the Burger's bi-viscous body [3] (see Section 1.2). For this reason, the Burger's body was used by Peltier in its seminal work in 1981 [18], and became a reference model in Geophysics for the study of PGR when transient effects are taken into account (along with the Maxwell body when transient phenomena are neglected). However, the Burger's body represents only a first approximation, that assumes implicitly a discrete spectrum of relaxation. On the other side, creep laws like Andrade's one offer a more realistic description of the transient stage, in which the spectrum of relaxation is continuous, with the downside of a more complex mathematical description. In this work I will consider which role plays the presence of a transient in the Earth's mantle, representing it through Andrade's creep law, and I will try to answer to this fundamental question: if the transient would be present actually, considering that, since last glacial maximum, 21 000 years have passed, are we still able to see it?

Two-layer mantle: Lambeck's school of thought

A fundamental ingredient in the PGR problem is a realistic ice-history, that is the spatio-temporal evolution of the ice-sheet. Depending on the problem we need to solve, the ice-history must be more or less detailed, regional or global, *etc...* . To understand present-day deformation due to PGR and to obtain valuable information about Earth's rheology, it is necessary to characterize, as better as possible, the deglaciation phase of the last glacial cycle, which started 21 *kyr* ago. The major attempts to do so come from two groups: Peltier and colleagues, and Lambeck and colleagues. The main differences in the two approaches is in the treatment of ice loads over continental shelves or shallow basins and in the way in which their techniques are applied to the observational datasets [19]. Peltier's analysis mainly focuses on global solutions, while Lambeck's one focuses on separate regional solutions.

We will not explain in detail the two approaches, because for our purpose it is sufficient to consider the ultimate results of their analyses. While models by Peltier school assume a viscosity in the upper mantle at $10^{21}\ Pa{\cdot}s$ and the lower one at $2{\cdot}10^{21}\ Pa{\cdot}s$ [20], Lambeck's school prefers considering a two-layer mantle model with viscosities for the upper and the lower mantle set to $5.1{\cdot}10^{20}\ Pa{\cdot}s$ (with a possible range $(3.5{-}7.5)10^{20}\ Pa{\cdot}s$), and $1.3 \cdot 10^{22}\ Pa \cdot s$ (with a possible range $(0.8 - 2.8)10^{22}\ Pa \cdot s$) [19]. Of course these two models produce different expected displacements and sea-level change histories, and it will be interesting to see if the presence of the transient is more evident in one of the two models. For this reason we will take both two models in consideration.

1.6 Andrade Rheology

One of the first quantitative descriptions of plastic deformation of metal and polycrystalline materials at high temperature is the one proposed by Andrade in 1910 [12], who reported the results of his experimental studies of deformation of Pb and Cu [21]. In general, creep of solids can be subdivided into several stages: at first it is possible to observe an instantaneous creep, that occurs immediately after the application of the load; then a *transient* creep follows. If the temperature is high enough, transient creep usually leads to linear steady state creep, followed by an accelerated creep preceding the rupture [3]. In Figure 1.15 it is possible to see one of the plots reported in Andrade's

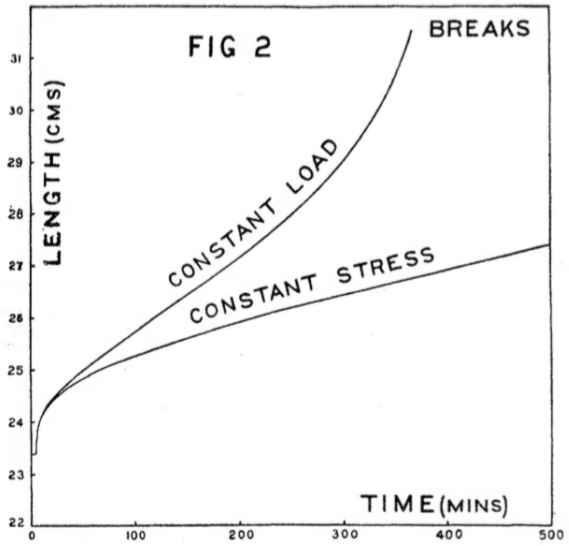

Figure 1.15: The curve "Constant Stress", shows each one of the three step described above, the instantaneous creep, the transient and the steady-state, while the curve "constant load" shows the behaviour of the body charged with a constant load, until the break point. From [12].

seminal work [12].

During experiments, Andrade observed that the metallic sample obeyed the following law:

$$\epsilon = \epsilon_0 + \beta t^{\alpha} \tag{1.35}$$

where ϵ_0 is the initial deformation, β a material parameter and $\alpha = 1/3$ according to Andrade's experiments. Parameter α determines the duration of the transient response in the primary creep. Lee and Morris [22] established that α is a function of the presence of impurities at the grain boundaries as well as irregularities in the grain shape. Parameter β characterizes the intensity of anelastic friction in the material, and therefore must depend upon the density of the defects in the lattice of the material. However, the shape of this dependence remains unknown, because no research has ever been undertaken in this direction in the case of diffusion-driven attenuation [23]. Analysing its physical dimensions, it results that β has units $s^{-\alpha}Pa^{-1}$. Reporting the same reasoning of Castillo-Rogez et al. [23], it would not be incorrect presuming that these units are the

result of a combinations of parameters "with less exotic dimensions". From their work it results experimentally that $\beta = \mu^{-(1-\alpha)}\eta^{-\alpha}$, where μ is the elastic rigidity and η is the viscosity of the material.

In order to obtain the complex modulus suitable for Andrade, let's consider the Andrade's rheology creep function:

$$J_A(t) = \frac{1}{\mu}H(t) + \beta t^{\alpha} + \frac{1}{\eta}t \ . \tag{1.36}$$

By considering equation (1.13), let's try to compute the complex modulus of Andrade's model by multiplying the Laplace transform of (1.36) by s:

$$s\tilde{J}_A(s) = \frac{1}{\mu s}s + \beta\Gamma(\alpha+1)s^{-(\alpha+1)}s + \frac{1}{\eta s^2}s \tag{1.37}$$

where $\Gamma(x)$ is the Gamma Function. Exploiting the definition of β we have:

$$s\tilde{J}_A(s) = \frac{1}{\mu} + \frac{\Gamma(\alpha+1)}{\mu^{(1-\alpha)}s^{\alpha}\eta^{\alpha}} + \frac{1}{\eta s} \tag{1.38}$$

and finally, indicating with $\tau_M = \eta/\mu$ one obtains:

$$s\tilde{J}_A(s) = \frac{1}{\mu} + \frac{\Gamma(\alpha+1)}{\mu(s\tau_M)^{\alpha}} + \frac{1}{\tau_M \mu s} = \frac{1}{\mu}\left[1 + \frac{\Gamma(\alpha+1)}{(s\tau_M)^{\alpha}} + \frac{1}{\tau_M s}\right] \ , \tag{1.39}$$

So we find:

$$\tilde{\mu}_A = \frac{1}{s\tilde{J_A}(s)} = \left\{\frac{1}{\mu}\left[1 + \frac{\Gamma(\alpha+1)}{(s\tau_M)^{\alpha}} + \frac{1}{\tau_M s}\right]\right\}^{-1} \ . \tag{1.40}$$

It is interesting to remark that once the Laplace transform of (1.36) is given, through the general relationship:

$$\tilde{J}\tilde{G} = \frac{1}{s^2}, \tag{1.41}$$

valid for all linear rheologies, it is possible to obtain the Andrade's relaxation modulus $G_A(s)$, completely characterizing the rheological response of this kind of body [24]. Unfortunately, a closed-form inversion of $G_A(s)$ to obtain $G_A(t)$ is not possible, and one

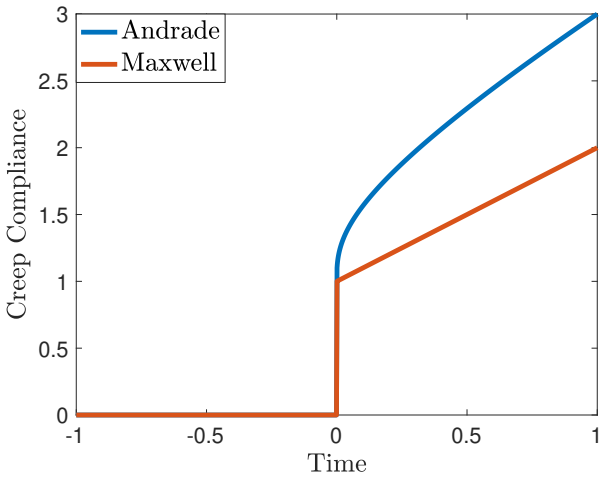

Figure 1.16: Creep compliance of Andrade's body (blue) and Maxwell's one (red) plotted as a function of time. As we can see, the transition between the elastic response and the steady-state in Maxwell's case is sharp, while in Andrade's body the transient phase is smoother and offers a gradual transition from the instantaneous elastic response to the steady-state, in agreement with laboratory observations.

must appeal to numerical methods.

Transient creep of many materials at high temperatures obey Andrade's law [5], and during years it has gained much popularity in planetary sciences, while in geophysics the Burger's solid or the standard linear solid are preferred, but this is just a choice of convenience that guarantees a completely analytical resolution of the problem.

In this Thesis I will focus the attention upon the differences that emerges in the estimates of expected displacement between models that consider a non-transient behaviour for the mantle (like the Maxwell body) and models in which the transient is present, like Andrade's one. For a visualisation of the main differences between this two models, in Figure 1.16 I show their creep compliance to facilitate the comparison.

Insights into Andrade's rheology

Let's focus one moment on Figure 1.16. The main feature of Maxwell rheology is being the simplest composition of an instantaneous elastic response and a subsequent newtonian flow: hence, immediately after the elastic phase, the creep compliance follows a linear regime with a constant slope. On the contrary, as it is clear even from Figure 1.16,

in the definition of the Andrade rheology, the exponential factor t^α does not allow any relaxation: even if the variation of the slope is more and more weak as the time passes, actually we can't say, in a strict mathematical way, that Andrade's rheology reaches a steady stare regime. Of course we are nitpicking, but aware of this fact we can try to do further comparison between Andrade and Maxwell rheological models. Observing Andrade's creep function (1.36) and Maxwell's one (1.14), we notice that they differ only for the additional factor βt^α. We can thus try to establish under which conditions the time derivative of Andrade's term βt^α is comparable to the one of Maxwell's term. By writing Eq. (1.36) and (1.14) derivatives for time $t > 0$:

$$\begin{aligned} J_A(t) &= \frac{1}{\mu}\left[H(t) + \left(\frac{t}{\tau_M}\right)^\alpha + \frac{t}{\tau_M}\right] \;\rightarrow\; J'_A(t) = \frac{1}{\mu}\left[\frac{\alpha}{\tau_M}\left(\frac{t}{\tau_M}\right)^{\alpha-1} + \frac{1}{\tau_M}\right] \\ J_M(t) &= \frac{1}{\mu}\left[H(t) + \frac{t}{\tau_M}\right] \rightarrow\; J'_M(t) = \frac{1}{\mu}\left[\frac{1}{\tau_M}\right] \end{aligned} \tag{1.42}$$

where we have exploited the definition of β, we understand that we are interested in determining for which conditions

$$\frac{\alpha}{\tau_M}\left(\frac{t}{\tau_M}\right)^{\alpha-1} = \frac{1 \pm \epsilon_0}{\tau_M} \tag{1.43}$$

where ϵ_0 is arbitrarily small. After some algebra, we find:

$$\frac{t}{\tau_M} = \left(\frac{\alpha}{1 \pm \epsilon_0}\right)^{\frac{1}{1-\alpha}} \tag{1.44}$$

and by choosing $\epsilon_0 = -0.1$, $\alpha = 1/3$, we obtain that the ratio $t/\tau_M \simeq 0.2$. These fast calculations demonstrate that the two terms are comparable after a time that corresponds to 1/5 of Maxwell's relaxation time.

Chapter 2

Love Numbers

Love numbers (LNs) are a powerful tool in (Geo)physics, whose importance and main features will be exposed in this chapter. First developed in the context of the tidal theory, the LNs have been lately applied to the surface load problem, becoming the Load Love Numbers (LLNs). After a brief description of their initial conception (Section 2.1), I will present their elastic and viscoelastic form (Sections 2.2, 2.3). Considering that their basic definition refers to the response to an impulsive load, in Section 2.4 I will show how to obtain Heaviside LLNs, which account for the response to a step function forcing. In Section 2.5 I will show their analytical form and in Section 2.6 I will report the LLNs for the case of a Kelvin sphere behaving according to Andrade's rheological model.

2.1 The origin of Love numbers

Love numbers (LN) were first introduced by the english mathematician A. E. H. Love in 1909 [25]. Love introduced its formalism in the study of the Earth's tides, allowing a simple and elegant description of a extremely complex phenomenon. In a few words we can define LNs as dimensionless parameters that measure the rigidity of a planetary body and the susceptibility of its shape to change in response to a tidal potential [26]. Love originally introduced the vertical LN h and the potential LN k; later, in 1912, T. Shida added a third LN, the horizontal one, l.

Love's idea was as brilliant as simple: he understood that the total gravitational potential, evaluated at a given point at the surface of a body subject to a tidal force,

must be the sum of two contributions: a direct potential, and an indirect one, due to the Earth's response:

$$\phi^{tot} = \phi_0 + \phi'. \tag{2.1}$$

In his seminal work Love considered an ideal homogeneous spherical Earth of radius a and density ρ. Denoting by ρ_0 and p_0 the mean density of the Earth and the pressure, trough the hydrostatic equilibrium, we can define the gravitational potential ϕ_0 as:

$$\frac{\partial \phi_0}{\partial r} = \frac{1}{\rho_0}\frac{\partial p_0}{\partial r} \ , \tag{2.2}$$

where as a first approximation, we have assumed that p_0 is function of the distance r from the centre of the Earth only, and that $p_0(a) = 0$.

In general, the gravitational potential ϕ can be expanded in series of harmonics:

$$\phi_0(r, \theta, \lambda, t) = \sum_{n=0}^{\infty} \phi_{0n}(r, \theta, \lambda, t) \ . \tag{2.3}$$

Then, let's consider the effect of an external body, deforming with its gravitational attraction the undisturbed Earth described above. We are interested in computing the total deformation that the Earth will experience under the effect of the tidal forces, so we suppose that these forces can be derived from another potential which, in the region $r > 0$, can be expressed as a sum of spherical solid harmonics of integer degrees as well.

Let ϕ'_n be a single spherical harmonic term of this sum, the degree n of this term being a positive integer. Under the action of the forces derived from the potential ϕ' the body will be deformed. The total gravitational potential ϕ^{tot} of the disturbed body at a point will not be ϕ_0, but it will be the sum of ϕ_0, and the potential ϕ' due to the mass redistribution. The great idea that Love had at the time was supposing that, since tide deformations can be regarded as infinitesimal, each one of the harmonic component of the incremental potential ϕ' should be proportional to the corresponding harmonic component of ϕ_0, allowing us to write:

$$\phi'_n = K_n(r)\phi_{0n} \ . \tag{2.4}$$

So finally we find:

$$\phi^{tot} = \sum_{n}^{\infty}[\phi_{0n} + K_n(r)\phi_{0n}] = \sum_{n}^{\infty}[1 + K_n(r)]\phi_{0n} = \sum_{n}^{\infty}(\phi_{0_n} + \phi'_n) = \phi_0 + \phi' \quad (2.5)$$

where $K(r)$ is a function of r. Then, defining $K(a) = k$ the value that this function assume at the Earth surface, we have the so called Love number for the gravitational potential.

Following the same reasoning, it is possible to define a Love number h for the the vertical component of the displacement field, and the Shida's LN l for the horizontal components of the displacement field.

2.2 Elastic Load Love Numbers

In the following pages it will be useful to refer to another derivation of LN, that will be described in this paragraph. In the previous Section we introduced tidal Love numbers (TLNs), but for the purpose of this thesis we will make large use of loading Love numbers (LLNs). Indeed, with appropriate modifications, the formalism of LNs is suitable also for the description of the response of the Earth due to space-temporal variations of a applied load, that is the Surface Load Problem.

So we consider a point mass acting on the surface of a rigid, spherically symmetric Earth. Because of rigidity, the surface stress exerted by the mass due to its own weight does not cause deformation. However, the load, with its perturbing mass, induces a "direct variation" of Earth's gravitational potential. We can describe the point mass acting on the sphere as:

$$\mu(t) = \delta(t)\delta m \ , \quad (2.6)$$

where $\delta(t)$ is Dirac's delta, t is time, and δm is the load mass, which we assume to be negligible with respect to the whole Earth's mass.

Our goal now is to compute the variation in the gravitational potential that an observer in $O = (\theta, \lambda)$, where θ and λ are the co-latitude and the geocentric longitude, will record after the application of the point mass. As reference figure, consider Figure 2.1. According to Newton's law, if α is the angular distance from the point mass and

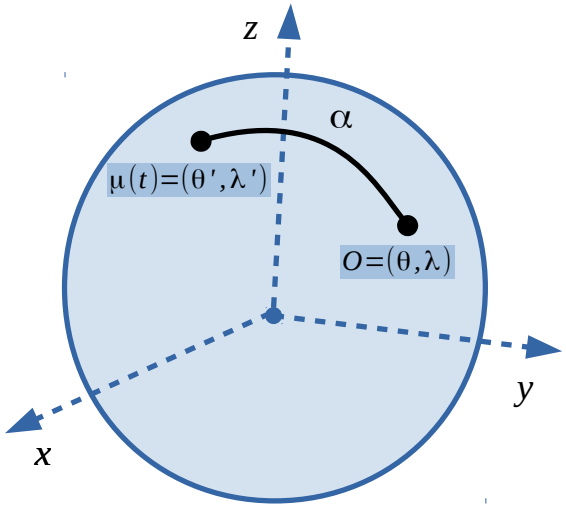

Figure 2.1: Schematic representation of the current problem: the point mass $\mu(\theta', \lambda')$ acts on a rigid Earth. We aim to compute its effects on the gravitational potential in the point O.

the observer, then the direct gravitational potential ϕ^r reads

$$\phi^r(\alpha, t) = \frac{G\mu(t)}{d(\alpha)} \ , \tag{2.7}$$

where r stands for *rigid*. By elementary plane trigonometry, $d(\alpha) = 2a\sin(\frac{\alpha}{2})$, and calling m^e the Earth's mass, using Universal Gravitation Law $g = Gm^e/a^2$, we have:

$$\phi^r(\alpha, t) = \delta(t)\frac{ag\delta m}{2m^e \sin(\frac{\alpha}{2})} \ . \tag{2.8}$$

Now we can define the Green's function (GF) for the direct gravitational potential as

$$\Gamma^{\phi,r}(\alpha, t) = \frac{\phi^r(\alpha, t)}{\delta m} = \delta(t)\frac{ag}{2m^e \sin(\frac{\alpha}{2})} \ . \tag{2.9}$$

which represents the potential variation per unit applied mass δm and per unit time.

A more modern formulation can be achieved by recognizing in the trigonometrical

term an analytical result involving Legendre polynomials [9]:

$$\frac{1}{2\sin(\frac{\alpha}{2})} = \sum_{l=0}^{\infty} P_l(\cos\alpha) \ , \tag{2.10}$$

so that

$$\mathit{\Gamma}^{\phi,r}(\alpha,t) = \delta(t)\sum_{l=0}^{\infty} \phi_l^r P_l(\cos\alpha) \ , \tag{2.11}$$

where

$$\phi_l^r = \frac{ag}{m^e}. \tag{2.12}$$

This "Legendre sum" allows to establish in a *natural* way the spectral representation of the GF for the direct gravitational potential [27].

Now we can finally consider the deformable Earth. In this case, the change in mass distribution will be the sum of two contributions: the direct one that we have already presented and an indirect (or incremental) gravitational potential variation that we will call $\phi^e(\alpha,t)$ due to the elastic response of the Earth to the load. Hence, we make the hypothesis that, similar to $\mathit{\Gamma}^{\phi,r}$, the corresponding GF can be expressed as an expansion like:

$$\mathit{\Gamma}^{\phi,e}(\alpha,t) = \delta(t)\sum_{l=0}^{\infty} \phi_l^e P_l(\cos\alpha) \tag{2.13}$$

where coefficients ϕ_l^e are appropriate l-dependent coefficients; of course, we expect that $\phi_l^r \neq \phi_l^e$. The value of ϕ_l^e depends on the elastic properties of the adopted Earth model, and are ultimately determined by solving the equilibrium equations 2.38, 2.39, 2.40, 2.41. Following the ideas in the fundamental works of Love, and as we have just shown in Section 2.1, Eq. (2.4), we assume that, at a given harmonic degree l, coefficients ϕ_l^e are proportional to those of the direct potential variation:

$$\phi_l^e = k_l^{L,e}\phi_l^r, \tag{2.14}$$

where $k_l^{L,e}$ is the elastic LLN for the potential. Of course, for a rigid Earth, since no

displacement is possible, $k_l^{L,e} = 0$.

Then, the total potential GF for an elastic Earth is

$$\Gamma^{\phi}(\alpha, t) \equiv \Gamma^{\phi,r} + \Gamma^{\phi,e} = \delta(t)\frac{ag}{m^e}\sum_{l=0}^{\infty}(1 + k_l^{L,e})P_l(cos\alpha) \tag{2.15}$$

By Bruns formula [28], the change in height of the geoid equipotential surface is

$$N = \frac{\phi}{\gamma}, \tag{2.16}$$

where ϕ the perturbation of the gravitational potential and γ the local gravity acceleration. Hence, it is straightforward to obtain the GF for the geoid height variation, per unit mass and time, which reads:

$$\Gamma^{g}(\alpha, t) = \delta(t)\frac{a}{m^e}\sum_{l=0}^{\infty}(1 + k_l^{L,e})P_l(\cos\alpha)\ . \tag{2.17}$$

We Finally obtained the GF Γ^g, that is the total geoid surface displacement due to the load exerted by the point mass. Term "1" describes the direct geoid elevation change, term "$k_l^{L,e}$" describes the indirect effect due to the elastic yielding of the Earth. In analogy with $\Gamma^{\phi,e}$, the elastic GF associated with the vertical displacement field (along r) shall have the form:

$$\Gamma^{u,e}(\alpha, t) = \delta(t)\sum_{l=0}^{\infty}u_l^e P_l(\cos\alpha)\ ,$$

with u_l^e being an appropriate coefficient. However, since there is no rigid Earth contribution,

$$\Gamma^{u} = \Gamma^{u,e}\ ,$$

and defining the vertical LLN, $h_l^{L,e}$ by:

$$u_l^e = h_l^{L,e}\frac{\phi_l^r}{g} = h_l^{L,e}\frac{a}{m^e}$$

we have

$$\Gamma^u(\alpha,t) = \delta(t)\frac{a}{m^e}\sum_{l=0}^{\infty} h_l^{L,e} P_l(\cos\alpha) \ . \tag{2.18}$$

Finally, along the same lines, the elastic GF for the horizontal displacement field is defined in a vector form, conveniently expanded in series of $\partial_\alpha P_l(cos\alpha)$:

$$\Gamma^{v,e}(\alpha,t) = \delta(t)\sum_{l=0}^{\infty} v_l^e \partial_\alpha P_l(\cos\alpha)\hat{\alpha}$$

Even in this case there is no rigid Earth contribution, so the total GF is

$$\Gamma^v = \Gamma^{v,e} \ ,$$

and once again we can define the horizontal LN $l_l^{L,e}$ by:

$$v_l^e = l_l^{L,e}\frac{\phi_l^r}{g} = l_l^{L,e}\frac{a}{m^e} \ ,$$

and we have

$$\Gamma^v(\alpha,t) = \delta(t)\frac{a}{m_e}\sum_{l=0}^{\infty} l_l^e \partial_\alpha P_l(\cos\alpha)\hat{\alpha} \ . \tag{2.19}$$

Lastly, we may write:

$$\begin{aligned}
\Gamma^g(\alpha,t) &= \frac{a}{m_e}\sum_{l=0}^{\infty}(\delta(t) + k_l^L(t))P_l(\cos\alpha) \\
\Gamma^u(\alpha,t) &= \frac{a}{m_e}\sum_{l=0}^{\infty} h_l^L(t)P_l(\cos\alpha) \\
\Gamma^v(\alpha,t) &= \frac{a}{m_e}\sum_{l=0}^{\infty} l_l^L(t)\partial_\alpha P_l(\cos\alpha)\hat{\alpha}
\end{aligned} \tag{2.20}$$

where

$$k_l^L(t) = k_l^{L,e}\delta(t), \qquad h_l^L(t) = h_l^{L,e}\delta(t), \qquad l_l^L(t) = l_l^{L,e}\delta(t) \ . \tag{2.21}$$

and $\hat{\alpha}$ is a unit vector lying on the sphere and parallel to the great circle passing through the observer $O(\theta, \lambda)$ and the impulsive load $\mu(\theta', \lambda')$ (see Figure 2.1).

2.3 Viscoelastic Load Love Numbers

In the framework of the viscoelastic normal modes (VNM) theory, Peltier (1974) and others have shown that for a 1-D Maxwell viscoelastic model the Loading Love numbers (LLNs) are causal functions, (i.e., one-sided functions vanishing for $t < 0$), characterised by two physically distinct *components*.

The first component (or elastic component, already described above) is in-phase with the $(\delta - like)$ impulsive load and only depends on the value of the elastic constants and density of layers. The second component (the viscous component) is discussed here, taking advantage of the existing literature. This component is sensitive to the rheological profile of the Earth, but it also depends upon the elastic parameters and density. Due to the delayed readjustment of the Earth, the viscous component is lagged with respect to the impulsive load. The viscous components of all the viscoelastic LLNs have a multi-exponential form [9]. The time-dependent k LLNs for a Earth with Maxwell generalised rheology have the general multi-exponential form:

$$\begin{aligned} k_l^L(t) &= k_l^{L,e}\delta(t) + H(t)\sum_{i=1}^{M} k_{li}^L e^{s_{li}t} \\ h_l^L(t) &= h_l^{L,e}\delta(t) + H(t)\sum_{i=1}^{M} h_{li}^L e^{s_{li}t} \\ l_l^L(t) &= l_l^{L,e}\delta(t) + H(t)\sum_{i=1}^{M} l_{li}^L e^{s_{li}t}, \end{aligned} \tag{2.22}$$

where the first term is the elastic component described in previous Section, and the second one is the viscous component, where each of the k_{li}^L (h_{li}^L, l_{li}^L) with $(i = 1, ...M)$ are the M viscous terms of the LLN, each one associated to a negative frequency $s_{li} = -1/\tau_{li} < 0$, where τ_{li} are the characteristic relaxation times of the Earth's model, and M is the number of VNMs, determined by the number and rheology of layers. By the viscoelastic normal mode method developed by Peltier [29], it has been established that this holds true for the classical (steady-state) Maxwell rheology but also for transient

rheologies like the Burgers' body. The values of the LLNs of degree $l = 1$ depend on the choice of the origin of the reference frame adopted to describe the deformation and the change in the geopotential. Normally, they are written in centre of mass (CM) reference frame of the system (Earth + Load).

By substituting those LNs in expressions 2.20 we obtain the viscoelastic time-dependent GFs:

$$\begin{aligned} \Gamma^g(\alpha,t) &= \frac{a}{m_e}\sum_{l=0}^{\infty}(\delta(t)+k_l^L(t))P_l(\cos\alpha) \\ \Gamma^u(\alpha,t) &= \frac{a}{m_e}\sum_{l=0}^{\infty}h_l^L(t)P_l(\cos\alpha) \\ \Gamma^v(\alpha,t) &= \frac{a}{m_e}\sum_{l=0}^{\infty}l_l^L(t)\partial_\alpha P_l(\cos\alpha)\hat{\alpha}\ , \end{aligned} \tag{2.23}$$

where:

$$\begin{aligned} k_l^L(t) &= k_l^{L,e}\delta(t)+H(t)\sum_{i=1}^{M}k_{li}^L e^{s_{li}t} \\ h_l^L(t) &= h_l^{L,e}\delta(t)+H(t)\sum_{i=1}^{M}h_{li}^L e^{s_{li}t} \\ l_l^L(t) &= l_l^{L,e}\delta(t)+H(t)\sum_{i=1}^{M}l_{li}^L e^{s_{li}t}\ . \end{aligned} \tag{2.24}$$

2.4 Generic Heaviside Load Love Numbers

In this work I will not consider the response to an impulsive load, since we are interested in computing the response of the Earth to the unloading consequent to the melting of an ice load. That's why in this section we will discuss how to obtain the Heaviside Love numbers (HLNs), which express the response of the Earth to a prolonged load: in other words, they represent the response of the planet to a creep experiment (see Section 1.2).

For simplicity, from now on we will denote in this section a generic LN as

$$x(t) = x_e\delta(t) + H(t)\sum_i x_i e^{s_i t} \ , \tag{2.25}$$

where we keep the l-dependence implicit to simplify the notation. This expression still describes the response to an impulsive forcing, and as said before, it can be split into an elastic component (the first term), and a viscous component (the second one). It can be demonstrated that, if the forcing has a heaviside step function form

$$H(t) = \begin{cases} 0, & t \leq 0 \\ 1, & t > 0 \end{cases} \tag{2.26}$$

Heaviside LLNs can be expressed by computing the time convolution

$$x^H(t) \equiv x(t) * H(t) = \int_{-\infty}^{\infty} x(t-t')H(t')dt' \ . \tag{2.27}$$

This holds if any load time history is used in place of $H(t)$, but for our purpose considering the Heaviside case will be enough. The previous expression leads to:

$$\begin{aligned} x^H(t) &= \int_{-\infty}^{\infty} x^\delta(t-t')H(t')dt' \\ &= \int_{-\infty}^{\infty} \left(x^e\delta(t-t') + H(t-t')\sum_i x^i e^{s_i(t-t')} \right) H(t')dt' \\ &= \int_{-\infty}^{\infty} x^e\delta(t-t')H(t')dt' + \int_{-\infty}^{\infty} \left(H(t-t')\sum_i x^i e^{s_i(t-t')} \right) H(t')dt' \ , \end{aligned} \tag{2.28}$$

where using the filter properties of the δ distribution, the first integral gives:

$$\int_{-\infty}^{\infty} x^e\delta(t-t')H(t')dt' = x^e H(t) \ . \tag{2.29}$$

As regards the second, we find:

$$\begin{aligned}
&\int_{-\infty}^{\infty} H(t-t')H(t')\sum_i x^i e^{s_i(t-t')}dt' = \int_0^{\infty} H(t-t')\sum_i x^i e^{s_i(t-t')}dt' \\
&= H(t)\sum_i x^i \int_0^t e^{s_i(t-t')}dt' = H(t)\sum_i x^i \left[-\frac{e^{s_i(t-t')}}{s_i}\right]_0^t \\
&= -H(t)\sum_i x^i \frac{1-e^{s_i t}}{s_i} \ ,
\end{aligned} \tag{2.30}$$

so, until now we have obtained:

$$x^H(t) = x^e H(t) - H(t)\sum_i x^i \frac{1-e^{s_i t}}{s_i} \tag{2.31}$$

but, by using the definition of Heaviside function, for $t > 0$, an equivalent form is

$$x^H(t) = x^e - \sum_i x^i \frac{1-e^{s_i t}}{s_i} \ . \tag{2.32}$$

It is interesting considering the case of a forcing acting in the opposite way as well, in other words a step function that for $t < 0$ assumes a constant value and vanishes in $t = 0$: $g(t) = 1 - H(t)$. This load history finds its physical equivalent in the unloading problem of an (ice) mass that, acting from a time $t = -\infty$, suddenly vanishes at $t = 0$. In this case we have:

$$x^{1-H}(t) = x^{\delta}(t) * (1 - H(t)) \ . \tag{2.33}$$

We have:

$$
\begin{aligned}
x^{1-H}(t) &= \int_{-\infty}^{\infty} x^{\delta}(t-t')(1-H(t'))dt' \\
&= \int_{-\infty}^{\infty} \left(x^e \delta(t-t') + H(t-t') \sum_i x^i e^{s_i(t-t')} \right) (1-H(t'))dt' \\
&= \int_{-\infty}^{\infty} \left(x^e \delta(t-t') + H(t-t') \sum_i x^i e^{s_i(t-t')} \right) dt' - \int_{-\infty}^{\infty} x^e \delta(t-t') H(t')dt' + \\
&\qquad - \int_{-\infty}^{\infty} \left(H(t-t') \sum_i x^i e^{s_i(t-t')} \right) H(t')dt' \\
&= x^e + \int_{-\infty}^{\infty} H(t-t') \sum_i x^i e^{s_i(t-t')} dt' - \int_{-\infty}^{\infty} x^e \delta(t-t') H(t')dt' + \\
&\qquad - \int_{-\infty}^{\infty} H(t-t') H(t') \sum_i x^i e^{s_i(t-t')} dt' \\
&= x^e + H(t) \sum_i x^i \int_{-\infty}^{t} e^{s_i(t-t')} dt' - x^e H(t) - H(t) \sum_i x^i \int_0^t e^{s_i(t-t')} dt' \\
&= x^e + H(t) \sum_i x^i \left[-\frac{e^{s_i(t-t')}}{s_i} \right]_{-\infty}^{t} - x^e H(t) - H(t) \sum_i x^i \left[-\frac{e^{s_i(t-t')}}{s_i} \right]_0^t \\
&= x^e - H(t) \sum_i \frac{x^i}{s_i} - x^e H(t) + H(t) \sum_i x^i \frac{1-e^{s_i t}}{s_i} \ .
\end{aligned}
$$

So that, for $t \geq 0$:

$$
x^{1-H}(t) = -\sum_i \frac{x^i}{s_i} + \sum_i x^i \frac{1-e^{s_i t}}{s_i} \ . \tag{2.34}
$$

Let's come back for a moment on Eq. (2.32), focusing the attention on the following limits:

$$
\textit{Elastic Limit}: \qquad \lim_{t \mapsto 0} x^H(t) = x_e \tag{2.35}
$$

$$
\textit{Fluid Limit}: \qquad \lim_{t \mapsto \infty} x^H(t) = x_e - \sum_i \frac{x_i}{s_i} \ . \tag{2.36}
$$

These are called the elastic and the fluid limits of the LNs; they represent respectively

the instantaneous and the long-term response. We will make use of them in order to demonstrate the validity of results (2.32) and (2.34).

Indeed, considering the combination of both load histories, $H(t)$ and $g(t)$, we obtain a constant load history: $H(t) + g(t) = H(t) + 1 - H(t) = 1$. This means dealing with a load acting from a time $t = -\infty$ and end at $t = \infty$. In terms of Love numbers, we expect that $x^H(t) + x^{1-H}(t) = x^f(t)$, that is the Love fluid number (eq. 2.36). Indeed,

$$x^H(t)+x^{1-H}(t) = x^e-\sum_i x^i\frac{1-e^{s_i t}}{s_i}-\sum_i \frac{x^i}{s_i}+\sum_i x^i\frac{1-e^{s_i t}}{s_i} = x^e-\sum_i \frac{x_i}{s_i} = x^f. \quad (2.37)$$

2.5 Analytical form of Load Love Numbers

Until now an analytical expression of the LNs has not been established.

For doing so, we have to evaluate the displacement and the gravitational potential variation for the chosen Earth model. This means solving a *simultaneous* set of equations, including momentum equation, continuity equation, the constitutive equation and the Laplace equation for the Earth potential with appropriate regularity and boundary conditions. If we consider the simpler case of an homogeneous and incompressible Earth, with a constant value of density, viscosity and elastic parameters, the equations can be written in a simplified form [30]:

$$\textit{Momentum Equation}: \quad \nabla \cdot \sigma + \rho\vec{g} = 0 \quad (2.38)$$

$$\textit{Continuity Equation}: \quad \nabla \cdot \vec{u} = 0 \quad (2.39)$$

$$\textit{Laplace Equation}: \quad \nabla^2\phi = 0 \quad (2.40)$$

$$\textit{Constitutive Equation}: \quad \sigma = \sigma(\epsilon, \dot{\epsilon}, ..., \vec{p}) \quad (2.41)$$

where σ is the stress tensor, ρ the density, $\vec{g}$ the gravitational acceleration, $\vec{u}$ the displacement field, ϕ the gravitational potential at the exterior of the solid Earth and the symbols $\nabla\cdot$ and ∇^2 indicate respectively the divergence and the Laplacian.

Even if we consider the simplified system of Eqs. (2.38 - 2.41), the resolution of this system is extremely difficult and requires many lines of calculations, and for more insight one can refer to [30]. Anyway, in the vast majority of cases, when we consider compressible or heterogeneous Earth model with two or more layers, it is even not assured

that a closed solution can be found analytically, and one should consider numerical methods.

Elastic Load Love Numbers for the Kelvin Model

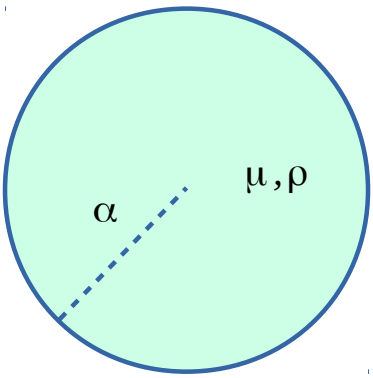

Figure 2.2: Representation of the Kelvin Model.

There exists, fortunately, another case in which the solution for the LLNs can *easily* be found analytically: it is the case of the so called Kelvin Model (KM) (Figure 2.2), firstly introduced by Thomson (later appointed Lord Kelvin) [31]. In the elastic case, it consists of an homogeneous sphere, with radius a, density ρ and rigidity μ, and it can represent an average Earth model. In the viscoelastic one, the KM shall be characterised, in addition, by an appropriate number of rheological parameters, like viscosities. So basically, with respect the model described in the previous paragraph, we have relaxed the hypothesis of rigidity. Following [29], and solving Equations (2.38 - 2.41), the explicit expressions for the elastic incompressible KM LLNs are:

$$\begin{aligned} k_l^{L,e} &= -\frac{1}{1+\lambda_l \xi} \\ h_l^{L,e} &= -\frac{(2l+1)/3}{1+\lambda_l \xi} \\ l_l^{L,e} &= -\frac{1/l}{1+\lambda_l \xi} \end{aligned} \tag{2.42}$$

where

$$\lambda_l = \frac{2l^2 + 4l + 3}{l} \quad \text{and} \quad \xi = \frac{\mu}{\rho g a} \tag{2.43}$$

These expressions are valid for $l \geqslant 2$, since for $l = 0$ we can assume that all LLNs are zero in case of an impulsive point mass load. For $l = 1$, the choice of the reference frame affects the value of LLNs.

Viscoelastic Load Love Numbers for the Kelvin model

For the visco-elastic KM, it is possible to use the Correspondence Principle (see Section 1.3) of linear viscoelasticity to obtain the VE LLNs from the corresponding elastic expressions. For example, in order to obtain the VE solution corresponding to a Maxwell rheology, we substitute the elastic modulus μ with by the Maxwell complex modulus $\tilde{\mu}_M = \frac{\mu s}{s+\tau_M^{-1}}$, while at numerator we have the fluid limits:

$$\begin{aligned}
h_l^L(s) &= \frac{h_l^{L,f}}{1 + \lambda_l \frac{\mu_M(s)}{\rho g a}} \qquad \text{with} \quad h_l^{L,f} = -\frac{2l+1}{3} \\
k_l^L(s) &= \frac{k_l^{L,f}}{1 + \lambda_l \frac{\mu_M(s)}{\rho g a}} \qquad \text{with} \quad k_l^{L,f} = -1 \\
l_l^L(s) &= \frac{l_l^{L,f}}{1 + \lambda_l \frac{\mu_M(s)}{\rho g a}} \qquad \text{with} \quad l_l^{L,f} = -\frac{1}{l} \ ,
\end{aligned} \tag{2.44}$$

It is necessary to perform the Laplace inverse transform to obtain the LLNs in the time domain. Before doing so, we can try to modify the expressions (2.44), in order to simplify the inversion. Firstly, let's define $\epsilon^2 = \lambda_l \frac{\eta}{\rho g a}$. In this way, the generic LLNs become:

$$x_l^L(s) = \frac{x_l^{L,f}}{1 + \frac{\lambda_l \mu_M(s)}{\rho g a}} = \frac{x_l^{L,f}}{1 + \epsilon^2 \dfrac{s}{s + \frac{1}{\tau_M}}} = \frac{x_l^{L,f}(s + 1/\tau_M)}{1/\tau_M + s\epsilon^2 + s} \ . \tag{2.45}$$

If we gather in the denominator $(1 + \epsilon^2)$, we obtain:

$$x_l^L(s) = \frac{x_l^{L,f}(s + 1/\tau_M)}{(1 + \epsilon^2)(s + 1/\tau_{KV})} \ , \tag{2.46}$$

where $\tau_{KV} = \tau_M(1+\epsilon^2)$. So we have found:

$$x_l^L(s) = \frac{x_l^{L,f}}{(1+\epsilon^2)} \frac{(s+1/\tau_M)}{(s+1/\tau_{KV})} \ . \tag{2.47}$$

Defining

$$x^e = \lim_{s\to\infty} x(s) = \frac{x_l^{L,f}}{(1+\epsilon^2)} \tag{2.48}$$

we can write:

$$x_l^L(s) = x^e \ \frac{(s+1/\tau_M)}{(s+1/\tau_{KV})} \tag{2.49}$$

and with a little algebra we find:

$$x_l^L(s) = x^e \ \left(1 + \frac{(1/\tau_M - 1/\tau_{KV})}{(s+1/\tau_{KV})}\right) \ , \tag{2.50}$$

and if we define

$$x^v = \frac{x_f(\frac{1}{\tau_M} - \frac{1}{\tau_{KV}})}{(1+\epsilon^2)} \ , \tag{2.51}$$

reminding that $x^f = x^e(1+\epsilon^2)$, we finally obtain:

$$x_l^L(s) = x^e + \frac{x^f(\frac{1}{\tau_M} - \frac{1}{\tau_{KV}})}{(1+\epsilon^2)(s+\frac{1}{\tau_{KV}})} = x^e + \frac{x^v}{s+\frac{1}{\tau_l^{KM}}} \ , \tag{2.52}$$

with

$$x^v = \frac{x^f(\frac{1}{\tau_M} - \frac{1}{\tau_{KV}})}{(1+\epsilon^2)} \ . \tag{2.53}$$

This formulation for viscoelastic LLNs allows an easier inversion in the time domain:

$$x_l^L(t) = x^e\delta(t) + H(t)x^v e^{(-t/\tau_{KM})} \tag{2.54}$$

Following the terminology introduced by Wu and Peltier [30], this last formula is referred

to as the $M0$ viscoelastic mode of relaxation [9].

2.6 Andrade's Load Love numbers for the Kelvin's Sphere

By exploiting the Correspondence Principle, in this Section we will try to define the explicit form of LLNs for a planet uniform and homogeneous, with an Andrade rheology. It will be sufficient to substitute in Eqs. (2.44) the definition of Andrade complex modulus. Considering the potential Love Number

$$k_l^A(s) = \frac{k_l^{L,f}}{1 + \lambda_l \frac{\mu_A(s)}{\rho g a}}$$

and recalling the form of $\mu^A(s)$ (equation 1.40):

$$\begin{aligned}
\mu_A(s) &= \left\{ \frac{1}{\mu} \left[1 + \frac{\Gamma(\alpha+1)}{(s\tau_M)^\alpha} + \frac{1}{\tau_M s} \right] \right\}^{-1} \\
&= \left\{ \frac{1}{\mu} \left[1 + \frac{\Gamma(\alpha+1)\mu^\alpha}{(s\eta)^\alpha} + \frac{\mu}{\eta s} \right] \right\}^{-1} \\
&= \left\{ \frac{1}{\mu} \left[\frac{(s\eta)^\alpha + \Gamma(\alpha+1)\mu^\alpha + \mu(\eta s)^{\alpha-1}}{(s\eta)^\alpha} \right] \right\}^{-1}
\end{aligned}$$

by developing the exponent and multiplying numerator and denominator by $s\eta$ one obtains:

$$\mu_A(s) = \frac{\mu(s\eta)^{\alpha+1}}{(s\eta)^\alpha(s\eta+\mu) + s\eta\mu^\alpha\Gamma(\alpha+1)} \ .$$

By using this relationship in the expression of k_l^A, and making the fluid limits explicit, we have:

$$k_l^A = \frac{-1}{1 + \frac{\lambda_l \mu (s\eta)^{\alpha+1}}{\rho g a[(s\eta)^\alpha(s\eta+\mu) + s\eta\mu^\alpha\Gamma(\alpha+1)]}} \tag{2.55}$$

In the same way we can write the expressions for k_l^A and l_l^A:

$$h_l^A = -\frac{2l+1}{3\left(1+\dfrac{\lambda_l \mu (s\eta)^{\alpha+1}}{\rho g a[(s\eta)^\alpha (s\eta+\mu)+s\eta\mu^\alpha \Gamma(\alpha+1)]}\right)} \ , \tag{2.56}$$

$$l_l^A = \frac{-1}{l\left(1+\dfrac{\lambda_l \mu (s\eta)^{\alpha+1}}{\rho g a[(s\eta)^\alpha (s\eta+\mu)+s\eta\mu^\alpha \Gamma(\alpha+1)]}\right)} \ . \tag{2.57}$$

These last three expressions represent the value of the Laplace-transformed LLN for a spherical homogeneous planet (KM) obeying to Andrade's rheology. Contrary to expressions (2.44) their form is not multi-exponential. However, Eq. (2.55), (2.56) and (2.56), are defined in the Laplace transform domain, and they need to be inverse-transformed in the time domain. The problem is that this procedure is far from being immediate as in the Maxwell's case. To perform the inversion we need to consider an alternative numerical methods between the many proposed by the field of Numerical Analysis.

Chapter 3

ALMA: the planetary Love Numbers calculator

ALMA (the plAnetary Love nuMbers cAlculator) [32] is a Fortran 90 program that computes the tidal and the loading Love numbers of a spherically symmetric, incompressible, viscoelastic planet, using the Post-Widder-Gaver (PWG) Laplace inversion formula. In the classical approach, the relaxation of a planet subject to a load (that finds its physical application in the study of post-glacial or post-seismic deformations) is computed using normal-mode method [29], based on the application of the propagator technique [32]. This semi-analytical approach allows to compute the response of an Earth model whose rheological parameters vary arbitrarily with depth. However, this method requires to perform the inverse transform of the LLNs expression. In the case of Andrade's rheology, whose explicit expressions for LLNs are reported in Section 2.6, Eqs. (2.55 - 2.57), this can not be done in a straightforward way through the Bromwhich integral method. With ALMA, this step is by-passed by using instead the PWG formula to transform the solution from the Laplace domain, back into the time domain.

In this Chapter a brief introduction about NM method is presented in Section 3.1, as well as a description of the PWG method used by ALMA in Section 3.2; Then, in Section 3.3, we will briefly describe the code, and finally in Section 3.4 some of the results will be reported. Here I remark that In this Chapter and in the following, we will use n to refer to the harmonic degree, in place of l.

3.1 Viscoelastic normal Mode: theory and drawbacks

The solutions of the equilibrium equations of a spherically symmetric Earth subject to a surface load are usually expressed in terms of the so called load-deformation coefficients, that are the LLNs. We already used this solutions, but in this Section we will see briefly how they can be obtained by following the procedure described in [29], well known as viscoelastic normal mode method (VNM). This technique implies a layer-by-layer propagation of the fundamental solution of the equilibrium equation (2.38) in the Laplace domain, and the solution of the secular equation whose roots determine the spectrum of relaxation of the Earth [33]. Within the normal-mode method, the Love numbers can be obtained solving a boundary value problem in the Laplace domain that involves the use of the matrix propagation technique. Let's consider the case of an incompressible Earth model that includes an elastic lithosphere on top of a stack of L homogeneous viscoelastic layers, and a homogeneous, inviscid core [33].

The interfaces between layers are at radii r_i, with $i = 0, 1, ..., L + 2$, where $r_0 = 0$, r_1 is the core-mantle boundary and r_{L+2} is the free surface of the Earth. Within each layer, for any harmonic degree n, the solution vector containing vertical and horizontal displacements and stresses, the incremental potential and its gradient can be written as

$$\vec{y}(r, s) = Y_k(r, s)\vec{c}_k(s) \quad r_k < r < r_{k+1} \text{ for } k = 1, ...L + 1, \tag{3.1}$$

where Y_k is the 6×6 fundamental matrix referring to the kth layer, and the elastic lithosphere is labelled by $k = L + 1$. In agreement with the Correspondence Principle of linear viscoelasticity, the matrix Y_k depends on the variable s through the complex shear modulus $\tilde{\mu}(s)$, and therefore it is determined by the elastic parameters of each layer (for example from the rigidity μ and the viscosity η in case of a Maxwell layer). If we impose the necessary boundary conditions (continuity conditions for all of the field variables across the mantle boundaries and the lithosphere-mantle boundary, as well as appropriate boundary conditions at the core-mantle boundary) then the solution vector at the Earth's surface can be written as:

$$\vec{y}(a, s) = WJ\vec{K} \ , \tag{3.2}$$

where the s-dependence is implicit at the right-hand side, J is the interface core-mantle matrix, W is the propagator

$$W(r,s) = \prod_{j=L+1}^{1} Y_j(r_{j+1}) Y^{-1}(r_j), \tag{3.3}$$

and the constant $\vec{K}$ is to be determined imposing the surface boundary conditions. These can be imposed exploiting a projection matrix P_b that extracts from $\vec{y}(a,s)$ the three known components at the surface (vertical and horizontal stress, and gradient of the geopotential):

$$P_b \vec{y}(a,s) = \vec{b} f(s) \ , \tag{3.4}$$

where $\vec{b}$ is given by [34] and $f(s)$ is the Laplace transform of the time-history of the point-like surface load. Introducing a further projection matrix such that

$$P_x \vec{y}(a,s) = \vec{x}(a,s) \equiv [u, v, \phi]^t(a,s) \ , \tag{3.5}$$

(where u, v are the vertical and horizontal displacement field and ϕ is the incremental potential) and using it with Eq. (3.4) in (3.2) we obtain:

$$\vec{x}(a,s) = P_x W J (P_b W J)^{-1} f(s) \vec{b} \ . \tag{3.6}$$

Then, using the definitions of Love numbers in the Laplace domain

$$\begin{aligned} h(s) &= \frac{m_e}{a} u(a,s) \\ l(s) &= \frac{m_e}{a} v(a,s) \\ k(s) &= -1 - \frac{m_e}{a g_a} \phi(a,s) \end{aligned} \tag{3.7}$$

and the residues theorem, we finally obtain the spectral form of the Love numbers:

$$\tilde{x}(s) = \left(x_e + \sum_{k=1}^{M} \frac{x_k}{s - s_k} \right) f(s) \ , \tag{3.8}$$

where $\tilde{x}$ is the Laplace transform of any of the three Love numbers and M is the number of viscoelastic modes. The terms s_k in Eq. (3.8) are the roots of the *secular equation*

$$Det(P_b W J) = 0 \tag{3.9}$$

and $x_k, (k = 1, ..., M)$ are the associated residues, with x_e representing the limit for large s values in the case of an impulsive forcing ($f(s) = 1$). Finally, we remark that the Love numbers have a multi-exponential form in the time domain, as it is possible to see by inverting expression above. Despite its success, the normal-mode method is characterized by several shortcomings, mostly associated with the resolution of the secular equation [33].

Here we summarize the main ones:

- In incompressible models, the number of roots of the secular equation increases linearly with increasing number of layers [32]. If compressibility is accounted for, a denumerable infinite number of modes appear even for an homogeneous Earth [42];
- At large harmonic degrees, the roots s_k of Eq. (3.8) become closely spaced and sometimes difficult to resolve [41];
- There is no way to determine *a priori* where the most significant roots are placed along the real negative axis, and neglecting some roots may lead to a loss of precision, with possible catastrophic consequences;
- One wrongly identified root may cause errors in the computation of the residue that may affect the whole time dependence of the Love numbers;

These are some of the motivations that encouraged several research groups to find out new methods for computing LLNs of $1D$-layered Earth models.

3.2 The Post-Widder-Gaver method

An alternative to VNM is exploited in `ALMA` [32], which performs a numerical Laplace inversion of Eq. (3.6) using the Post–Widder formula [35][36][37]:

$$f(t) = \lim_{n \mapsto \infty} \frac{(-1)^n}{n!} \left(\frac{n}{t}\right)^{n+1} \hat{f}^{(}n) \left(\frac{n}{t}\right) \text{ with } t > 0 \ , \tag{3.10}$$

where $\hat{f}$ represents the Laplace transform, and $\hat{f}^{(n)}$ is the nth s-derivative of $\hat{f}$.

This formula is a shortcut that allows to directly obtain the Laplace anti-transform in terms of derivatives of the transform, without the need of applying the traditional inverse Laplace formula. It is true that other formulas exist for the inversion of the Laplace transforms, that do not involve the nth derivative, but they are characterized by other complexities, and the PW is formally simple and easy to program [33]. However, if a closed-form expression for $\hat{f}^{(n)}(s)$ is not available, Gaver [38] has shown that $f(t)$ can be approximated by a sequence of functions

$$f_n(t) = (-1)^n \frac{n\alpha}{t} \binom{2n}{n} \Delta^n \hat{f} \left(\frac{n\alpha}{t}\right), \quad n = 1, 2, ..., N \tag{3.11}$$

where $\binom{n}{k}$ is the binomial coefficient, N is the maximum order of the sequence, $\alpha = \ln\ 2$ and Δ is the forward difference operator, that is $\Delta f(nx) = f((n+1)x) - f(nx)$. In their work, Abate and Valkò [39] shown that it is possible to write

$$f_n(t) = G_n^n, \tag{3.12}$$

with the recursive algorithm:

$$\begin{aligned} G_0^k &= \frac{k\alpha}{t} \hat{f} \left(\frac{k\alpha}{t}\right) \qquad 1 \leqslant k \leqslant 2N, \\ G_n^k &= \left(1 + \frac{k}{n}\right) G_{n-1}^k - \left(\frac{k}{n}\right) G_{n-1}^{k+1} 1 \leqslant n \leqslant N; \quad 1 \leqslant k \leqslant 2N - n \end{aligned} \tag{3.13}$$

where the G_n^k are called the "Gaver functionals".

This last three equations are the basis of the so called PWG method. The PWG approach allows to compute directly the Laplace inverse of $\hat{x}(a, s)$ and to derive the

Love numbers for any value of t. Since for a stable, stratified and incompressible Earth all of the poles of $\hat{x}(a,s)$ are located on the negative axis, in the PWG approach the Laplace transform $\hat{f}$ is sampled in a singularity-free region. With this method we can bypass both the analytical inversion of the array P_bWJ in Eq. (3.6) and the root-finding procedures that are needed to solve the secular Eq. (3.9), and this implies, in terms of code, *enormous semplifications* [33]. Following this procedure we will lose the standard normal-mode spectral form of the LN, so if the individual normal modes (s_i, l_i) and the elastic term l_e are needed, they must be obtained by non-linear regression. However, the simplicity of the PWG method has its drawbacks [33]:

- The sequence has a logarithmic convergence: we will need a large number of terms to obtain a sufficiently large number of significant digits in the inverse function;
- Since the evaluation of $f_n(t)$ demands the computation of $\hat{f}$, the PWG approach, like the normal-mode one, should become more inefficient as the number of viscoelastic layers grows;
- Gaver recurrence is known to be numerically unstable and to lead to catastrophic cancellation above some finite, threshold value of N.

Nonetheless, with respect of the normal mode method, the advantages of the PWG approach are:

- The numerical solution of the secular equation is no longer necessary;
- Love numbers are directly computed in the time domain for any time history;
- The algebraic structure of the numerical codes is greatly simplified;
- The method can be extended to (possibly compressible) finely layered models in a straightforward manner, as well as to arbitrary linear viscoelastic rheologies.

3.3 `ALMA`: some details

`ALMA` has been developed using the IBM XL Fortran 90 compiler and has been tested on a 1.5 GHz Macintosh Power PC G4. Program `alma.f90` has been built from scratch; `ALMA` is executed by the bash shell script `alma.sh`, and can be configured using the

Fortran "include" file `alma.inc`.

In Fig 3.1 we can see one example of the configuration file I used for my tests. It is

```
! ========================================================================
! ALMA configuration file
! ========================================================================
!
! ~~~~~~~~~~~~~~~~~~~~~~
! # General parameters
! ~~~~~~~~~~~~~~~~~~~~~~
!
 256                        ! number of digits
 8                          ! order of the Gaver sequence
!
 Loading                    ! LN type ('Loading' or 'Tidal')
!
1000                        ! Minimum degree
9900                        ! Maximum degree
100                         ! Step
!
!
 log                        ! Time scale ('log' / 'lin' / 'ext')
100                         ! Time points (minus one)
 -6 6                       ! Time range  (10^(m1:m2) kyrs)
!
! ~~~~~~~~~~~~~~~~~~~~~~
! # Rheological model
! ~~~~~~~~~~~~~~~~~~~~~~
!
 4                          ! Number of layers
!
! rheological_profiles/GS00-burgers.dat
! rheological_profiles/GS00-andrade.dat
! rheological_profiles/GS00-maxwell.dat
! rheological_profiles/BJ97.dat
 rheological_profiles/BJ97_Andrade_Inf.txt
!
! ~~~~~~~~~~~~~~~~~~~~~~
! # Log file
! ~~~~~~~~~~~~~~~~~~~~~~
!
alma-test.log
!
!
! ~~~~~~~~~~~~~~~~~~~~~~
! # Output files
! ~~~~~~~~~~~~~~~~~~~~~~
!
Real                        ! 'Real' or 'Complex' LNs
!
ln_vs_n                     ! Output file format (LNs vs t or LNs vs n)
!
h_10000_AI_lam.dat
l_10000_AI_lam.dat
k_10000_AI_lam.dat
!
!
!
! ========================================================================
! End of ALMA configuration file
! ========================================================================
```

Figure 3.1: `ALMA`'s configuration file.

divided into four Section:

- **General parameters**: in this section I set the parameters, choosing the number of significant digits, the order of the Gaver sequence, the LN type (tidal or load), the range of degrees of the LN, as well as the step, and lastly the desired time interval.

- **Rheological model**: this section tells `ALMA` which rheological model is to be used.

The rheological models used will be described in the following tables.

- **Output files**: In the last section it is possible to set the names of the output files. One can chose the file format which gives LNs as a function of time or LNs as a function of harmonic degree.

3.4 Computing Love numbers with ALMA

In the following pages the results I obtained using ALMA will be presented. For this work used the latest version, ALMA[3].

Calibration

At first I needed to calibrate and set all the parameters in the correct way. So I used Spada 2008 [32] as a benchmark, and I tried to reproduce the results shown in that paper. The following two plots 3.2 and 3.3 are the outcomes of this work.

I used the Earth model introduced by Bills and James (BJ97) [40] (for details about the values of the parameters, see Table 3.1), a simple 4-layer Earth model with an elastic lithosphere, a 2-layer Maxwell mantle and an inviscid fluid core. I configured ALMA to compute the two asymptotes of LNs for a Heaviside function, conventionally referred to as the "elastic LNs" (in other words the short-term behaviour for $t \longrightarrow 0$, that I obtained setting $t = 10^{-6}yr$) and the "fluid LNs" (obtained when one considers the long-term behaviour $t \longrightarrow \infty$, so I set $t = 10^{6}yr$). In the title of Figures 3.2 and 3.3, nla is for "number of layers", referring to the number of layers in the mantle, nsd is the number of significant digit, while ng is the order of the Gaver method (see [38]). All these are parameters that ALMA requires.

In both asymptotes, the LLNs of lower degrees have quite different values, but then, as the harmonic degree increases, they tend to a similar value close to zero (see Figures 3.2 and 3.3).

Radius $m \cdot 10^3$	**Density** $kg/m^3 \cdot 10^3$	**Rigidity** $Pa \cdot 10^{11}$	**Viscosity** (Pa·s·10^{21})	**Rheology**
6371	2.771	0.315	∞	elastic
6271	4.120	0.954	1	Maxwell
5701	4.508	1.990	2	Maxwell
3480	10.925	0	0	fluid

Table 3.1: Parameters for Bills and James (1997), a 4−layer Earth model proposed in [40]. In the last columns the written description "elastic", "Maxwell" and "fluid" indicate the rheological law to be used.

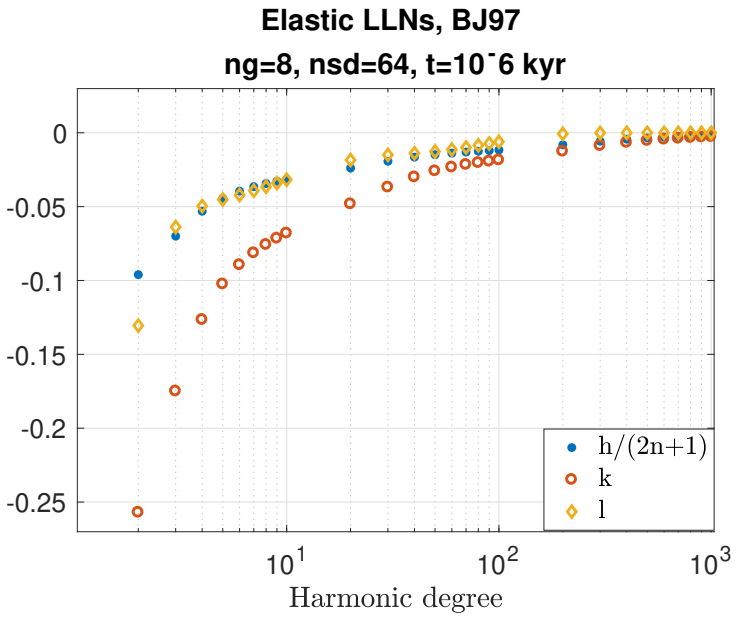

Figure 3.2: Elastic LLns k, h and l as a function of the harmonic degree for Earth model BJ97. The lower degrees of h, k and l assume different values while at higher degrees $> 10^2$ they tend to zero. The scale is semi-log.

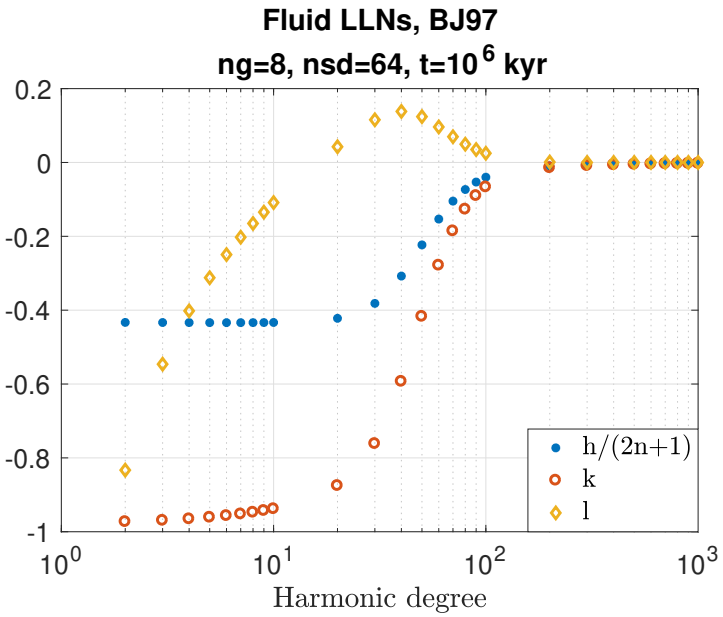

Figure 3.3: Fluid LLNs k, h and l as a function of the harmonic degree for Earth model BJ97. Even in this case the lower degrees of h, k and l assume different values while at higher degrees they all tend to zero. The scale is semi-log.

Then I used a more complex Earth model: VSS96, introduced in [42], in which a detailed rheological layering is adopted for the mantle, with 28 Maxwell layers (`nla`= 28), an inviscid fluid core and an elastic lithosphere. Even in this case I considered the elastic (Figure 3.4) and the fluid limit. In particular, in the fluid limit, I tested for which value of `nds ALMA` showed instabilities. These latter reflect the known singularity of the matrix Y^{-1} for $s \to 0$ and the increased numerical noise introduced by the large number of products in Eq (3.3) [43]. I found `nsd` = 32 (Figure 3.5), although in [32] it was found that `nsd` = 64. I have made two assumptions to justify this discrepancy: either the difference in the `nsd` value is due to the different Earth model used (in the paper the authors use another 30-layer model, different from VSS96), or the `ALMA`'s version I'm using, that is an upgraded one with respect the one used in [32], has a superior precision and stability.

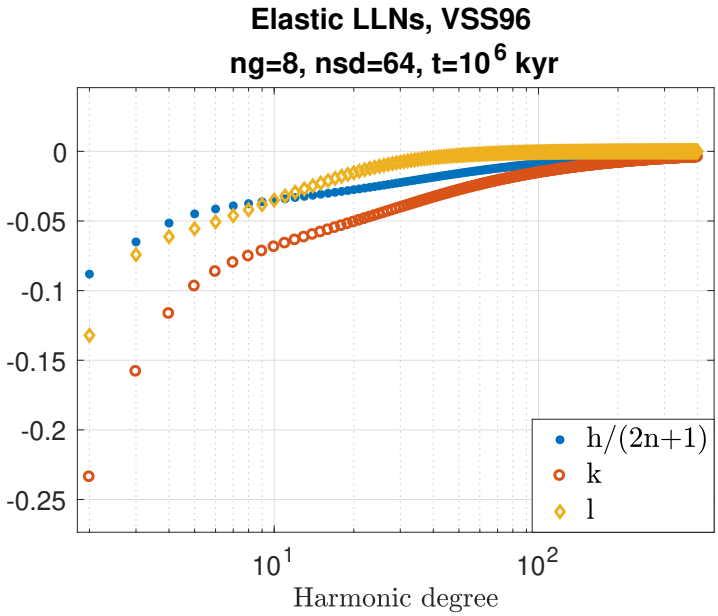

Figure 3.4: Elastic LLNs k, h and l as a function of the harmonic degree for Earth model VSS96. The scale is semi-log.

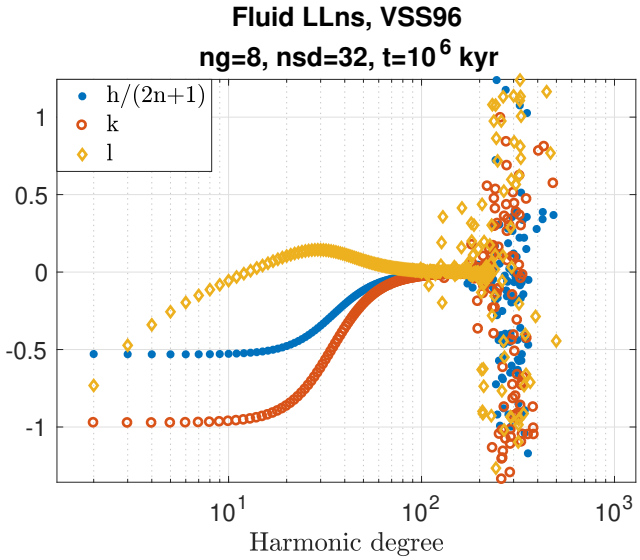

Figure 3.5: Fluid LLNs k, h and l as a function of the harmonic degree for Earth model VSS96. Here is the case in which nsd= 32 and, as mentioned above, at degree $n > 10^2$ the instability explodes. The scale is semi-log.

To close this first set of experiments, I produced a plot showing the trend of LLNs of degrees $2, 4, 8, 16, 32, 64$ as a function of time, produced using model BJ97. Here I report the case of h (Figure 3.6). Even in this case I had the opportunity to compare my results with the ones reported in [32], and the correspondence was more than satisfactory. As we can notice in Figure 3.6, their trend is almost the same: from an initial value included between 0 and 2, at a time that varies from 10^{-1} $kyrs$ to 10^{0} $kyrs$, it starts decreasing, with different slopes, until it reaches a new lower constant value.

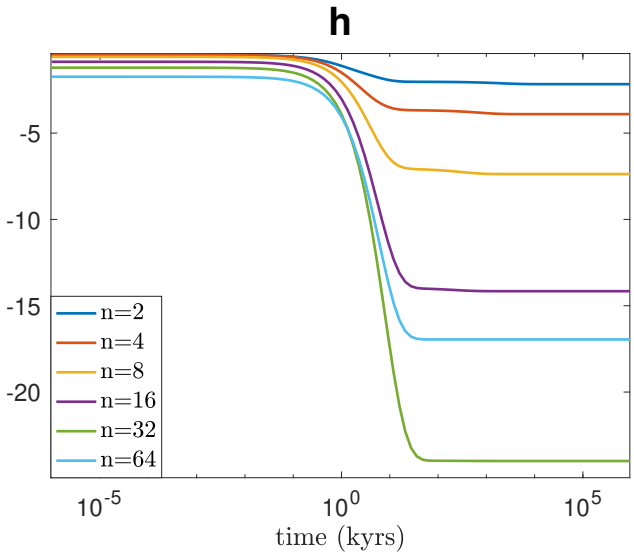

Figure 3.6: Love load number h as a function of time, for various harmonic degrees. Note that the scale is semi-log.

Comparison between Andrade's and Maxwell's rheologies in a 3-layer Earth

In a second stage I started some experiments more pertinent to my work. In particular, I started considering a simple 3−layer Earth model, GS00 (Table 3.4), with a fluid core, a homogeneous mantle and an elastic lithosphere. I configured `ALMA` to produce the h, k and l LLNs for two different cases: in the first case, the mantle behaves like a Maxwell's body, in the second like an Andrade's one. `ALMA` considered for the two cases the same parameter values, reported in Table 3.4, but in the mantle layer consider the presence of a Maxwell's rheology or an Andrade's one, depending on the case.

Radius $m \cdot 10^3$	**Density** $kg/m^3 \cdot 10^3$	**Rigidity** $Pa \cdot 10^{11}$	**Viscosity** (Pa·s)	**Rheology**
6371	3.300	0.28	1	Elastic
6271	4.518	1.45	1	Maxwell/Andrade
3480	10.977	0	0	Fluid

Table 3.2: Parameters for GS00, a 4−layered Earth model. In the last columns the written description "elastic", "Maxwell", "fluid" indicate to `ALMA` which kind of rheological behaviour attribute the parameters.

To make `ALMA` do this, it is sufficient to set the last column of the configuration file (the file in which are described all the elastic and rheological parameters of each layer) with the required rheology, typing `Maxwell` or `Andrade`. In Figure 3.7 we can see the outcomes of h for degree $n = 2$. In the following Figure 3.8 I show the result also for k and l, and even for higher harmonic degrees ($n = 53$, $n = 87$).

We can notice that the main differences are in the central part of the plot, and in general we can see that Andrade's LLNs follow a smoother trend. Moreover we can see that the Andrade's trend tends to deviate earlier from the elastic value with respect the Maxwell's one.

To investigate of the discrepancy between the first case and the second one, I plotted for different degrees ($n = 2$, $n = 53$, $n = 87$) the ratio $\frac{Andrade}{Maxwell}$. In Figure 3.9 it is clear that they reach their maximum amplitude for times $10^{-1} \leq t \leq 1\ kyr$. Of course this ratio has significance only when LN for the Maxwell model are different from 0. Unfortunately, as we can notice already in Figure 3.8, for high degrees, like

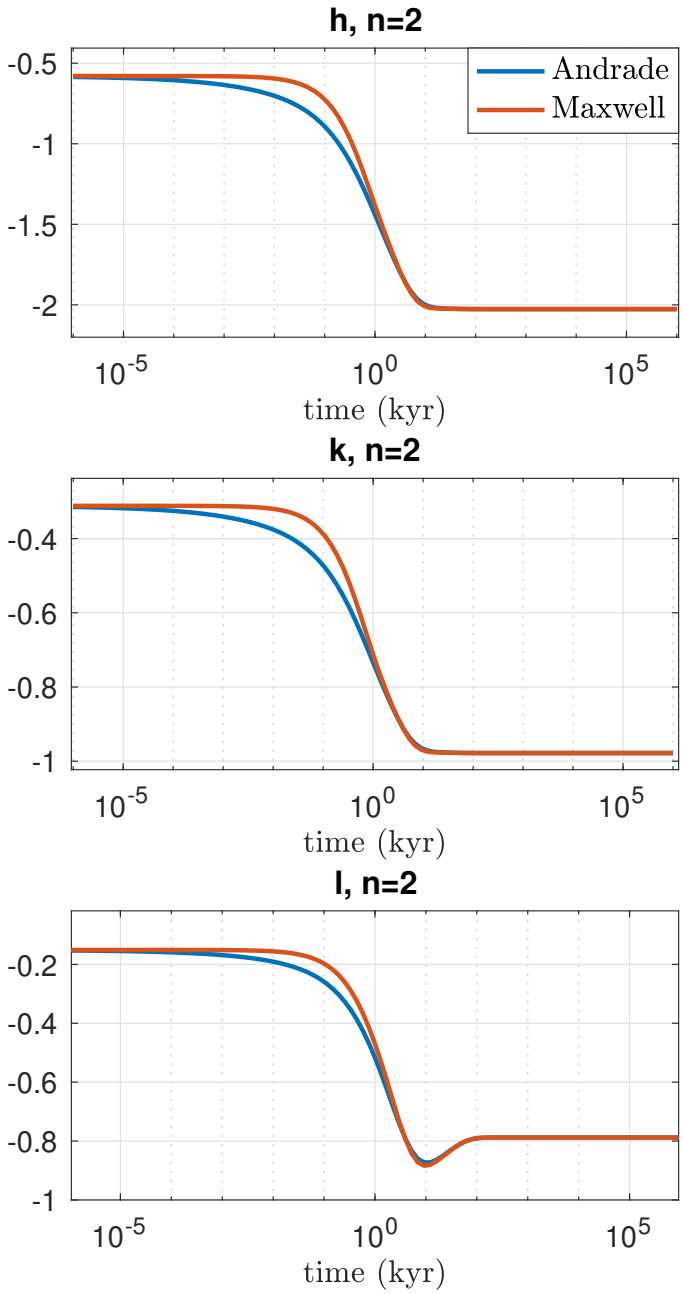

Figure 3.7: Comparison between Andrade's and Maxwell's results for LLNs h, k and l, for $n = 2$. The scale is semilog.

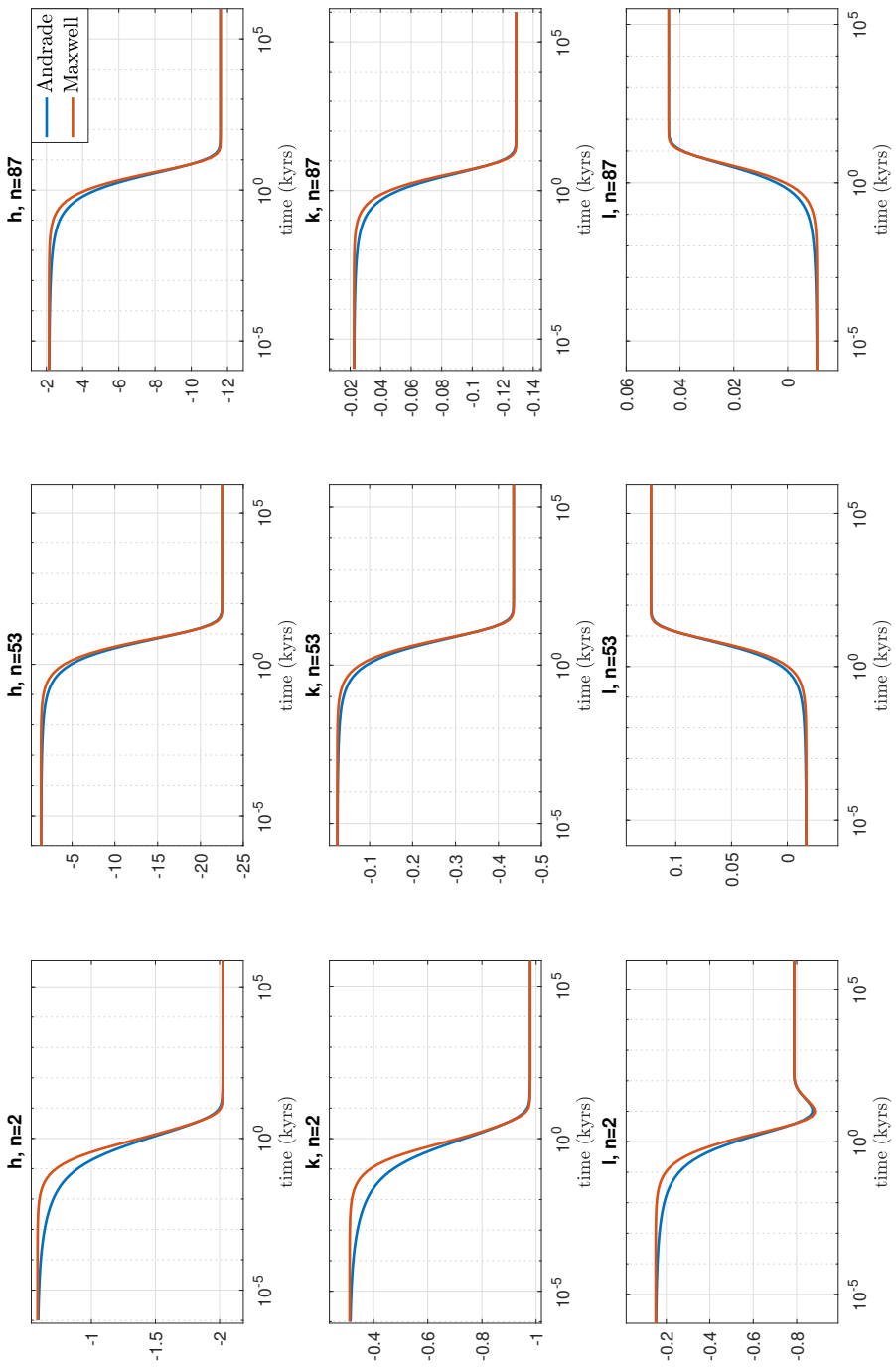

Figure 3.8: Comparison between LLNs produced by two different 3-layered Earth model, having respectively a mantle responding to Maxwell's model and to Andrade's model. The results are reported for the three LLNs and for the harmonic degree $n = 2, 53, 87$. The scale is semilog.

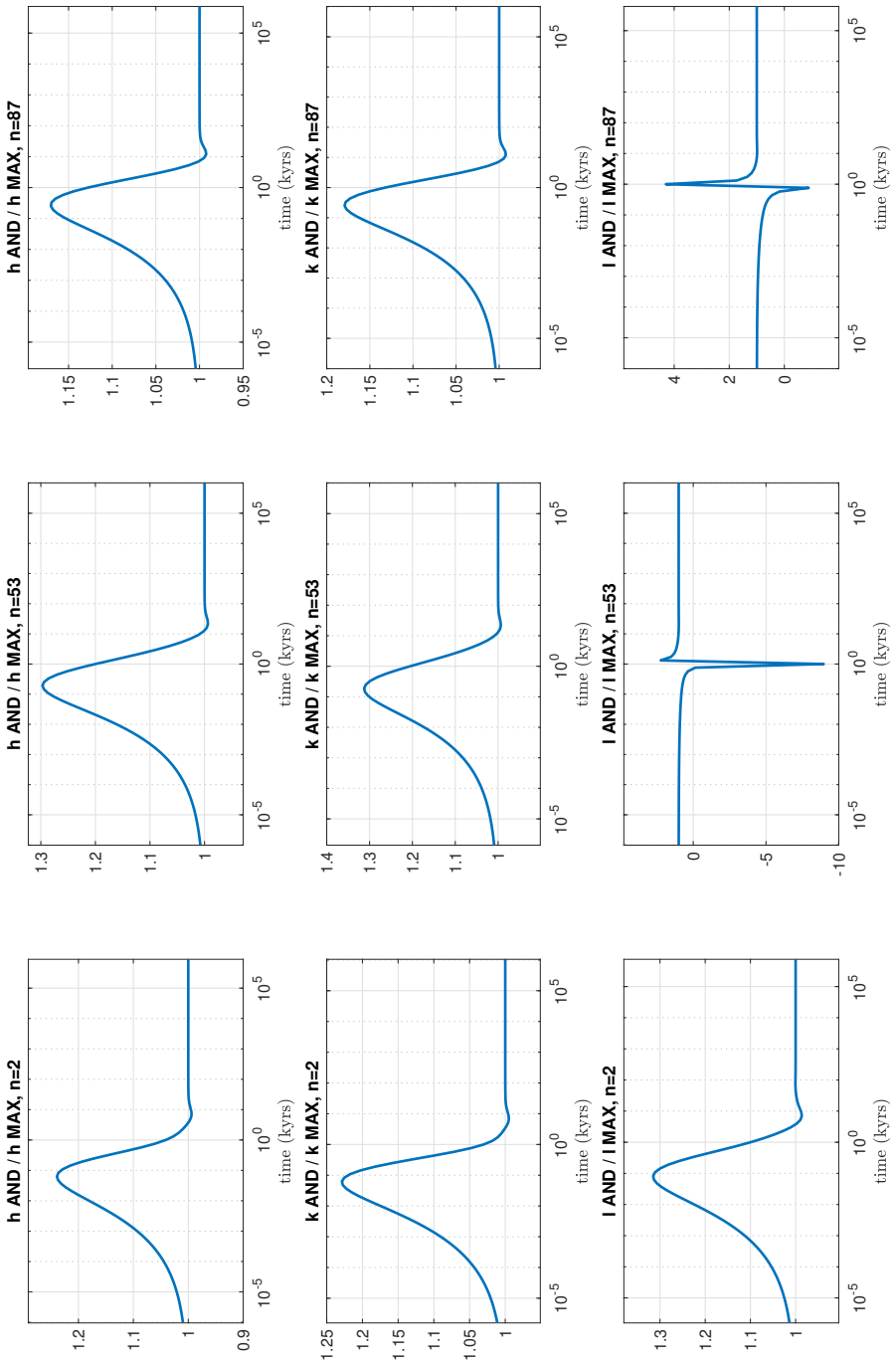

Figure 3.9: Ratio between LLNs computed with Andrade and Maxwell rheologies in the mantle. The maximum amplitudes are reached in a time interval $10^{-1} \leq t \leq 1$ $kyrs$. The results are reported for the three LLNs and for the harmonic degree $n = 2, 53, 87$. The scale is semilog.

$n = 53,\ n = 87$, the l LLNs cross the zero, creating in plots 3.9, 3.12 singularities which have no physical meaning. The last set of Figures (3.10, 3.11, 3.12) shows once again the ratio $\frac{Andrade}{Maxwell}$, but for more harmonic degrees ($n = 2, 4, 8, 16, 32, 48$).

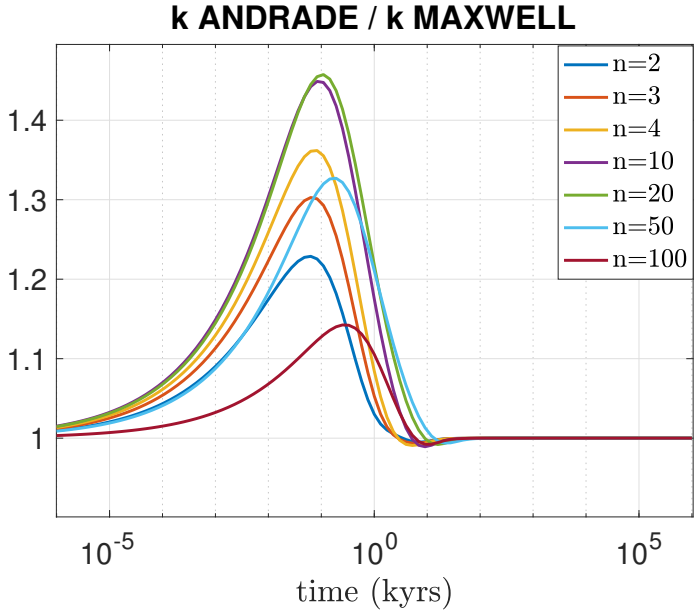

Figure 3.10: Ratio $\frac{Andrade}{Maxwell}$ as a function of time for k LN. The maxima are reached for times that go from $t = 10^{-1}\ kyrs$ for the lower degrees, to almost $t = 1\ kyrs$ for the higher degrees. The scale is semilog.

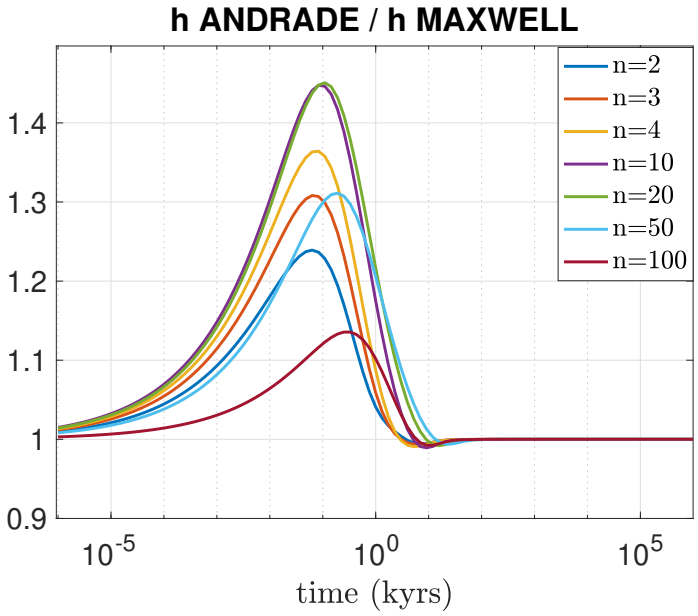

Figure 3.11: Ratio $\frac{Andrade}{Maxwell}$ as a function of time for h LN. Their trend is very similar to the k's one. The scale is semilog.

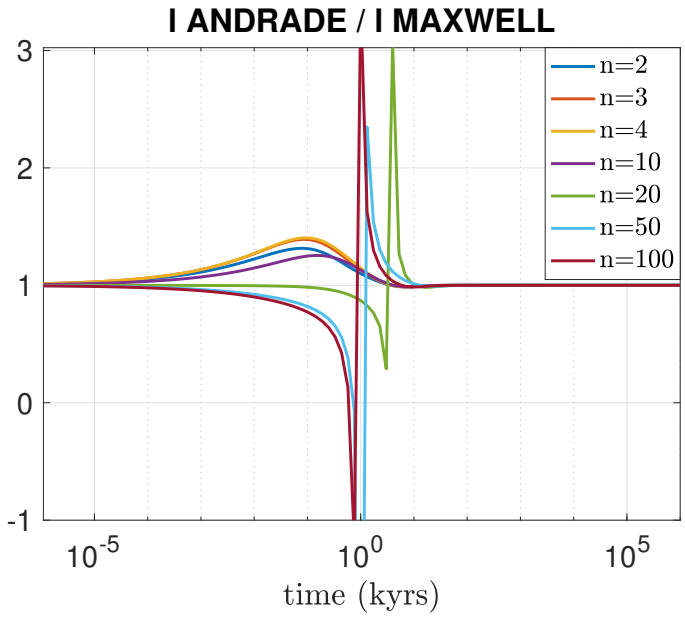

Figure 3.12: Ratio $\frac{Andrade}{Maxwell}$ as a function of time for l LN. The singularity has no physical meaning and it is only do to the fact that, for higher degrees ($n = 20, 50, 100$), both values of Maxwell and Andrade's LLNs cross the 0. The scale is semilog.

To conclude this Section, I would like to underline the main findings of this first set of experiments: Andrade's LLNs follow a smoother time evolution with respect to Maxwell's ones. This fact reflects the presence of the transient, or, in other words, a more gradual transition from the initial (elastic) response, to the long-term viscous one. However, as it is even more clear in the figure in which I plotted the ratio $\frac{Andrade}{Maxwell}$ (Figure 3.9 - 3.12), the differences, in terms of LLNs, manifest themselves only in a particular range of time, and they reach their maximum around $10^{-1\div 0}\ kyrs$. This means that there exists a particular range of times in which we are able to discern between the presence of a transient behaviour or not, and in the case of a point mass load that acts following a Heaviside step function, this time is set around $10^{-1\div 0}\ kyrs$. It is too early to make final considerations, since for an accurate analysis it would be better to include in our computations the presence of a load with finite physical dimensions and with a realistic load history, in order to simulate in the best way the unloading of an ice-sheet, and understand when (and where) it would be possible to measure the discrepancies between the two models, provided that these latter are actually measurable. For this reason in the next chapter I will introduce and discuss the problem of the $surface\ loading$, that will allow us to compute the expected deformation of the Earth to the unloading of a realistic load representing, for instance, a melting ice-sheet.

Chapter 4

Surface Loads: modelling Glacial Isostatic Adjustment

Any massive body above the Earth's surface represents, at the same time, a gravitational attractor and a load. In this way, atmosphere, oceans, rivers, ice sheets, volcanoes etc... are able to deform and modify the Earth's shape. The complexity of an accurate description of the deformation of the Earth under the effects of natural loads originates not from the number of possible loads, but especially from their reciprocal interaction. The Earth is a system composed of many other subsystems (the atmosphere, the cryosphere, the hydrosphere, the geosphere ...) that are inter-connected in a non-linear way. These interactions originate a huge number of geophysical phenomena whose interpretation is still source of discussion and debate among scientists. As an example of the extreme complexity of these kind of phenomena, let's suppose that we wish to estimate the expected displacement caused by the present-day melting of the Greenland ice sheet due to climate change. Unfortunately, it will not be enough to compute the deformation uniquely caused by the unloading due to the melting ice, but we will also have to take into account that the ocean will receive part of the melted water (while another part will be absorbed by the ground, and another part will evaporate), changing its mass and thus its load on the solid Earth, and then that the change in sea level will contribute in changing the coastline. Furthermore, even the loss of ice mass will imply a modification in the gravitational attraction that the lands exert on the water, contributing as well to the redistribution of the waters and in the modification of the coastline - and thus,

of the load. It is not over yet, since we have not considered that the melting of the ice sheet, and the subsequent redistribution of the water, will imply a chance in the inertia tensor of the planet, modifying the rotational motion to conserve angular momentum, and therefore, the Earth's shape.

The geophysical problem that we have just illustrated is known as "Surface Loading" problem, and aims to understand the amount of the deformation caused by the natural loading and unloading of the surface of our Planet. The first and simplest solutions came from Boussinesq (1885), who considered the response of a non-gravitating elastic half space to an applied surface point load. The solution he found, expressed in a cylindrical coordinate system (z, r, θ), is:

$$\begin{aligned} u_z &= \frac{P}{4\pi\mu R}\left[2(1-\nu)+\frac{z^2}{R^2}\right] \\ u_r &= \frac{P}{4\pi\mu R}\left[\frac{zr}{R^2}-\frac{(1-\nu)r}{R+z}\right] \\ u_\theta &= 0 \ , \end{aligned} \tag{4.1}$$

where u_z, u_r and u_θ are the vertical, the horizontal and the azimuthal displacements, μ is the shear modulus, ν the Poisson ratio, P the load magnitude and $R = \sqrt{r^2 + z^2}$ [9]. Even if this problem contained all the essential ingredients that appears in a more general case [29], its solutions gives a poor description of the complexity of the deformation, since it does not account neither the stratification of the Earth, nor the effects of a distributed load, and not even for any kind of gravitational effects.

Many progress in this field came after the introduction of the Green's function approach, originally proposed by Longman in 1962 [44] and then improved by Farrell [27, 29]. In this chapter we will see how, starting from the Green's functions previously introduced, it is possible, once we know the space and time evolution of the load, to compute the displacement, or better, computing the so-called $Surface\ Response\ Function$ (SRF).

4.1 Surface Response Function

The response of the Earth to a finite *variation* of surface load $\mathcal{L}$ is represented by the Surface Response Function [9]:

$$SRF = SRF(\gamma, t) \tag{4.2}$$

where $\gamma = (\theta, \lambda)$ are the point where SRF is evaluated. Depending on the type of response that is required, it is possible to define different $SRFs$, like that for the geoid height variation $\mathcal{G}$, for the vertical displacement $\mathcal{U}$, or for the horizontal displacement $\mathcal{V}$. Of course the SRF will depend not only on the evolution of the load, but also on the Earth model that we decide to employ (and therefore, on the LLNs).

Thus, all the SRFs have the general form:

$$SRF(\gamma, t) = (\mathit{\Gamma} \otimes \mathcal{L})(\gamma, t) = \int_{\infty}^{\infty} dt' \int_{e} \mathit{\Gamma}(\alpha, t - t')\mathcal{L}(\gamma', t')dA' \tag{4.3}$$

where:

- $\otimes$ is the spatio-temporal convolution operator,
- $\mathit{\Gamma}$ is the Green's function,
- $\int_e$ denotes the integration over Earth's surface, and
- α is the angular distance between the impulsive point load of the GF and the observer.

We remark that $\mathit{\Gamma}$ is determined exclusively by the choice of the Earth model, and therefore by the number and the characteristics of each layer, while the load function $\mathcal{L}$ depends on the geometry and evolution of the load [9].

For the following discussion, it will be useful to reduce the SRF to a standard spectral form. For doing so, at first we need to expand the load function in series of spherical harmonics:

$$\mathcal{L} = \sum_{nm} \mathcal{L}_{nm}\mathcal{Y}_{nm} \quad \text{with} \quad \mathcal{L}_{nm} = \frac{1}{4\pi}\int_{\gamma} \mathcal{L}(\gamma, t)\mathcal{Y}^{*}_{nm}(\gamma)d\gamma, \tag{4.4}$$

where $\mathcal{Y}_{nm}$ is the spherical harmonic function of degree l and order m, and $*$ denotes the complex conjugation. For the GF, we use the general form

$$\Gamma(\alpha, t) = \frac{a}{m_e} \sum_{n=0}^{\infty} x_n(t) P_n(\cos\alpha), \tag{4.5}$$

where $x_n(t)$ denotes one of the following combinations:

$$x_n(t) \equiv \begin{cases} \delta(t) + k_n^L(t), & \Gamma = \Gamma^g \quad \text{(Geoid height } \mathcal{G}) \\ h_n^L(t), & \Gamma = \Gamma^u \quad \text{(Vertical displacement } \mathcal{U}) \\ \ell_n^L(t), & \Gamma = \Gamma^\ell \quad \text{(Horizontal displacement } \mathcal{V}) \end{cases} \tag{4.6}$$

where we remark that for the horizontal displacement $\mathcal{V}$ it is necessary to consider in Eq. (4.5) the derivative with respect the spatial coordinates of the Legendre polynomial P_n.

Considering these definitions, let's perform the convolution (4.3) in order to find out the expansion in series of spherical harmonics of the SRF:

$$\begin{aligned} SRF(\gamma, t) &\equiv \int_{-\infty}^{\infty} dt' \int_e \Gamma(\alpha, t - t') \mathcal{L}(\gamma', t') dA' \\ &= \int_{-\infty}^{\infty} dt' \int_\gamma \left(\frac{a}{m^e} \sum_{t=0}^{\infty} x_n(t - t') P_n(\cos\alpha) \right) \cdot \left(\sum_{n'm'} \mathcal{L}_{n'm'}(t') \mathcal{Y}_{n'm'}(\gamma') \right) a^2 d\gamma' \\ &= \frac{a^3}{m^e} \int_{-\infty}^{\infty} dt' \int_\gamma \left(\sum_{n=0}^{\infty} \frac{x_n(t - t')}{2n+1} \sum_{m=-n}^{n} \mathcal{Y}_{nm}^*(\gamma') \mathcal{Y}_{nm}(\gamma) \right) \cdot (\cdots) d\gamma' \\ &= \frac{a^3}{m^e} \sum_{nm} \frac{\mathcal{Y}_{nm}(\gamma)}{2n+1} \int_{-\infty}^{\infty} dt' x_n(t - t') \sum_{n'm'} \mathcal{L}_{n'm'}(t') \int_\gamma \mathcal{Y}_{nm}^*(\gamma') \mathcal{Y}_{n'm'}(\gamma') d\gamma' \\ &= \frac{4\pi a^3}{m^e} \sum_{nm} \frac{\mathcal{Y}_{nm}(\gamma)}{2n+1} \int_{-\infty}^{\infty} x_n(t - t') \mathcal{L}_{nm}(t') dt' \\ &= \sum_{nm} SRF_{nm}(t) \mathcal{Y}_{nm}(\gamma) \ , \end{aligned} \tag{4.7}$$

with the harmonic coefficients:

$$SRF_{nm}(t) = \frac{1}{\rho^e}\frac{3}{2n+1}(x_n(t) * \mathcal{L}_{nm}(t)), \tag{4.8}$$

where $\rho^e = \frac{3m^e}{4\pi a^3}$ is the Earth's average density, and $*$ is the time convolution.

The Sea Level Equation

We have obtained an explicit expression for the SRF, but we still need to define the load variation function. The most complete approach to the definition of the SRF entails the resolution of the Sea Level Equation (SLE) [27].

The SLE is an integral equation defined by:

$$\Delta SL(\theta,\gamma,t) = \frac{\rho_i}{\gamma}\Gamma \otimes_i I + \frac{\rho_w}{\gamma}\Gamma \otimes_o \Delta SL - \frac{m_i(t)}{\rho_w A_o(t)} - \frac{\rho_i}{\gamma}\overline{\Gamma \otimes I} - \frac{\rho}{\gamma}\overline{\Gamma \otimes_o \Delta SL} \tag{4.9}$$

where:

- ΔSL is the change in sea level at point (θ,γ) between time t and some reference time t_0,
- I is the evolution of global ice thickness change,
- ρ_i and ρ_w are ice and ocean water densities, respectively,
- γ is the gravity acceleration,
- Γ represents a Green's function that describes perturbations to the solid Earth displacement field and the gravitational potential due to surface loading [29], [46],
- $\otimes_i$ and $\otimes_o$ represent convolutions in space and time over the ice sheets and the ocean, respectively,
- the third term is the eustatic term, where A_o is the ocean area and $m_i(t)$ is the variation of the ice mass.

The most common way of solving it [2], is using a pseudo-spectral approach (e.g. [45], [46]). The SLE is an extremely powerful mathematical tool, which allows us to

determine, for a chosen range of times, the evolution of the sea level, and thus, of the coastlines. Of course the resolution of the equation requires many efforts, reason for which it become natural asking if our load function has to be really so much detailed. As we will see in the next chapter, the regions in which the effects of the transient are visible include a finite range of angular distances, that depend on the original dimension and on the evolution of the load (the ice-sheet). This range is typically close to the physical boundaries of the load, and for this reason we are interested in the local response; the SLE instead, provides a global self-consistent solution for the variation of the sea level (and thus, the load) worldwide, while the nature of our problem is more local-scale size. For this reason, instead of solving the SLE, we can consider a *simplified load problem*, whose assumptions allow to find a closed solution in terms of vertical and horizontal displacement, and geoid height variation [9].

The simplified load problem

Assumptions

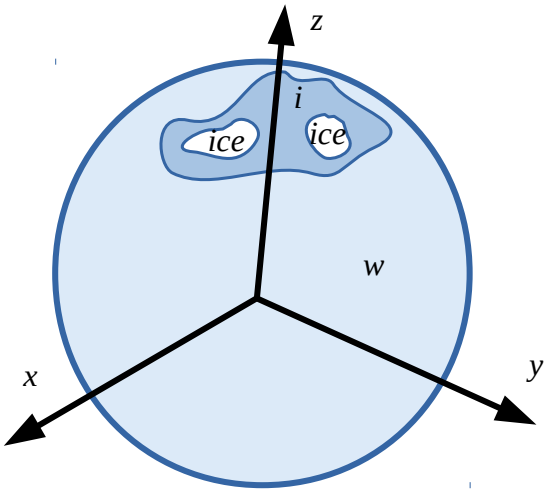

Figure 4.1: An illustration of the simplified loading problem. The ice can vary in space and time over the subset i, while the water thickness assumes a spatially uniform but time dependent value over the subset w.

The assumptions of the simplified load problem are the following: we will consider the load $\mathcal{L}$ as the sum of two contributions, the first, $\mathcal{L}_i$, accounts the variation of the

ice load, and the second, $\mathcal{L}_w$, refers to the water-covered region. The contribution $\mathcal{L}_i$ is known and can vary in space and time over a defined subset i; on the other hand, $\mathcal{L}_w$ is defined over the subset w that is disjoint to i, and represents a uniform load that assumes a constant value all over w. This representation is quite unrealistic, since the borders of w do not change. It is equivalent to assume that the topography is infinitely steep so that coastlines do not migrate with varying sea level. Moreover, ice and water elements can not overlap, so this approach excludes presence of marine ice and considers only grounded ice (above sea level).

The two components of the surface load are defined in the following way: the ice load is

$$\mathcal{L}_i = \rho^i d^i(\gamma)\chi^i(\gamma)f^i(t), \tag{4.10}$$

where ρ^i is the ice density, $d^i(\gamma) > 0$ is the ice thickness at the coordinates $\gamma = (\theta, \lambda)$, $f^i(t) \geq 0$ is the time history of the ice height, and $\chi^i(\gamma)$ is the mask function, defined as:

$$\chi^i(\gamma) \equiv \begin{cases} 1, & \text{if } \gamma \in i \\ 0, & \text{otherwise.} \end{cases} \tag{4.11}$$

The melt water load is:

$$\mathcal{L}_w = \rho^w d^w(t)\chi^i(\gamma) \ , \tag{4.12}$$

where ρ^w is the density of the water, $\chi^w(\gamma)$ is now defined as:

$$\chi^i(\gamma) \equiv \begin{cases} 1, & \text{if } \gamma \in w \\ 0, & \text{otherwise} \ , \end{cases} \tag{4.13}$$

and finally $d^w(t) > 0$, is the yet unknown time dependent water layer thickness, that we will determined in order to satisfy the constraint of mass conservation. Adding the previous two definitions together, and generalizing to the case of N^i individual ice

elements, we have the total load function:

$$\mathcal{L}(\gamma,t)=\rho^i\sum_{N=1}^{N^i}\left(d^{i,N}(\gamma)\chi^{i,N}(\gamma)f^{i,N}(t)\right)+\rho^w d^w(t)\chi^w(\gamma)\ . \tag{4.14}$$

Mass conservation Principle

We now need to impose the mass conservation principle. It can be demonstrated that it can be stated requiring that the average over the Earth surface of the total load variation must be zero:

$$<\mathcal{L}(\gamma,t)>^e=0\ . \tag{4.15}$$

We can exploit this relationship to compute the unknown variable $d^w(t)$:

$$d^w(t)=-\frac{\rho^i}{\rho^w}\frac{<d^i(\gamma)\chi^i(\gamma)>^e}{<\chi^w(\gamma)>^e}f^i(t), \tag{4.16}$$

where the negative sign indicates that, as expected, an increase in the ice thickness is compensated by a uniform sea-level fall and vice-versa [9]. Then, substituting Eq. (4.16) in the total load function (4.14) we obtain:

$$\mathcal{L}(\gamma,t)=\rho^i\left(d^i(\gamma)\chi^i(\gamma)-\frac{<d^i(\gamma)\chi^i(\gamma)>^e}{<\chi^w(\gamma)>^e}\chi^w(\gamma)\right)f^i(t)\ . \tag{4.17}$$

The form of Eq. (4.16) appears quite complex. We now see how to find an equivalent and lighter form, that later will be used to obtain a more suitable definition for $\mathcal{L}$. After exploiting the term $\chi^i(\gamma)$, the numerator becomes:

$$<d^i(\gamma)\chi^i(\gamma)>^e=\frac{A^i}{A^e}<d^i(\gamma)>^i\ . \tag{4.18}$$

Then, using the definition of the ice load variation:

$$\begin{aligned}m^i(t)&\equiv\int_e\mathcal{L}^i(\gamma,t)dA=\int_e\rho^i d^i(\gamma)\chi^i(\gamma)f^i(t)dA=\rho^i f^i(t)\int_i d^i(\gamma)dA\\&=\rho^i f^i(t)A^i<d^i(\gamma)>^i\end{aligned} \tag{4.19}$$

Combining these two relationships we have:

$$< d^i(\gamma)\chi^i(\gamma) >^e = \frac{m^i(t)}{\rho^i A^i f^i(t)} \ . \tag{4.20}$$

Finally, we note that the denominator of Eq. (4.16), $< \chi^w(\gamma) >^e$ represents just the ratio between the melt water and the Earth's surface, A^w/A^e, so that we can write $d^w(t)$ simply as:

$$d^w(t) = -\frac{m^i(t)}{\rho^w A^w} \ . \tag{4.21}$$

This expression gives the assumed uniform sea-level variation corresponding to the ice mass variation $m_i(t)$, and sometimes this is referred to as "Eustatic Sea-level Variation"[47].

Complex spherical harmonics expansion

The next step is expanding in series of complex spherical harmonics the mass conserving load (4.17), to preserve the expanded definition of $\mathcal{L}$ we introduced in Eq. (4.4). At first, we expand the ice term:

$$d^i(\gamma)\chi(\gamma) = \sum_{nm} d^i_{nm}\mathcal{Y}_{nm}(\gamma), \tag{4.22}$$

with coefficients

$$d^i_{nm} \equiv \frac{1}{4\pi}\int_\gamma \chi^i(\gamma) d^i(\gamma)\mathcal{Y}^*_{nm}(\gamma)d\gamma = \frac{1}{4\pi}\int_i d^i(\gamma)\mathcal{Y}^*_{nm}(\gamma)d\gamma \ , \tag{4.23}$$

and sub-sequentially the melt water term:

$$\chi^w(\gamma) = \sum_{nm} \chi^w_{nm}\mathcal{Y}_{nm}(\gamma), \tag{4.24}$$

with

$$\chi^w_{nm} \equiv \frac{1}{4\pi}\int_\gamma \chi^w(\gamma)\mathcal{Y}^*_{nm}(\gamma)d\gamma = \frac{1}{4\pi}\int_w \mathcal{Y}^*_{nm}(\gamma)d\gamma \ . \tag{4.25}$$

Since for any scalar field, the mean over the whole Earth's surface is $< F >^e = F_{00}$, we can conclude that:

$$\mathcal{L}(\gamma, t) = \rho^i f^i(t) \sum_{nm} d^{iw}_{nm} \mathcal{Y}_{nm}(\gamma) \ , \tag{4.26}$$

where:

$$d^{iw}_{nm} = d^i_{nm} - \left(\frac{d^i_{00}}{\chi^w_{00}} \right) \chi^w_{nm} \ . \tag{4.27}$$

Now we have all the ingredients for computing the SRFs, so the convolution (4.7) becomes:

$$\begin{Bmatrix} \mathcal{U} \\ \mathcal{V}_\theta \\ \mathcal{V}_\lambda \\ \mathcal{G} \end{Bmatrix} (\gamma, t) \equiv \frac{3\rho^i}{\rho^e} \sum_{nm} d^{iw}_{nm} \begin{Bmatrix} c^h_n(t) \\ c^\ell_n(t) \\ c^k_n(t) \end{Bmatrix} \cdot \begin{Bmatrix} 1 \\ \nabla_\theta \\ \nabla_\lambda \\ 1 \end{Bmatrix} \mathcal{Y}_{nm}(\gamma) \tag{4.28}$$

where the time-convolutions are:

$$\begin{Bmatrix} c^h_n \\ c^\ell_n \\ c^k_n \end{Bmatrix} (t) \equiv \frac{1}{2n+1} \int_{-\infty}^{\infty} dt' \begin{Bmatrix} h^L_n \\ \ell^L_n \\ \delta + k^L_n \end{Bmatrix} (t - t') f^i(t') \ . \tag{4.29}$$

4.2 Surface Response Function for axis-symmetric loads

There exist a particular case for the load problem in which special properties of the load geometries allow additional simplifications. It is the case of the axis-symmetric surface loads, i.e., surface loads for which regions i and w are symmetric for rotations around the $z-$ axis [9]. Hypothetically, we can imagine the case of a disc-shaped ice sheet surrounded by an unique ocean (Figure 4.2). If we define a reference frame with the north pole at the centre of the ice disc load, the χ^i and χ^w functions will depend

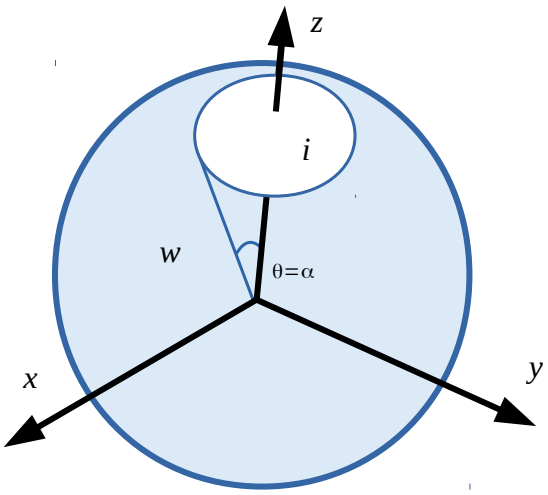

Figure 4.2: An illustration of an axis-symmetric load.

only on colatitude θ:

$$\chi^i(\theta) \equiv \begin{cases} 1, & \text{if } 0 \leq \theta \leq \alpha \\ 0, & \text{if } \alpha \leq \theta \leq \pi \end{cases} \qquad \chi^w(\theta) \equiv \begin{cases} 0, & \text{if } 0 \leq \theta \leq \alpha \\ 1, & \text{if } \alpha \leq \theta \leq \pi \end{cases}, \tag{4.30}$$

where α is the half-amplitude of the ice load. For the moment we make no other assumptions, leaving arbitrary the function $d^i(\theta)$ describing the ice surface, which shall be made specific later on.

The symmetry of the load allows us to compute the d^i_{nm} coefficients of the surface

load:

$$
\begin{aligned}
d^i_{nm} &= \frac{1}{4\pi}\int_\gamma \chi^i(\gamma) d^i(\gamma) \mathcal{Y}^*_{nm}(\gamma) d\gamma \\
&= \frac{1}{4\pi}\int_\gamma \chi^i(\theta) d^i(\theta) \mu_{nm} P_{nm}(\cos\theta) e^{-im\lambda} \sin\theta d\theta d\lambda \\
&= \frac{1}{4\pi}\mu_{nm}\int_0^{2\pi} e^{-im\lambda} d\lambda \times \int_0^\pi \chi^i(\theta) d^i(\theta) P_{nm}(\cos\theta)\sin\theta d\theta \\
&= \frac{1}{4\pi}\mu_{nm} 2\pi\delta_{m0}\int_0^\pi \chi^i(\theta) d^i(\theta) P_{nm}(\cos\theta)\sin\theta d\theta \\
&= \frac{\mu_{nm}\delta_{m0}}{2n+1}\left(\frac{2n+1}{2}\int_0^\pi \chi^i(\theta) d^i(\theta) P_{nm}(\cos\theta)\sin\theta d\theta\right) \\
&= \frac{\mu_{nm}\delta_{m0}}{2n+1} d^i_n
\end{aligned}
\tag{4.31}
$$

where μ_{nm} are normalization constants that comes from the definition of complex spherical harmonics: $\mathcal{Y}_{nm}(\gamma) = \mu_{nm} P_{nm}(\cos\theta) e^{im\lambda}$, and where

$$
d^i_n = \frac{2n+1}{2}\int_0^\pi \chi^i(\theta) d^i(\theta) P_{nm}(\cos\theta)\sin\theta d\theta \ . \tag{4.32}
$$

We remark that in the second line of Eq.(4.31) we have exploited the definition of the complex spherical harmonics. In the same way we can gain a similar definition for χ^w_{nm}:

$$
\chi^w_{nm} = \frac{\mu_{nm}\delta_{m0}}{2n+1}\chi^w_n \quad \text{where} \quad \chi^w_n = \frac{2n+1}{2}\int_0^\pi \chi^w(\theta) P_{nm}(\cos\theta)\sin\theta d\theta \ . \tag{4.33}
$$

Putting these two results together in Eq. (4.27), we have:

$$
d^{iw}_{nm} = \frac{\mu_{nm}\delta_{m0}}{2n+1}\left(d^i_n - \frac{d^i_0}{\chi^w_0}\chi^w_n\right) = \frac{\mu_{nm}\delta_{m0}}{2n+1} d^{iw}_n \ , \tag{4.34}
$$

where:

$$
d^{iw}_n = d^i_n - \frac{d^i_0}{\chi^w_0}\chi^w_n \ . \tag{4.35}
$$

Substituting this expression into (4.28) it is possible to arrive to a final solution.

The SRF for the vertical displacement leads to:

$$\begin{aligned}
\mathcal{U}(\gamma,t) &\equiv \frac{3\rho^i}{\rho^e}\sum_{nm} d_{nm}^{iw} c_n^h(t)\mathcal{Y}(\gamma) \\
&= \frac{3\rho^i}{\rho^e}\sum_{nm} \frac{\mu_{nm}\delta_{m0}}{2n+1} d_n^{iw} c_n^h(t)\mu_{nm}P_{nm}(\cos\theta)e^{im\lambda} \\
&= \frac{3\rho^i}{\rho^e}\sum_{nm} \frac{\mu_{n0}}{2n+1} d_n^{iw} c_n^h(t)\mu_{n0}P_{n0}(\cos\theta) \\
&\Rightarrow \mathcal{U}(\theta,t) = \frac{3\rho^i}{\rho^e}\sum_{n=0}^{\infty} d_n^{iw} c_n^h(t)P_n(\cos\theta) \ ,
\end{aligned} \tag{4.36}$$

and the SRF for the geoid height can be obtained in the same way, obtaining:

$$\mathcal{G}(\theta,t) = \frac{3\rho^i}{\rho^e}\sum_{n=0}^{\infty} d_n^{iw} c_n^k(t)P_n(\cos\theta) \ . \tag{4.37}$$

For the longitudinal displacement term, we have:

$$\mathcal{V}_\theta(\theta,t) = \frac{3\rho^i}{\rho^e}\sum_{n=0}^{\infty} d_n^{iw} c_n^\ell(t)\frac{\partial P_n(\cos\theta)}{\partial\theta} \tag{4.38}$$

whereas, due to the symmetry of the load, we obtain:

$$\mathcal{V}_\lambda = 0 \ . \tag{4.39}$$

4.3 Surface Response Function for disc loads

In this Section we will consider the case of a disc-shaped load (Figure 4.3), in which $d^i = const$ over the whole subset i. As a consequence, from the integral 4.32 we have:

$$\begin{aligned}
d_n^i &= \frac{2n+1}{2}\int_0^\pi \chi^i(\theta)d^i(\theta)P_n(\cos\theta)\sin\theta d\theta \\
&= \frac{2n+1}{2}d^i\int_{\cos\alpha}^1 P_n(x)dx \\
&= \frac{2n+1}{2}d^i\int_{\cos\alpha}^1 \frac{P'_{n+1}(x)-P'_{n-1}(x)}{2n+1}dx \ ,
\end{aligned} \tag{4.40}$$

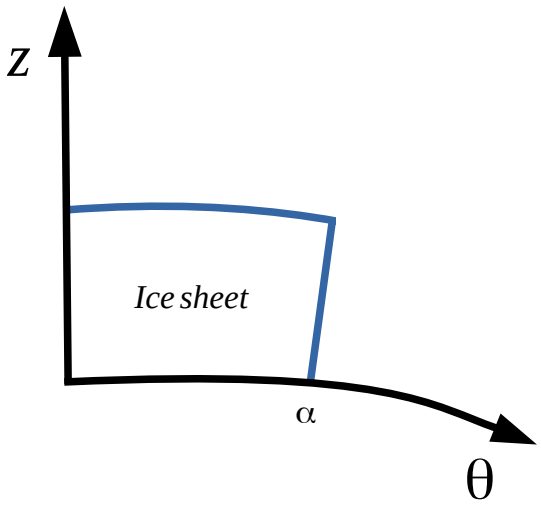

Figure 4.3: Disc-shaped load of half-amplitude α.

where in the last line we have exploited the "shifted derivative property" of Legendre polynomials. Given that $P_n(1) = 1$, we obtain:

$$d_n^i = \frac{d^i}{2}(P_{n-1}(\cos\alpha) - P_{n+1}(\cos\alpha)) \ , \tag{4.41}$$

and similar considerations lead to:

$$\chi_n^w = \frac{1}{2}(P_{n-1}(\cos\alpha) - P_{n+1}(\cos\alpha)) \ . \tag{4.42}$$

With these last definitions, the coefficients d_n^{iw} become:

$$\begin{aligned} d_n^{iw} &= \left(d_n^i - \frac{d_0^i}{\chi_0^w}\chi_n^w\right) \\ &= \frac{d^i}{2}(P_{n-1} - P_{n+1}) + \frac{d^i/2}{1/2}\frac{1-\cos\alpha}{1+\cos\alpha}\frac{1}{2}(P_{n-1} - P_{n+1}) \\ &= \frac{d^i}{2}(P_{n-1} - P_{n+1})\left(1 + \frac{1-\cos\alpha}{1+\cos\alpha}\right) \\ &= d^i\frac{P_{n-1} - P_{n+1}}{1-\cos\alpha} \quad l \geq 1 \end{aligned} \tag{4.43}$$

where here, for the sake of simplicity, we have abbreviated $P_n(\cos\alpha)$ by P_n.

Finally, the SRF of the disc load are:

$$\mathcal{U}(\theta,t) = \frac{3\rho^i}{\rho^e}\sum_{n=0}^{\infty} d_n^{iw} c_n^h(t) P_n(\cos\theta) \tag{4.44}$$

$$\mathcal{G}(\theta,t) = \frac{3\rho^i}{\rho^e}\sum_{n=0}^{\infty} d_n^{iw} c_n^k(t) P_n(\cos\theta) \tag{4.45}$$

$$\mathcal{V}_\theta(\theta,t) = \frac{3\rho^i}{\rho^e}\sum_{n=0}^{\infty} d_n^{iw} c_n^\ell(t) \frac{\partial P_n(\cos\theta)}{\partial\theta} \ , \tag{4.46}$$

with

$$d_n^{iw} = d^i \frac{P_{n-1}(\cos\alpha) - P_{n+1}(\cos\alpha)}{1-\cos\alpha} \quad l \geq 1 \ . \tag{4.47}$$

The disc-shaped load is precisely the load model that I will use in the following simulations. In the next chapter I will show the results of my work: after computing the LLNs for various Earth models in the previous chapter, and after showing, in this chapter, how to obtain the expected deformation caused by a plausible load, I will evaluate the contribution of transient rheology to surface deformation.

Chapter 5

Results of the simulations

In this chapter I will discuss the results obtained by the simulations I performed with `ALMA`. I used a `FORTRAN 90` code for computing the convolution in Eqs. (4.44), (4.46), (4.45) and then I used `MATLAB` to produce the plots that will be shown in this chapter. The first experiment has the simplest set up: an inverted Heaviside-step function (see Figure 5.1) as time history describing the melting of a disc-shaped ice-sheet applied on a 3-layer Earth.

The second experiment considers a more realistic time history, representing a deglaciation that occurred between 21 *kyr* and 6 *kyr* ago, in which the ice melts following a gradual steps decrease. The Earth model used is the same as in the first experiment.

The third experiment consisted in two simulations performed considering a 2-layer mantle, respectively with viscosity trends that follow the ideas of Peltier [20] and Lambeck [48] (see Section 1.5). The time history used is the one of the previous experiment.

In the fourth and last experiment I performed a simulation in which I consider present-day ice melting: the ice load is smaller, in order to reproduce glaciers and ice caps, the Earth model accounts for a thinner lithosphere and the ice history has a ramp-shape.

5.1 Experiment 1: Heaviside time-history, 3-layer Earth

In the first simulation, I considered the easiest time evolution for the ice load: the step function. In this experiment the description of the melting of the ice is extremely

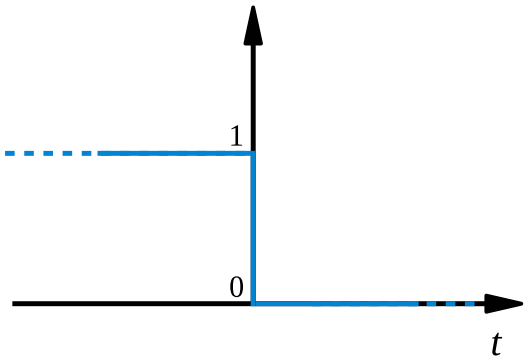

Figure 5.1: Step Function representing the evolution of the ice sheet. In this case, extremely simplified, the ice disappears suddenly at $t = 0$.

simplified: the disc-shaped ice-sheet, unperturbed since $t = -\infty$, suddenly disappears at $t = 0\ yr$ (see Figure 5.1). The half-amplitude of the ice-sheet is set to 10°, to simulate the displacement magnitudes expected from the melting of an ice-sheet such as the Laurentide. This load function is then convoluted following Eqs. (4.44), (4.45) and (4.46) with the LLNS obtained for a 3-layer Earth model ($n_{max} = 10000$) considering both Maxwell and Andrade rheologies in the mantle. (see parameters in Table 5.1). This

Radius $m \cdot 10^3$	**Density** $kg/m^3 \cdot 10^3$	**Rigidity** $Pa \cdot 10^{11}$	**Viscosity** $Pa \cdot s$	**Rheology**
6371	3.300	0.28	10^{21}	E
6271	4.518	1.45	10^{21}	M/A
3480	10.977	0	0	F

Table 5.1: Parameters for GS00, a 3−layered Earth model. In the last column the "E", "M", F", "A" indicate the rheological behaviour attribute the parameters (Elastic, Maxwell, Fluid and Andrade).

first approach does not aim to describe in detail a realistic response of the Earth, but it is a first step for gaining confidence with the main characteristics of the responses of the two Earth models considered. In Figure 5.2 a schematic representation of the problem is shown.

At first I have computed the expected **vertical displacement** as a function of the angular distance θ, from $t = 0$ until $t = 10\ kyr$, with a temporal step of 0.5 kyr. In Figure 5.3 are reported some of the steps of its time evolution, for times $t = 0,\ 0.5,\ 5$

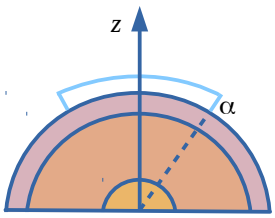

Figure 5.2: Schematic representation of the first simulation. α is the angular extension of the disc-shaped ice load.

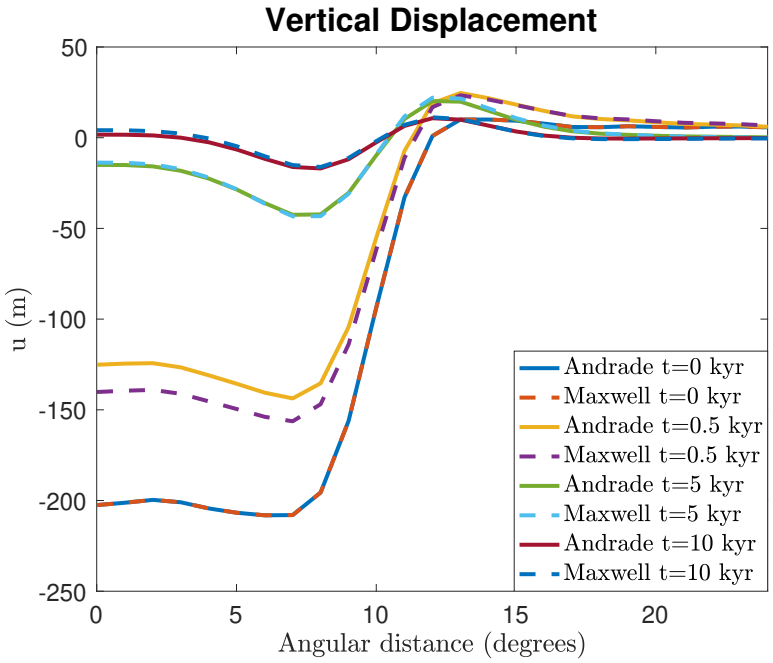

Figure 5.3: **Vertical Displacement**: in this plot the vertical displacement is shown as a function of the angular distance θ from the centre of the disc-shaped ice sheet. In the figure, four time steps are considered. $t = 0$, $t = 0.5$, $t = 5$ and $t = 10$ kyr. For the ease of visualization, the dashed curves refer to the displacement computed with a Maxwell rheology in the mantle, while the solid one are the one computed considering an Andrade rheology.

and 10 kyr. At $t = 0$ the profile reflects perfectly the ice load: at small angular distances we have the maximum depression, then, at around 10°, corresponding to the ice-sheet boundary, the displacements decrease rapidly until values close to zero; moreover, at time $t = 0$ the two responses (the one computed considering a Maxwell's rheology and the one considering an Andrade's rheology in the mantle) coincide. This is because a state of *isostatic equilibrium* was reached before the instantaneous deglaciation. Then, in the following time step, at $t = 0.5$ kyr, we see that, due to the absence of the load, the Earth's surface starts uplifting. As it will be shown better later, I found that the maximum difference between the expected displacement computed with the two models is reached at this time step. Indeed, in the following time steps, for $t = 5,\ 10$ kyr the computed displacement almost superimpose. Of course by choosing a smaller time interval, it would be possible to locate this event with a better precision, but for our purposes this is sufficient. One of the most remarkable considerations is that after a time $t = 10$ kyr the Earth has almost totally recovered from the deformation caused by the ice-load, or at least, the residual deformation is ten times smaller than the initial response.

Figure 5.4 shows the **horizontal displacement**. Even in this case, for $t = 0$ the responses for the two rheologies are the same, and for $t = 0.5$ kyr we have the maximum difference between Maxwell and Andrade. Then, for subsequent times, this difference tends to disappear and, at the same time, the deformations decrease to zero. The shape of the horizontal displacement has a particular trend with a minimum fixed at 10° and the two maximum at its sides. The symmetry imposes that the displacement must vanish for angular distances $\theta = 0°$ and $\theta = 180°$.

Considering the **geoid displacement**, we can see their trends in Figure 5.5. They reflect in a smoother way the vertical deformations. Between the cases analysed until now, this is the one whose response *recover* the most from the original deformation: for $t = 10$ kyr the plot is almost flat.

To better define the displacement variation I have also computed the **displacement rates** (or velocities). To estimate the velocity with `MATLAB` at a particular time t_{i+1} and at a particular angular distance, I simply computed the difference between the value of the displacement at t_{i+2} and at t_i, and then I divided by the time interval. That is why, in all the plots that show the rates, I will refer not to a single time instant, but to the relative time interval.

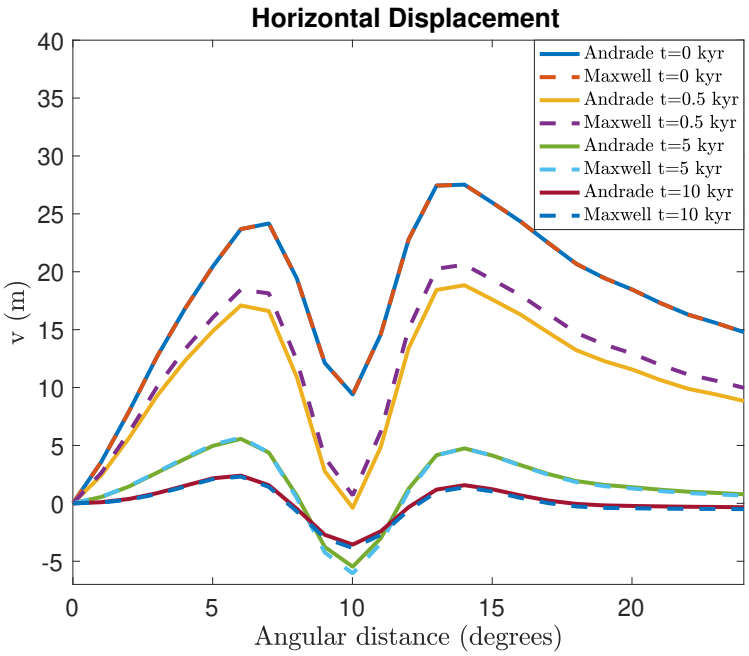

Figure 5.4: **Horizontal Displacement**: the displacement is displayed as a function of the angular distance θ from the centre of the ice-load. The dotted curves refer to an Earth model with a Maxwell rheology in the mantle, the solid ones to Andrade. The four group of curves refers to times $t = 0,\ t = 0.5,\ t = 5$ and $t = 10\ kyr$.

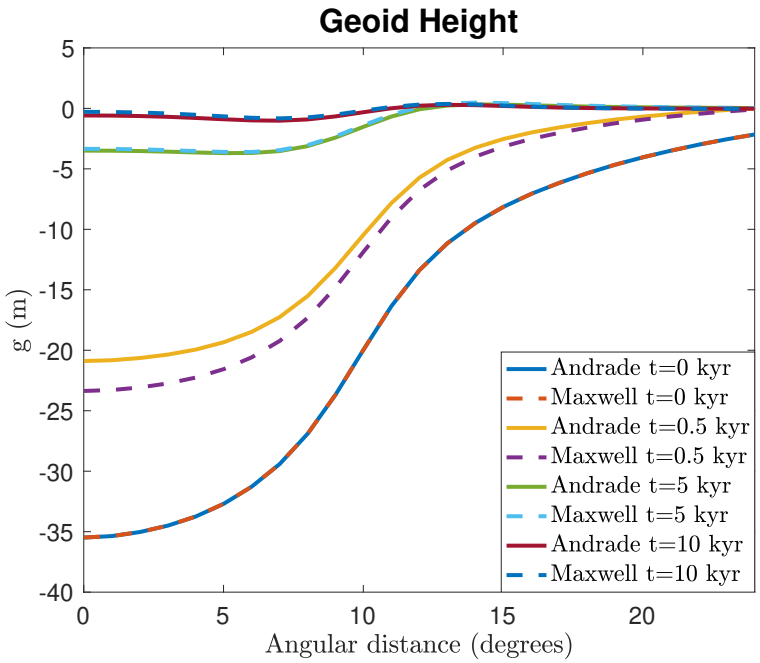

Figure 5.5: **Geoid Height variations**: variation of height of the geoid as a function of angular distance. Here are reported four time steps, $t = 0$, $t = 0.5$, $t = 5$ and $t = 10$ kyr. Their shape is qualitatively similar to the one of the vertical displacement, but the amplitude differs.

During my experiments I found that the rates reach their maximum values at the beginning, in the period included between $t = 0\ kyr$ and $t = 1kyr$, then they linearly decrease until they reach the minimum at the end of the simulation, for the time $t = 9 \div 10\ kyr$. In Figures 5.6 and 5.7 we can see these two cases. The rates are shown as a function of the angular distance. It is interesting to notice that in the ideal case that we are considering (a huge amount of ice that disappears instantaneously), the initial response in terms of vertical displacement reaches a considerable value (10 cm/yr). Another relevant consideration is the fact that Andrade's response is faster than the Maxwell one: this could be inferred even by just observing the first three Figures (5.3 - 5.5): Andrade's displacements are always closer to the following time step, and this fact finds a confirmation in the plot of the maximum rates (Figure 5.6), where Andrade's velocities are always higher than Maxwell's ones. Nevertheless, during the simulation,

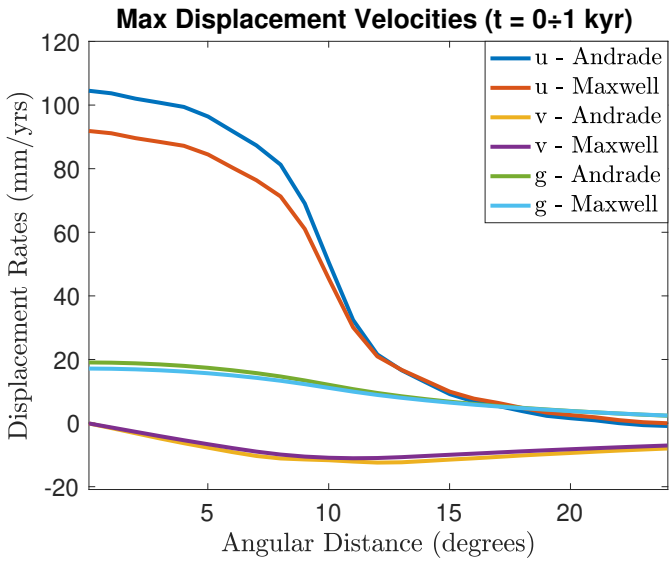

Figure 5.6: **Maximum displacement velocities**: in this graph are reported, as a function of the angular distance, the maximum velocities of vertical (u) and horizontal (v) displacement, as well as the variation in geoid height g. This maximum occurs in a time between 0 and 1 kyr; during the whole duration of the simulation these velocities progressively decrease.

this difference tends to vanish and in the final step (Figure 5.7) the two models have almost the same velocities. This is particularly true in the case of the geoid height (Figure 5.7), were the two trends are indistinguishable.

It is interesting to notice that, as regard the vertical velocity, the initial trend has only positive values (Figure 5.6), while in the last time step (Figure 5.7), at an angular distance of $\theta > 10°$, the velocity changes sign, and becomes negative. Observing Figure 5.3, it is clear that this is due the the adjustment of the forebulge: this sort of lateral bulge feels the effect of the surrounding uplift, but contrary to the depressed region, during the ice accumulation, it lifted up over $z = 0$. For this reason, it is possible to see in the simulation that after more or less $t = 5\ kyr$ from the disappearance of the ice load, that region is characterized by a negative velocities, that means a drop in terms of displacement.

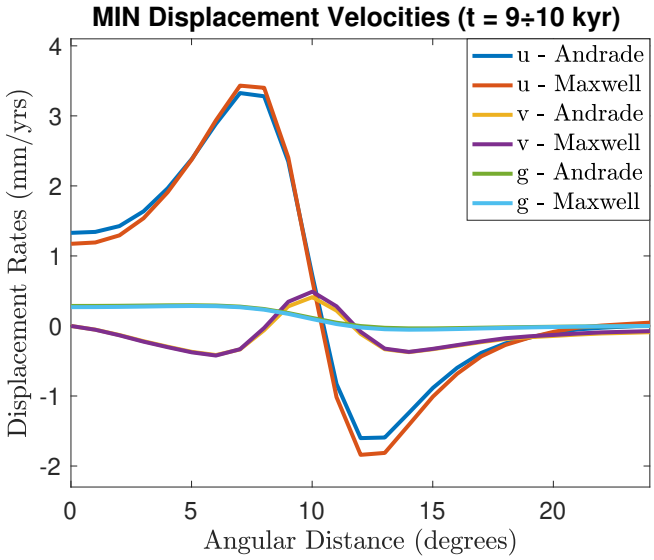

Figure 5.7: **Minimum displacement velocities**: in this graph are reported, as a function of the angular distance, the minimum velocities of vertical (u) and horizontal (v) displacement, as well as the variation in geoid height g, which occurs for $t = 9 \div 10\ kyr$. Notice that with respect Figure 5.6 the y axis has been re-scaled.

To conclude this first experiment, in Figures 5.8 and 5.9 I show the maximum and minimum absolute value differences between the expected displacement computed by the two models. As previously mentioned, the maximum differences appear at the beginning of the simulation, for $t = 0.5\ kyr$ (Figure 5.8), while the minimum appears at the end (Figure 5.9). In both cases, the larger differences occur in the estimate of the vertical displacement, that reaches 15 m at $t \simeq 500\ yr$. Then these differences tend to decrease, reaching their minimum values for $t = 10\ kyr$.

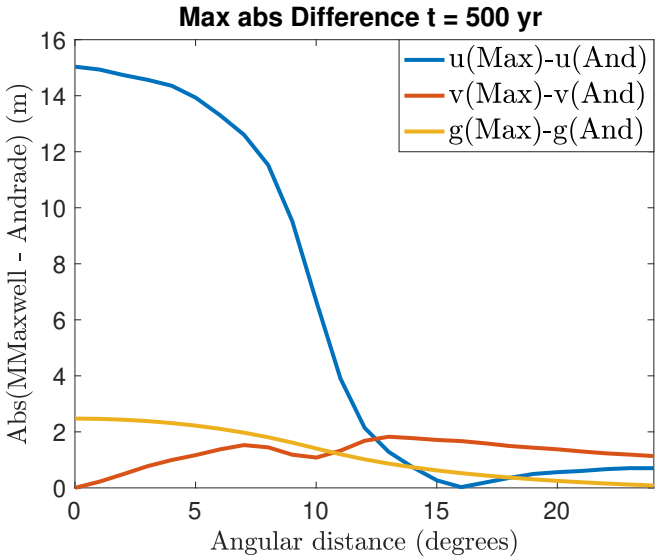

Figure 5.8: **Maximum absolute difference** between vertical, horizontal and geoid displacement computed with Maxwell and Andrade's model. This occurs at the start of the simulation, for $t = 500\ yr$.

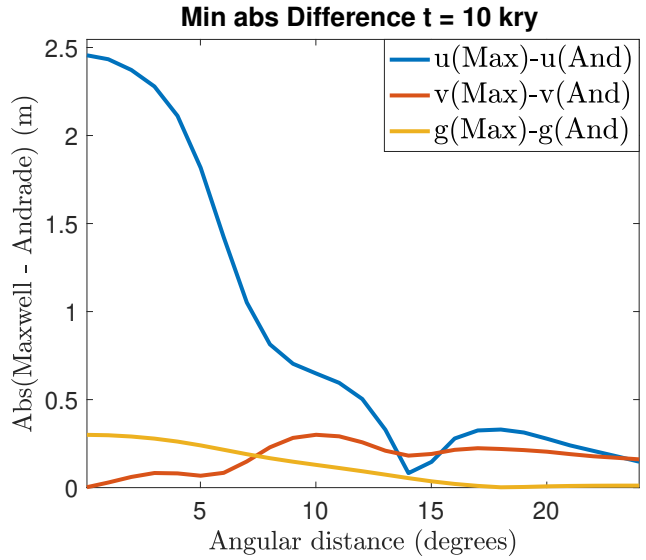

Figure 5.9: **Minimum absolute difference** between vertical, horizontal and geoid displacement computed with Maxwell and Andrade's model. This occurs at the end of the simulation, for $t = 10\ kyr$. Note that the y scale is different with respect to the previous plot.

5.2 Experiment 2: realistic step-function time-history, 3-layer Earth

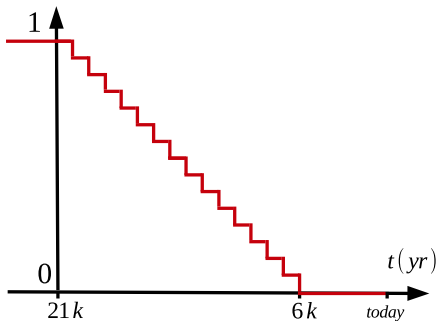

Figure 5.10: Sketch of the second time history used. This time the description of the melting is gradual, and thus more realistic. From its maximum at 21 *kyr*, the ice height decreases in a piecewise manner in time steps of 1 *kyr* until it reaches zero 6 *kyr* ago, when the full deglaciation occurs.

In this second experiment I considered a more realistic representation of the evolution of the ice load, whose plot is described in Figure 5.10.

With this spirit, next simulations aim at reproducing the expected deformations (and relative rates) due to the melting of a continental ice-sheet like, for example, the Laurentide. This ice-sheet, during the Late Pleistocene, extended over the western interior Plains and Great Lakes region in the central region of North America (Figure 5.11).

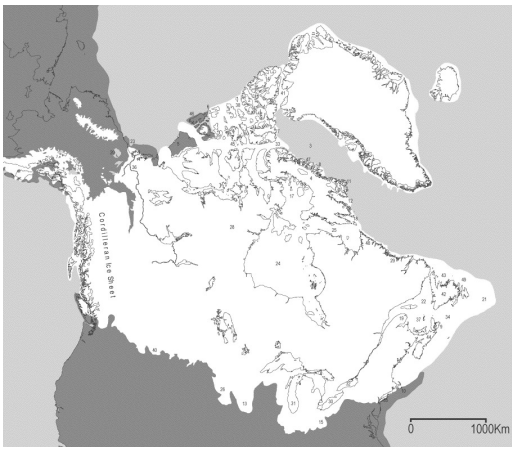

Figure 5.11: **Laurentide Ice sheet at Last Glacial Maximum**: figure from [49].

This area generally encompasses the northwestern interior Plains of North America, extending from the Rocky Mountains in the west to the western Great Lakes and Hudson Bay in the east [50]. The Laurentide underwent a fast deglaciation that acted in different times over different regions. Our simulation is extremely rough and does not aim to retrace accurately the Laurentide deglaciation, since our ice model is just a disc-shaped load that gradually loses height but that does not shrink. Indeed, we remark here that we are not interested in computing the most reliable values of displacement that we expect to observe from satellite data, but our purpose is instead understanding the main differences that a rheological model accounting for a transient produce with respect to models that do not account for transient effects. I used the same Earth models of the

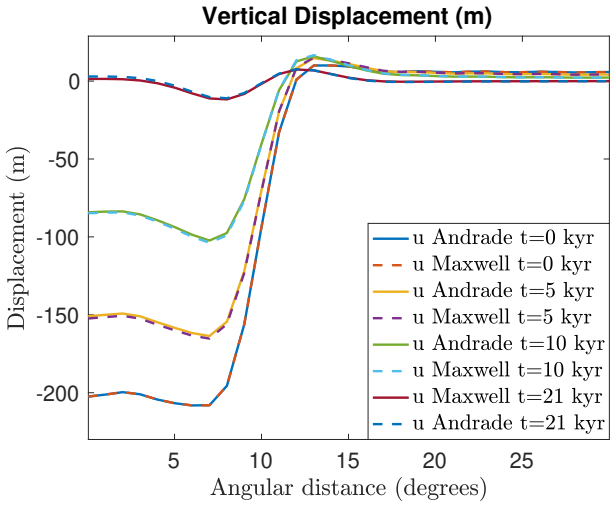

Figure 5.12: **Vertical displacement**: the displacement is plotted as function of the angular distance from the center of the ice-load. Four temporal steps are reported: $t = 0,\ 5,\ 10$ and $21\ kyr$. The shape of the profile is quite similar to the previous one of experiment 1.

previous experiment, whose parameters are reported in Table 5.1, and following the same methods I computed the expected displacement.

Observing the plots concerning the **surface dispacement** and the **geoid height variation** (Figures 5.12, 5.13, 5.14) at first sight no large differences appear with respect to Figures 5.3, 5.4, 5.5.

However, a more careful analysis reveals interesting features. First of all, the time range in which the Earth's surface $forgets$ the deformation is different: the simulation

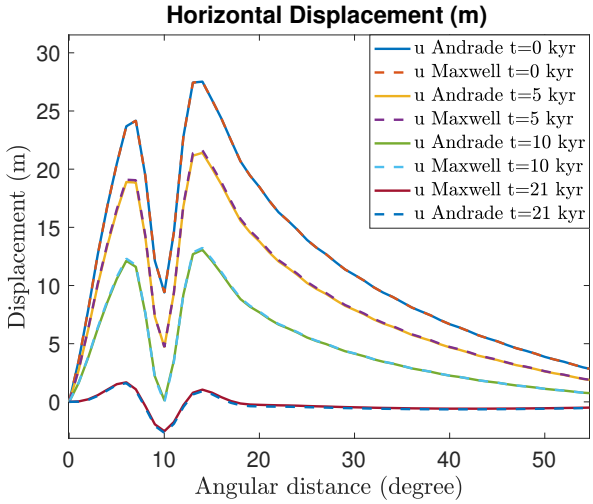

Figure 5.13: **Horizontal displacement**: the horizontal displacement is plotted as function of the angular distance from the center of the ice-load. Four temporal steps are reported: $t = 0,\ 5,\ 10$ and 21 kyr. Even in this case we can recognize the typical trend of the horizontal displacement, with the minimum nearby the boundary of the ice sheet and the maximums at its sides.

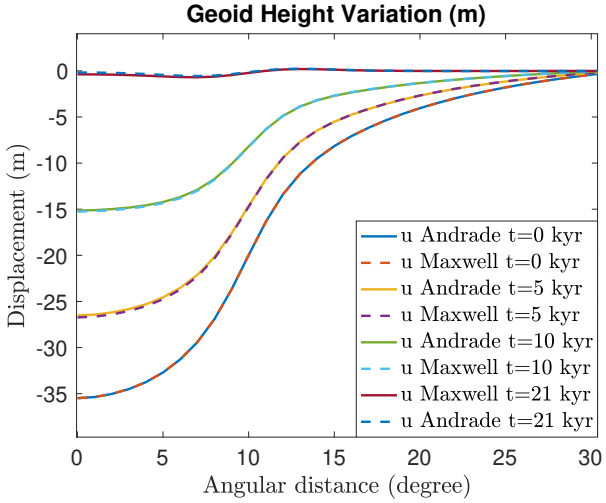

Figure 5.14: **Geoid height variations**: the geoid height is plotted as a function of the angular distance from the center of the ice-load. Four temporal step are reported: $t = 0,\ 5,\ 10,\ 21\ kyr$.

is continued to 21 kyr. This makes sense considering that the ice does not disappear instantaneously like it did before, but melts gradually and it disappears 6 kyr before present. Then, another characteristic feature is that the deformation computed considering Andrade's rheology for the mantle differs much less than the one computed with a Maxwellian mantle with respect to the first experiment. Indeed, the two curves, the dashed one and the solid one, are always very close to each other.

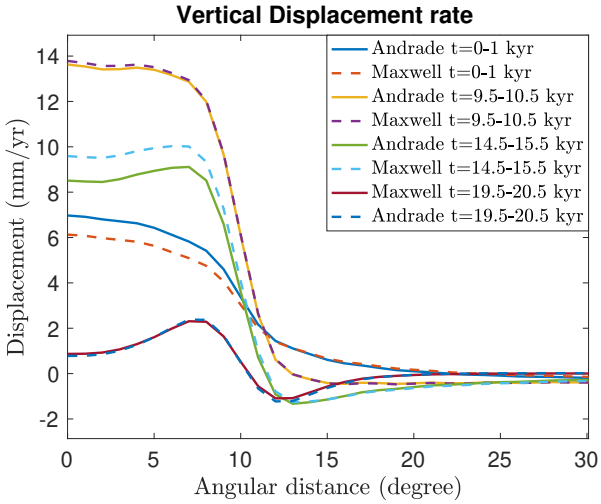

Figure 5.15: **Time evolution of the velocity profile of the vertical displacement**: in the first 10 kyr velocities under the melting ice-sheet increase from initial value of $6 \div 7$ mm/yr to 14 mm/yr. Then the profile remains almost the same for the following 4.5 kyr. In the time step time included between $14.5 \div 15.5$ kyr a drop occurs, and then the velocities decrease almost linearly until the end of the simulation.

Something that may not emerge from the previous plots is the evolution of the **displacement rates**, that is instead well described in the following Figures 5.15, 5.16, 5.17. While in the previous experiment the velocity profile, after reaching instantaneously its maximum at the first time steps, followed a linear reduction, now the tendency is different.

Here the maximum velocities are reached not in the first time step, but around $9 \div 10$ kyr from the start of the simulations. Then, for a time of ~ 5 kyr, the profile remains almost constant. Subsequentially, in the time step corresponding to $14.5 \div 15.5$ kyr, the velocities undergo to a sudden decrease. This temporal instant coincides with the one in which the ice-sheet vanishes totally. After this drop, the velocities tend to decrease.

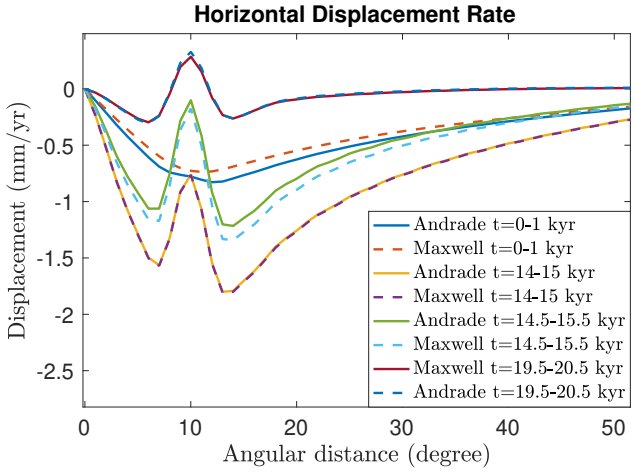

Figure 5.16: **Time evolution of the velocity profile of the horizontal displacement**: the main temporal features are the same of the vertical displacement (the growth until $14.5 \div 15.5$ kyr and then the decrease). This time I plotted the instant in which the drop happens: the yellow and violet line refers to $t = 14 \div 15$ kyr, while the green and light blue one the following time step $t = 14.5 \div 15.5$ kyr.

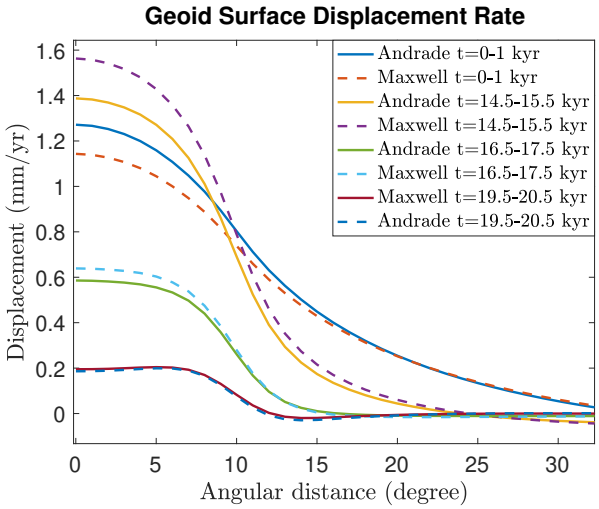

Figure 5.17: **Time evolution of the velocity profile of geoid height variation**: this profile is really similar to the one of the vertical displacement rate: from values between 1.2 mm/yr and 1.3 mm/yr, at $t = 14 \div 15$ kyr the velocities reach their maximum and then, in the following time step, they decrease suddenly. Here are reported four different time steps: $t = 0 \div 1$ kyr, $t = 14 \div 14$ kyr, $t = 16.5 \div 17.5$ kyr and $t = 19.5 \div 20.5$ kyr.

5.3 Experiment 3: 2-layer Mantle

The disc-shaped ice-sheet that we have considered in our simulation has a half-amplitude of $\alpha = 10°$, that correspond to a diameter on the Earth's surface of $\simeq 2000\ km$. Thus, the lateral extent of this ice-sheet is so large that the induced deformation is likely to be sensitive to Earth's deep layers. Therefore, ignoring a realistic layering of the mantle would produce inaccurate results. For this reason in the following experiment, a two-layer mantle model will be used. We opted for the model BJ97 [40]. Recalling the discussion of Section 1.5 we will consider both a "Peltier" layering, in which the viscosity of the upper mantle ($10^{21} Pa \cdot s$) differs by a factor 2 from the viscosity of the lower mantle ($2 \cdot 10^{21} Pa \cdot s$) [20], both a "Lambeck" layering, in which the viscosities differ of a factor 10 [19]. Here I remark that, for the upper mantle, I do not use exactly the parameters that Lambeck has indicated in his work as the better estimate ($0.5 \cdot 10^{21}$); I made this choice to build two models in which only the viscosity of the lower mantle varies, with the aim of focusing on the role of this unique phenomena. Therefore, taking advantage of the large value interval in which Lambeck has defined the viscosity of the upper mantle, I considered the higher value, $7.5 \cdot 10^{20} \simeq 10^{21}\ Pa \cdot s$. In Figure 5.18, for the sake of clarity, we can see a schematic representation of the present simulation.

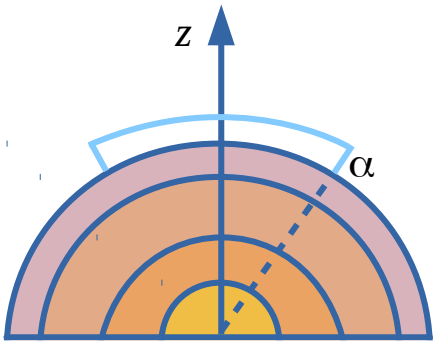

Figure 5.18: Schematic representation of the third simulation. α is the angular extension of the disc-shaped ice load. The mantle is divided into an upper and a lower layer.

We note that the presence of a two-layer mantle offers us the chance of considering a transient rheology in the upper or in the lower mantle, separately. We have a total of 6 possibilities:

- **Peltier's Maxwell mantle - Max-2M(P)**: In this model, the two mantles are

characterized by a Maxwell rheology, and the viscosities are $10^{21} Pa \cdot s$ for the upper one and $2 \cdot 10^{21} Pa \cdot s$ for the lower mantle;

- **Peltier's mantle with Andrade in the upper mantle - And-SUP(P)**: In the upper mantle, an Andrade's rheology is present and the viscosity is set to $10^{21} Pa \cdot s$, while the lower mantle follows a Maxwell's rheology with a viscosity value of $2 \cdot 10^{21} Pa \cdot s$;

- **Peltier's mantle with Andrade in the lower mantle - And-INF(P)**: this time the Andrade rheology is in the lower mantle, whose viscosity is set to $2 \cdot 10^{21} Pa \cdot s$, while in the upper mantle we have a Maxwell rheology with a viscosity of $10^{21} Pa \cdot s$;

- **Lambeck's Maxwell mantle - Max-2M(L)**: the two mantles follow a Maxwell rheology. The viscosities are $10^{21} Pa \cdot s$ for the upper one and $10^{22} Pa \cdot s$ for the lower;

- **Lambeck's mantle with Andrade in the upper mantle - And-SUP(L)**: The upper mantle obey Andrade rheology and its viscosity is set to $10^{21} Pa \cdot s$, the lower mantle follows a Maxwell rheology and its viscosity is set to $10^{22} Pa \cdot s$;

- **Lambeck's mantle with Andrade in the lower mantle - And-INF(L)**: Andrade rheology is in the lower mantle, with a viscosity set to $10^{22} Pa \cdot s$, while in the upper mantle there is a Maxwell rheology with a viscosity of $10^{21} Pa \cdot s$;

In Table 5.2 the values of all the parameters of BJ97 are summarized. For all models I computed with `ALMA` the corresponding LLNs up to $n = 10000$. This third experiment is, among the ones performed until now, the more realistic, and therefore in this section we will address the main aim of this thesis, that is understanding until how many (kilo)years the effects of a transient behaviour in the Earth are observable.

Displacements

The following outputs were obtained in the same way of the previous simulations. In this Section I will report the output concerning the expected deformations as a function of the angular distance θ for different times. Differently from the previous experiment,

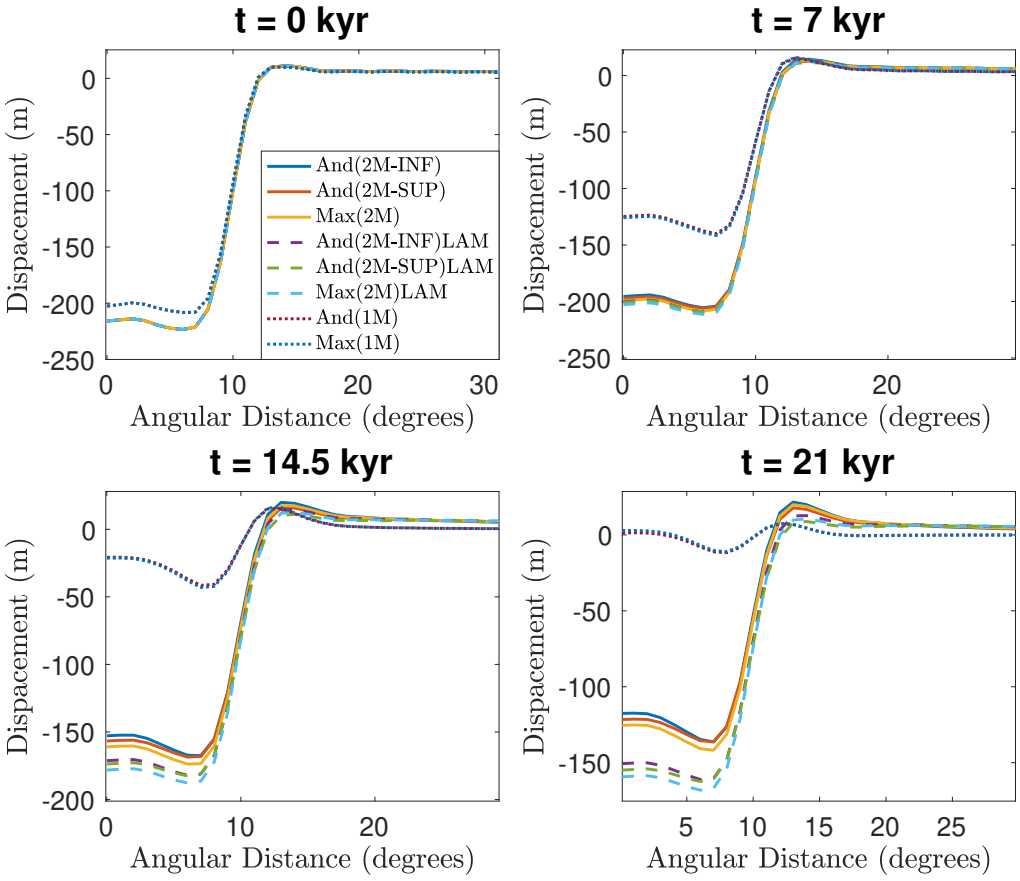

Figure 5.19: **Vertical Displacement**: in the four plots the vertical displacement is reported for different times $t = 0,\ 7,\ 14.5$ and 21 kyr. At $t = 0$ kyr we can distinguish the different initial deformation estimated from this and the previous experiment. At $t = 7$ kyr and $t = 14.5$ kyr the surface beneath the load is uplifting; at the end of the simulation we can distinguish well the difference between the displacement computed using models that considered Peltier's approach and Lambeck's one.

Radius $m \cdot 10^3$	**Density** $kg/m^3 \cdot 10^3$	**Rigidity (Pa)** $Pa \cdot 10^{11}$	**Viscosity** $10^{21} Pa \cdot s$	**Rheology**
6371	2.771	0.315	∞	E
6271	4.120	0.954	1	M/A
5701	4.508	1.990	2 (P) or 10(L)	M/A
3480	10.925	0	0	F

Table 5.2: Parameters for Bills and James (1997), a 4−layer Earth model proposed in [40]. In the last column "E", "M", "F", "A" indicate to which kind of rheological behaviour attribute the parameters (Elastic, Maxwell, Fluid, Andrade). The value of viscosity of the lower mantle can change whether we are considering Lambeck(L) or Peltier (P) approaches.

the number of considered model obliged me to choose a different way of representing data: in this case, each window represents a single temporal step.

Concerning the **vertical displacement** (Figure 5.19), we can see that the profiles have the general features of the previous simulations: the surface beneath the ice load is gradually subject to an uplift, while at angular distances $\theta > 20°$ the deformation is almost negligible. In all the figures concerning the displacements and the velocities, in addition to the six models listed above, I reported also the output of the previous experiment, (dashed curves) in order to have a basis for comparison.

The first thing that stands out is that, for $t = 0$, in the region between $0° \leq \theta \leq 10°$, there is a difference in the depth of the surface below the ice sheet computed from this experiment and the previous one. The models considered before lies about 20 m above the new ones. This has nothing to do with the viscosities, rather it is due to the different densities chosen for the layers, that entail a different depth for the isostatic compensation.

The second thing that one can notice, is that these new models with a layered mantle and greater viscosities predicts a much slower deformation than the ones with a unique mantle. At the end of the simulation, the region between $0° \leq \theta \leq 10°$ is still depressed, while in the previous experiment we saw that after a time of 21 kyr the residual deformation was a factor 10 lower than the original one. Then, we can say that the differences between the new models increase with time, and after more or less 15 kyr, we can notice that the profiles split into two groups: the one that reaches the maximum height is the group of the simulations done considering a *Peltier* viscosities layering, while *Lambeck's* ones lies about thirty meters below. An intuitive explanation for this fact is that the

Lambeck model, thanks to a viscosity of the lower mantle set to $10^{22}\ Pa \cdot s$, results less prone to deformation (hence, has a longer relaxation time).

Another remarkable feature of these plots, especially visible in the one for $t = 21\ kyr$, is that inside each of the two groups, the trend regarding the three possibilities for the mantle behaviour are arranged in the same order: at the top we have the model with an Andrade transient component in the lower mantle (and Maxwell in the upper one), then the one with Andrade in the upper mantle, and the last is always the one with Maxwell in the two mantles. This is in line with the previous results: we saw that, indeed, Andrade's transient rheology produced faster deformation than the Maxwell one. In this case we have a composition of Andrade and Maxwell rheologies in the mantle, so it was foreseeable that the case of an upper and lower mantle with a Maxwell behaviour produced the slowest deformation. Nevertheless, is quite interesting to see that considering a transient behaviour in the lower mantle generates a faster deformation than a transient in the upper mantle. In the next section regarding rates of displacement we will better characterize this behaviour.

The **horizontal displacement** (Figure 5.20) have the typical shape with two maxima around 6° and 14°, and the minimum in 10°. The symmetry of the problem imposes a null horizontal displacement in 0° and 180°. Even here we can notice an initial difference between the computed displacement of the new experiment and the previous one. However, since the entity of the horizontal deformations are of the order of few meters, these differences are much smaller than those of the vertical deformations. Unlike the previous case, here the outputs stand, for the whole duration of the simulation, almost in the same values interval and it is more complicated to group the results. The general trend is a reduction of the displacement toward the zero for increasing time, but as happened before, in 21 kyr the deformation does not disappear at all. This reduction affects primarily the peripheral areas, while the zone around the ice-sheet boundary maintains its shape, with the two maximua and the minimum at $\theta = 10°$.

Regarding the difference between Peltier's and Lambeck's models, we can see that in Peltier's case, the trends seems a little delayed with respect Lambeck's one, which decreases faster. However, while for angular distances $> 15°$ Peltier's horizontal displacement decreases linearly, in Lambeck's case, especially at the end of the simulation, a lateral swelling starts developing.

In the **geoid height variation** plot (Figure 5.21), we can see that in general what

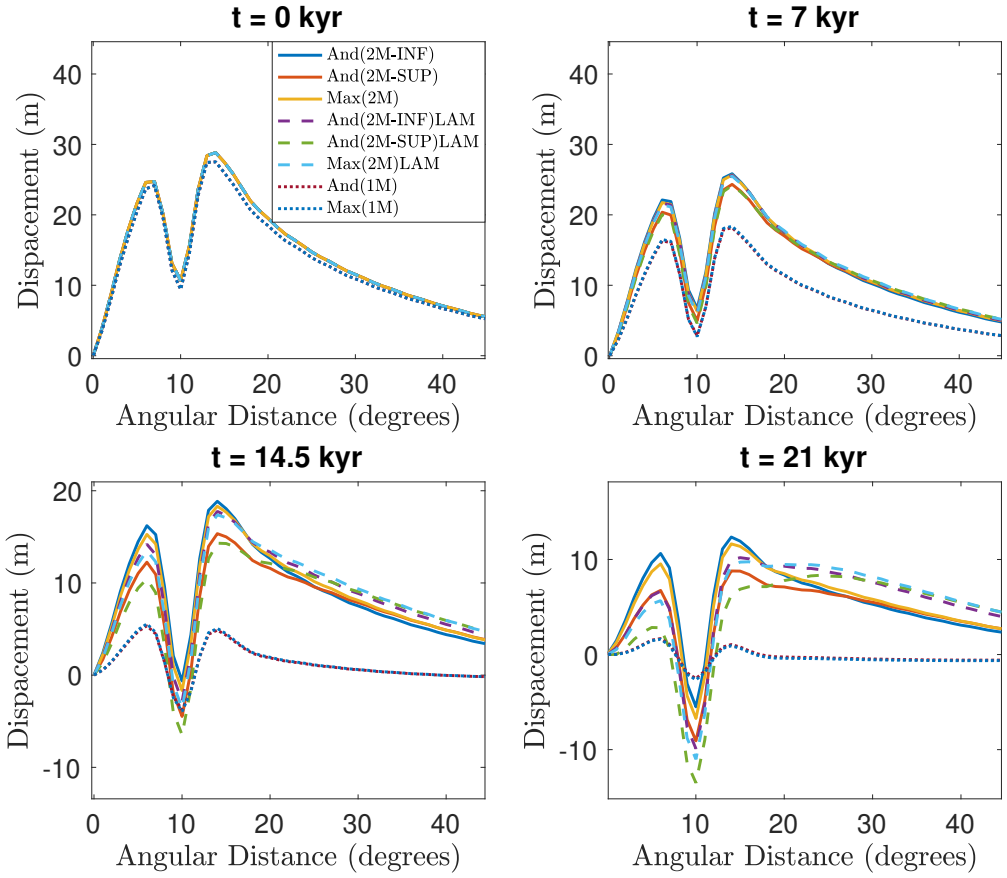

Figure 5.20: **Horizontal Displacement**: in the four plots the horizontal displacement is reported for different times $t = 0,\ 7,\ 14,5\ 21\ kyr$. At $t = 0\ kyr$ we can distinguish a little but significant difference in the shape of the curves computed by this and the previous experiment. Both in $t = 7\ kyr$ and $t = 14.5\ kyr$ the value of each output assume similar value, and it is difficult to discern them; at the end of the simulation the trends are still very close to each other but some differences can be observed.

we said for the vertical variation holds true even in this case, with the usual difference that the plots are smoother and the amplitudes of the displacements are smaller.

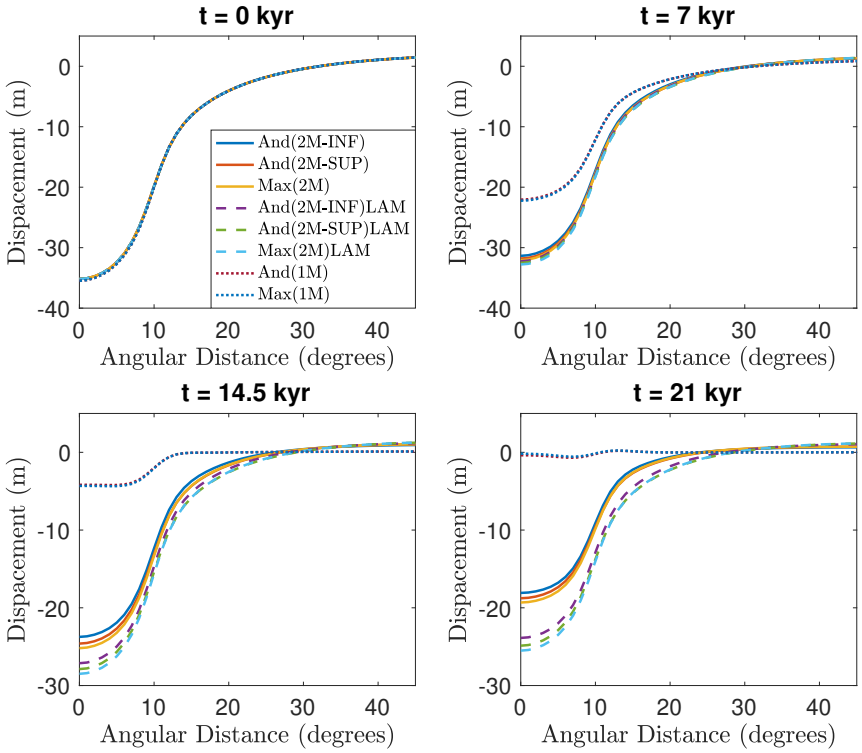

Figure 5.21: **Geoid Height Variation**: in the four plots the geoid height is reported for different times $t = 0,\ 7,\ 14.5$ and $21\ kyr$. The main features follow the one of the vertical displacement.

Velocities

In the following pages are reported the plots regarding the evolution of the displacement rates. These plots are particularly important since displacement rates are leading data in PGR.

Starting from the **vertical displacement rate** (Figure 5.22), what we can say is that its evolution reflects the one of the previous experiment (an increase in the displacement rate under the ice load, then a sudden drop when the load is removed, followed by a gradual decrease). The main difference that we can notice observing Figure 5.22 regards the values of these velocities. With respect the previous experiment, they are

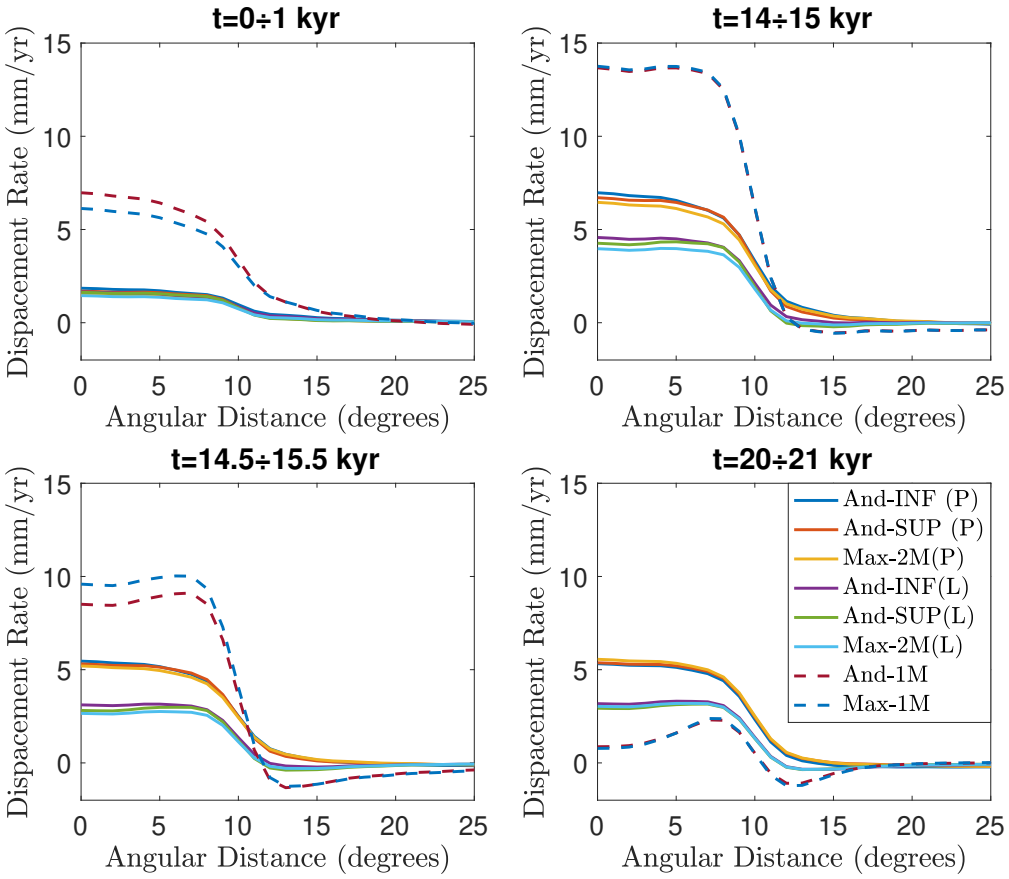

Figure 5.22: **Vertical Displacement Rate**: even in this figure four different time interval are represented. From angular distances $\alpha < 15°$, the velocity trends remain for the most part of the experiment grouped into two clusters: Peltier's and Lambeck's one.

lower, and they never exceed the value of 8 mm/yr. In the first phase, from the start of the simulation until $t = 14 \div 15$ kyr they increase from an initial value around 2 mm/yr untill, for the case of Peltier's models, ~ 7 mm/yr, and until ~ 4.5 mm/yr as regards Lambeck's models. Then, at $t = 14.5 \div 15.5$ kyr the disappearance of the ice load generates the drop in the velocity values that we observed even in the previous experiment. This time the entity of the drop is not marked as it was in the previous case (Peltier's trends decrease from ~ 7 mm/yr to ~ 5 mm/yr while Lambeck's from ~ 5 mm/yr to ~ 3 mm/yr. Then, until the end of the simulation, the profile remains almost unvaried. As it was mentioned in the discussion about the vertical displacements, here it appears even more clearly that the faster models are the ones with Andrade in the

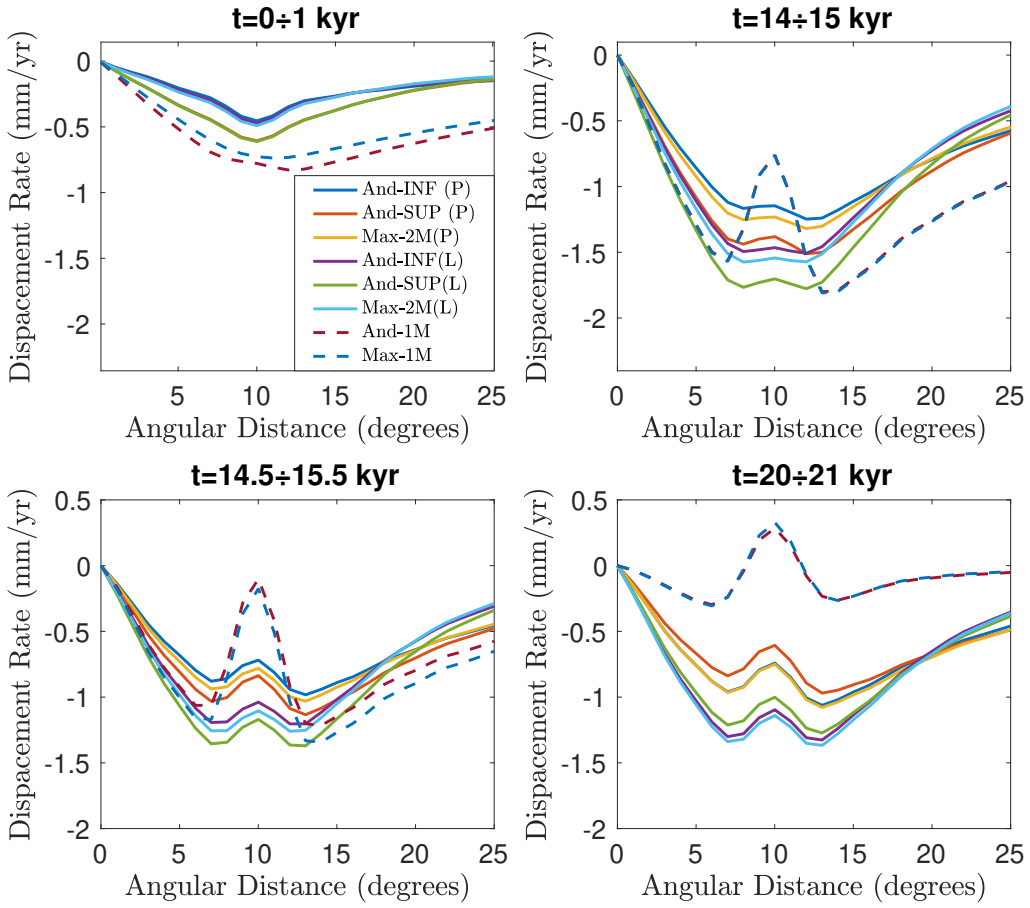

Figure 5.23: **Horizontal Displacement Rate**: in this figure we see the evolution of the vertical velocity through four different time intervals: $t = 0 \div 1$, $t = 14 \div 14$, $t = 14.5 \div 15.5$ and $t = 20 \div 21$ kyr.

lower mantle. The difference in velocity is not very significant, but however it is a fact of remarkable interest: we can conclude that, the GIA vertical displacements involving huge ice sheet is mostly controlled by the deepest mantle layers.

The **horizontal displacement rate** (Figure 5.23) is characterized, in the first part of the experiment, until $t = 14 \div 15$ kyr, by negative velocities that increase with time in the $y - axis$ negative direction and have their minimum around $\theta = 10°$ (see the first box of Figure 5.23). In the time step $t = 14.5 \div 15.5$ kyr, the disappearance of the ice-sheet modifies the shape of the velocity profile, and as we can see in the third box of Figure 5.23, the central part of the concavity raises up. Then, until the end of the simulation, the models with Maxwell in the two mantles and the ones with Andrade in

the lower mantle remain almost unchanged in this new position, while the one referring to the models with Andrade in the upper mantle increase in value toward the y axis. Basically, we can say that in this last time range, while the models And-INF(P), And-INF(L), Max-2M(P) and Max-2M(L) have a null acceleration, the ones with Andrade in the upper mantle have positive accelerations. This means that, contrary to the vertical displacement, the horizontal one seems more influenced by the rheology of the upper mantle.

As regards the **geoid height variation** (Figure 5.21), we can see that in general what we said for the vertical displacement rates holds true, with the usual difference that the profiles are smoother and the amplitudes are smaller.

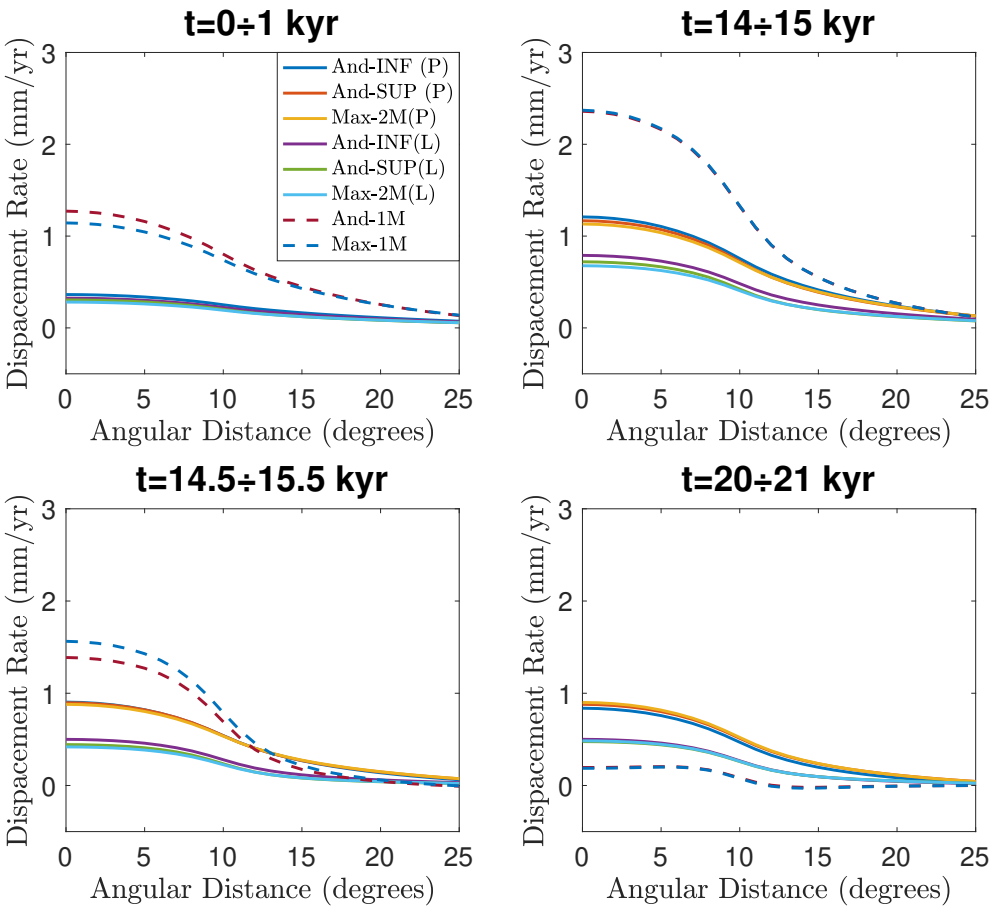

Figure 5.24: **Geoid height variation rate**:in the four plots the geoid height is reported for different times $t = 0,\ 14 \div 15,\ 14.5 \div 15.5$ and $20 \div 21$ *kyr*. The main features follow the one of the vertical displacement.

5.4 Experiment 4: present day ice melting

In the previous sections we have solved the problem of understanding which are the optimal time and position for observing the effects of a transient rheology for a deglaciation occurred in the past. In this last section we will investigate if also present day climate change is able to trigger responses attributable to transient effects. To do so, we will need to change the dimension of the considered load: present day climate change acts firstly on alpine and peripheral glaciers, that due to their dimension and other external conditions, are more sensitive to temperature warming than the bulk of ice-sheet. In this section we will thus consider the following problem:

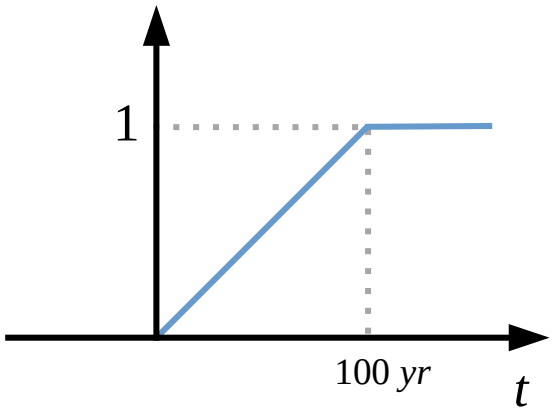

Figure 5.25: Schematic representation of the ice history used in the fourth experiment.

- **Ice-History**: thanks to a new version of `ALMA`, we will consider a ramp-shaped ice-history (Figure 5.25). The ramp describes the growth of the glacier, that from time $t = 0\ yr$ in which no ice is present, evolves until it reaches its maximum thickness for $t = 100\ yr$.

- **Earth Model**: due to the dimensions of the load, we need an Earth model with a better description of the upper layers. To do so without invoking a detailed Earth model with many layers, we will consider a 3-layer Earth model in which the crust has a thickness of 30 km, the mantle is uniform and reaches a depth of 3480 km, and then the core is fluid and inviscid. Basically, we are considering model GS00 with a thinner lithosphere. Parameters of this model are reported in Table 5.4.

Here we remark that, for the case of Burgers, the rigidity μ_1 and the viscosity η_1 have the valeus shown in Table 5.4, while $\mu_2 = 0.3 \cdot \mu_1$ and $\eta_2 = 0.1 \cdot \eta_1$.

- **Ice-Load**: the purpose of this experiment is simulate the response to present day ice melting, that involves mainly alpine and peripherical glaciers. For this reason, since we continue using the disc-shaped model, the ice load angular extension is reduced to $\theta = 1°$, that represents a surface extension of 38 820 km^2. This is a good representation of alpine glaciers, that by definition do not exceed the dimensions of 50 000 km^2.

- **Rheology**: we will take into consideration four different rheology for the mantle: Elastic, Maxwell, Burgers, and Andrade. All this rheological models are described in Chapter 1.

Radius $m \cdot 10^3$	**Density** $kg/m^3 \cdot 10^3$	**Rigidity** $Pa \cdot 10^{11}$	**Viscosity** $Pa \cdot s$	**Rheology**
6371	3.300	0.28	10^{21}	E
6341	4.518	1.45	10^{21}	M/A/E/B
3480	10.977	0	0	F

Table 5.3: Parameters for the modified GS00 model. Differently from the previous case, here the lithosphere is thinner, only 30 km thick. In the last column "E", "M", "F", "A" and "B" indicate to which kind of rheological behaviour attribute the parameters (Elastic, Maxwell, Fluid, Andrade and Burgers).

First of all, using `ALMA`, I obtained the LLNs until the harmonic degree $n = 256$ for all the four Earth model described above; then, I performed convolutions Eqs. (4.44), (4.46) and (4.45) to obtain the displacements. I plotted the results with `MATLAB`. As done before, using `MATLAB` I also computed the displacement rates. In this experiment I choose to represent data in a different way: the ice load is small, so we do not expect to recognize its effects at great angular distances. Since we are interested to recognize the time interval in which the effects of the transients start to differ from the ones produced by non-transient rheologies, I opted for plots in which, at a given angular distance θ, the displacement is shown as a function of time. I considered $\theta = 0°,\ 1°,\ 2°$.

The result I obtained from the convolutions referred however to a deformation due to the formation or to the growth of a glacier, while in the actual case we would obtain

the deformation due to deglaciation process. Rather than modifying the convolution and making it able to consider an ice-history of the type $1 - ramp(t)$, I simply multiply the output by -1. So, differently from before, at the start of the simulation the displacement is zero, while in the previous case we where able to plot the initial depression.

In the first three figures, vertical, horizontal and geoid displacement are shown, while in the other three we see the velocities.

Figure 5.26 represents the **vertical displacement**. The three boxes represent the angular distances $\theta = 0°,\ 1°$, and $2°$. The higher values of displacement are reached at $\theta = 0°$, and by moving away from the centre of the glacier the amplitude of the displacements decreases. However, in all the three cases, the trends of the displacement are the same: the model with a Burgers rheology in the mantle produces the larger displacements, that have their maximum at $t = 100\ yr$. Immediately below, we have Andrade, and then Maxwell and the Elastic case. The rheology that accounts for transient effects (Burgers and Andrade) shows a convexity while the other two have a linear trend. As we can see, starting from $t = 40\ yr$ Burger and Andrade models are well distinguishable from each other and from the elastic and Maxwell's output. Compared to the difference between Andrade and Burgers, the outputs computed with a Maxwell rheology and an elastic one remain smaller until the end of the simulation, at $t = 100\ yr$. This first figure tells us that, if our glacier started losing mass in the 80's, at present day we should be able to discern the presence (or not) of a transient in the mantle. Of course this is a rough estimate, a more detailed analysis should exploit as more as possible the data available about the ice melting, to model a more accurate deglaciation time history, but these experiments give us a first indication about the time-scales involved.

The **horizontal displacement** for $\theta = 0°,\ 1°$, and $2°$ is shown in Figure 5.27. Of course, under the centre of the load, $\theta = 0°$, no horizontal displacements take place for symmetry reasons. At the load boundary, for $\theta = 1°$, the highest values of displacement are those of the models that consider an Elastic or Maxwell's rheology in the mantle, while Andrade and Burgers produce lower results. The situation is reversed at $\theta = 2°$. Recalling the shape of the horizontal displacements saw in previous experiment, we know that in $\theta = 1°$ we are seeing a minimum, while $\theta = 2°$ is a point taken at the exterior the load, and we can expect that it is a point near the one in which we have one of the two characteristic maxima. It is interesting to notice that, according to the plot, the difference between the maximum and the minimum have a larger size in the case of

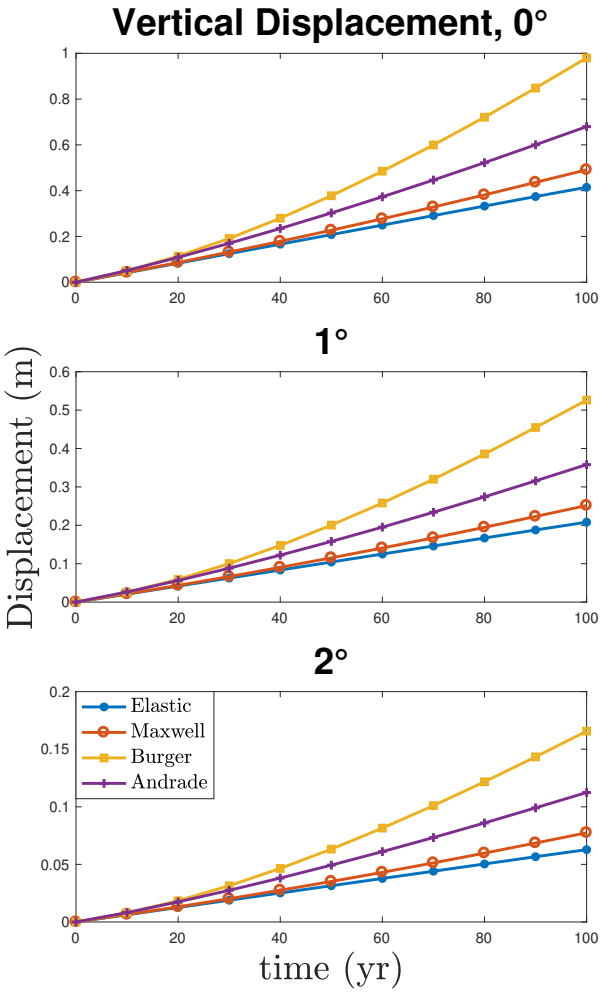

Figure 5.26: **Vertical Displacement**: in the three boxes we can see the computed displacement at $\theta = 0°,\ 1°$ and $2°$ as a function of time. The four curves represent the responses of the considered models. The number above each plots represents angular distances $\theta = 0°,\ 1°,\ 2°$ from the centre of the load.

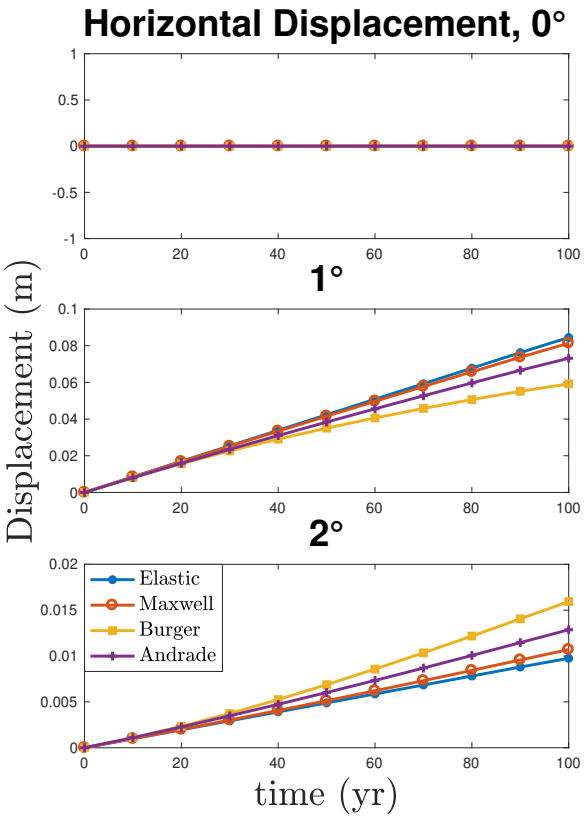

Figure 5.27: **Horizontal Displacement**: as above, in the three boxes, we can see the expected displacements for $\theta = 0°,\ 1°\ 2°$ as a function of time.

models that do not consider the transient in the mantle.

The **geoid displacement** (Figure 5.28) follows the same trends of the vertical displacement, with the difference that the amplitudes are smaller.

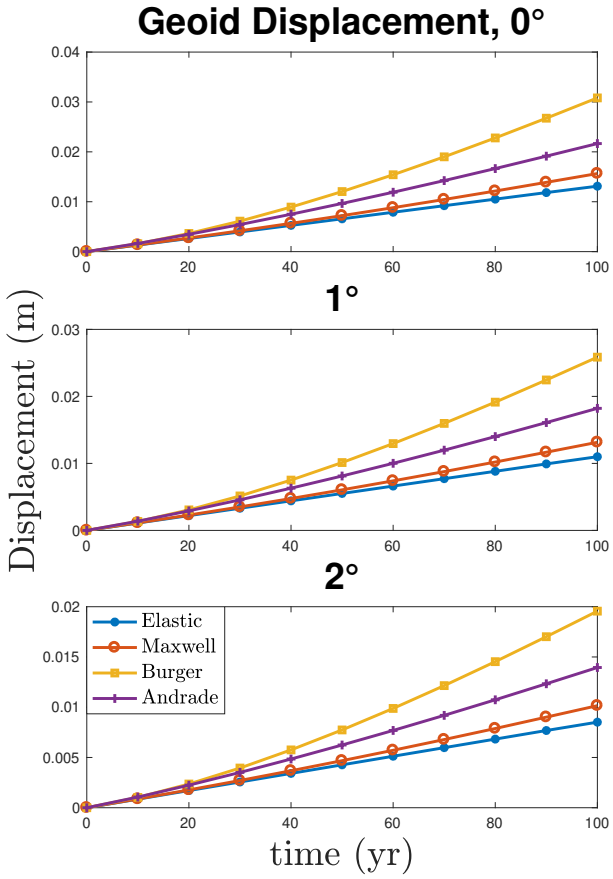

Figure 5.28: **Geoid Displacement**: the geoid displacements are shown as a function of time for the angular distances $\theta = 0°, 1°$ and $2°$. The four trends refer to the output relative to different models that account respectively for Elastic, Maxwell, Burger and Andrade rheology in the mantle. The profiles retraces the ones of the vertical displacements.

The rates reflects what we have just seen in the displacement plots. Regarding the **vertical velocities** (Figure 5.29), the highest values are reached by the models that assume a Burger's rheology and an Andrade's one in the mantle, with values around 13 and 8 mm/yr respectively, at $t = 100\ yr$. The velocities obtained with these two models show a progressive deceleration, while the Maxwell model shows a linear behaviour and the elastic response rate remains constant during the whole simulation. The velocities seems to decrease with increasing angular distance from the centre of the load.

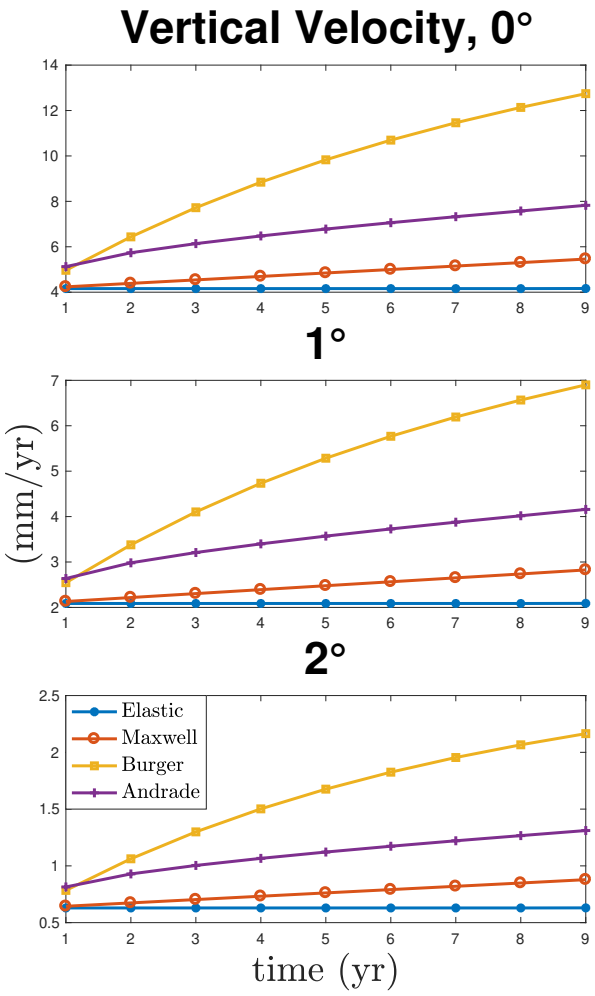

Figure 5.29: **Vertical Displacement Rate**: the rates are shown as a function of time for the angular distances $\theta = 0°, 1°$ and $2°$. In the title of each box, the number indicates the angular distance. The four trends refer to the output relative to different models described in the legend.

The **horizontal velocities** (Figure 5.30) show a particular trend. Of course at $\theta = 0°$ the velocity vanishes by symmetry, while at $\theta = 1°$, except for the elastic model, the other three have a decreasing trend. The Burgers curve seems to decelerate in the last phase of the simulation. On the contrary, at $\theta = 2°$ transient models seems to accelerate. These particular profiles suggest that the horizontal displacement is assuming its characteristic shape, with the minimum at $\theta = 1°$, at the boundary of the ice load, and the two maxima at its sides.

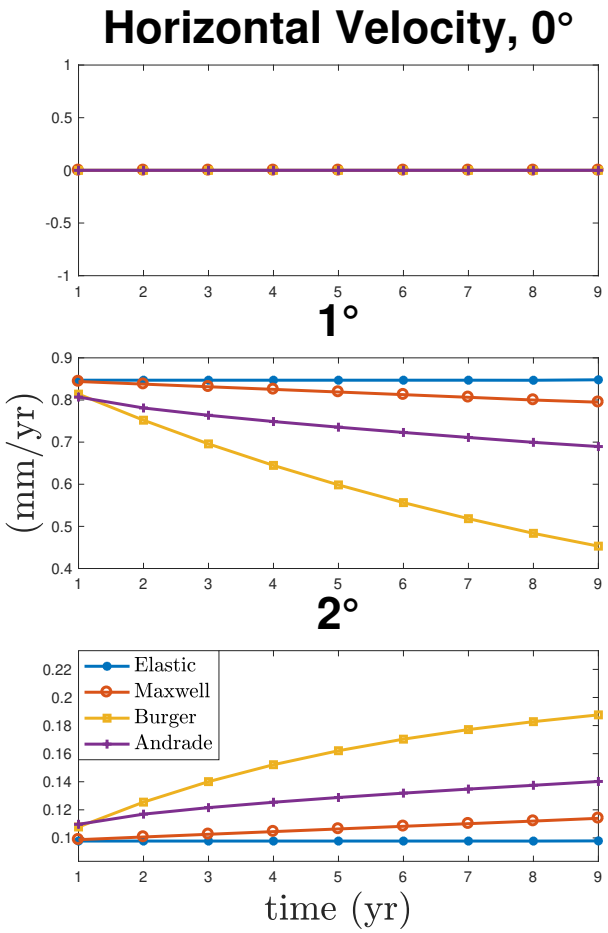

Figure 5.30: **Horizontal Displacement Rate**; the rates are shown as a function of time for the angular distances $\theta = 0°, 1°$ and $2°$. The four trends refer to the output relative to different models that account respectively for Elastic, Maxwell, Burgers and Andrade rheology in the mantle.

Even in this case the **geoid displacement rates** (Figure 5.31) follow the trend of

the vertical rates. The usual differences are in the magnitude of the velocities. The higher values are reached at $\theta = 0°$ and from the Burger's body model (0.4 m/yr at $t = 100\ yr$. Immediatly below we have Andrade's model: 0.25 m/yr at $t = 100\ yr$.

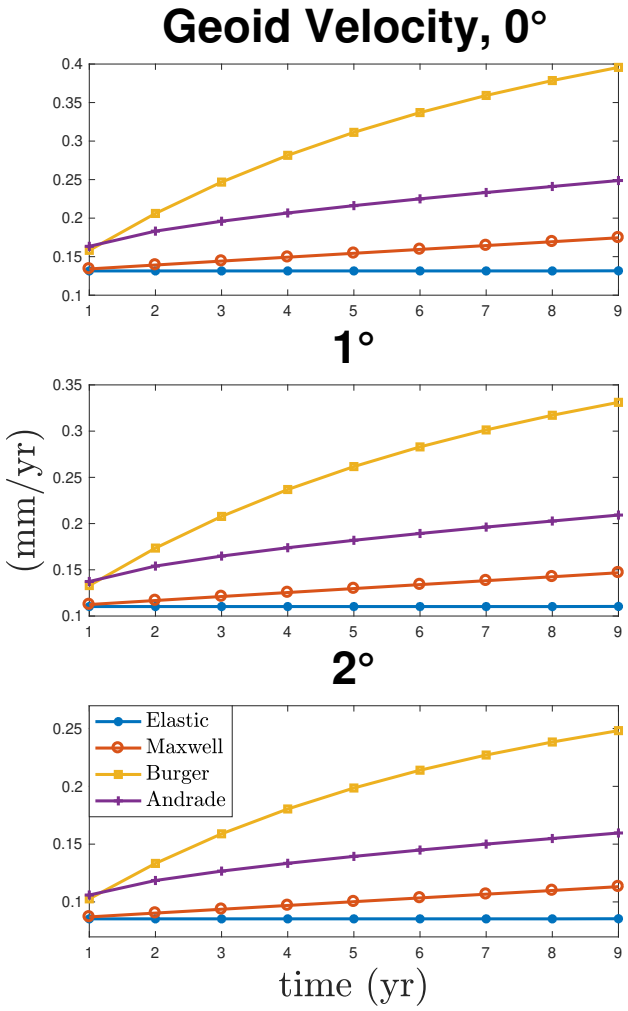

Figure 5.31: **Geoid Displacement Rate**: in this figure the geoid dispacement rates are shown as a function of time for the angular distances $\theta = 0°, 1°$ and $2°$. The four trends refer to the output relative to different models that account respectively for Elastic, Maxwell, Burger and Andrade rheology in the mantle.

Chapter 6

Conclusions

In this final chapter I wish to recall the most important results discussed in this thesis. After the first introductory chapter in which the main rheological laws were presented, we have introduced the Love numbers formalism and applied it to the surface load problem. Then, we had all the necessary ingredients to compute, once chosen a suitable ice-history, the expected displacement (and relative rates) produced by several Earth models. We considered both experiments "in the past", with the aim of understanding when past deglaciation caused deformation trends in which the transient component was distinguishable from other Earth's models with steady-state rheologies, and experiments " in the future ", to understand when present day climate change may be able to produce measurable displacement attributable to the presence of a transient in the Earth's behaviour.

We started with three experiments "in the past": the first had the simplest conditions (Heaviside ice-history, 3-layer Earth Model), from which we were however able to understand that:

- The model that accounts for an Andrade's transient in the mantle produces larger vertical, horizontal, and geoid displacement rates than the one in which we consider a Maxwell rheology;
- The horizontal displacement has a particular shape, with a minimum nearby the ice-sheet boundary and two maxima at its sides. For symmetry reason, the horizontal displacement vanishes at angular distances $\theta = 0°$, and $\theta = 180°$.

- The geoid displacement profile can be described as a smoother version of the vertical displacement profile, with smaller magnitude.

- In this experiment, the best time to distinguish the effects of the transient from those of a steady-state rheology is immediately after the disappearance of the ice-load, while the best position is the point on the Earth's surface under the centre of the disc-shaped ice-sheet.

The first three statements remained true also for the following experiments.

The second experiment exploited the same Earth model but this time the ice-history was more realistic, and in place of accounting for a unique step in which the ice suddenly disappeared, it considered a gradual step-decrease of the ice. The conclusion of this experiment confirmed the one of the previous, and added a particular: when the ice melting is gradual, the displacement rates change in value during the simulation: the velocities increase until the time in which we remove totally the ice-load. At that moment they undergo to a sudden drop, after which they decrease further. This fact characterizes even the following experiments. Even in this case the best moment in which possible transient effects are clearly osservable is when the ice disappears totally, but if before this occurred at the beginning of the simulation, here we must wait for $\simeq 14.5 \div 15.5\ kyr$.

The third experiment accounted for a two-layered mantle. We considered both a "Peltier's" layering, with viscosities of the upper and lower mantle respectively 10^{21} and $2{\cdot}10^{21}\ Pa{\cdot}s$, and a "Lambeck's" layering, were the two viscosities were 10^{21} and $10^{22}\ Pa{\cdot}s$. The two-layer mantle allowed us also to investigate if the presence of the transient only in a portion of the mantle (the upper or the lower) had remarkable consequences. The main results we found out were:

- Considering a layer (the lower) in which the viscosity is higher slows down displacement rates;

- The general behaviour of the displacement rates follows the one observed in the second experiment: a first phase of increasing velocities, then the drop at the ice disappearance moment, and then a slow reduction;

- Vertical displacements are more sensitive to the rheology of the lower mantle, while horizontal displacements to the one of the upper mantle. This feature finds a qualitative explanation considering that horizontal displacements are linked especially

with horizontal fluxes of the Earth's interior material, which for geometric reasons have more freedom of movement with respect vertical fluxes, that have a restricted area corresponding to the thickness of the mantle.

- The best moment in which the effects of the transient can be observed was, even here, at the disappearance of the ice, between 14.5 and 15.5 kyr ago, at angular distances $\theta < 8°$ for vertical and geoid displacement. The horizontal ones shows greater differences between Andrade's models and the Maxwell's one at $t = 21$ kyr and in the angular distances around the minimum and the two maxima.

Considering the last simulation the more suitable for answering the fundamental question of this thesis, we can say that the best time at which the presence of a possible transient can be observed in the profile of the vertical displacement occurred more or less between 14.5 and 15.5 kyr ago. However, collecting the information deduced by previous experiments, I think that, in general, the effects of a transient rheology produces the greater differences, in term of expected displacement, with respect to a steady-state rheology, when sudden changes happen to the load. Indeed I do not think that it is just a coincidence that the best times at which the transient can be observed happened always at the disappearance of the ice-load. Hence, the best situations in which we can try to find a possible transient are those in which the ice-load underwent to fast and sudden variations.

Regarding the last experiment, our purpose was understanding when actual climate change will be able to produce deformations attributable to the presence of a rheological transient behaviour in the Earth. We assumed a ramp ice-history, in which the ice melted linearly in 100 yr. This ice model is even more detailed than the previous ones. We saw that the expected displacements with the greater magnitudes were the vertical ones: in a century, considering the Earth model of Table 5.4 , an ice-sheet of angular amplitude of 1° can produce an uplifting of the Earth's surface of 1 m under its centre (considering a Burger's rheology in the mantle). Observing the data of the vertical displacement, we can say that after 40 yr from the start of the melting, the four curves representing Earth's models with Andrade, Burgers, Maxwell and an elastic rheology in the mantle start producing sufficiently different expected displacement. Beyond 50 yr the curves of the two steady-state rheologies (Maxwell and linear elastic) are well distinguishable from the one of Burgers and Andrade's. Even Burgers and Andrade's curves are discernible

after 50 yr. For the horizontal displacement, we should wait a little more to distinguish the various trends: a time of 60 yr seems however enough for discerning between Burgers trend, Andrade's trend and the steady-state rheologies trend (Maxwell and elastic rheology).

Considering the rate of the actual melting of alpine glaciers and ice-caps, in the next decades, we should be able to recognize patterns potentially attributable to transient effects in the Earth's surface deformation data.

Ringraziamenti

In queste ultime righe vorrei ringraziare il Prof. G. Spada che, con estrema disponibilità e gentilezza, mi ha seguito e guidato nella stesura di questa tesi. Un grazie anche al Dott. D. Melini, che con altrettanta disponibilità mi ha fornito le ultime versioni di `ALMA` con cui condurre gli esperimenti finali, seguendo questo lavoro fino alla fine.

Bibliography

[1] G. Spada: Glacial isostatic adjustment and contemporary sea level rise; an overview - *Survey Geophysics, 38:153–185*, DOI 10.1007/s10712-016-9379-x (2017).

[2] P. L. Whitehouse: Glacial Isostatic Adjustment modelling: historical perspectives, recent advances, and future directions - *Earth Surf. Dynam. Discuss.*, https://doi.org/10.5194/esurf-2018-6 (2018).

[3] G. Ranalli: Rheology of the Earth - *Springer* (1995).

[4] D. K. Dysthe et al.: Universal Scaling in Transient Creep - *Physics of Geological Processes, 89, number 24*, DOI: 10.1103/PhysRevLett.89.246102 (2002).

[5] F. Douchet, P. Duval: Andrade Creep Revisited - *International Journal of Materials Resarch*, https://doi.org/10.3139/146.110189 (2009).

[6] D. L. Turcotte and G. Schubert: Geodynamics - *Cambridge University Press* (1982).

[7] M. E. Belardinellii: Dispense del corso "Tettonofisica" (Reologia dell'interno della Terra) - *Università di Bologna* (A.A 2020/2021).

[8] M. Dragoni: Dispense del corso "Fisica della Terra" - *Università di Bologna* (A.A. 2019/2020).

[9] G.Spada: Dispense del corso "Interazioni nel sistema Terra" - *Università di Bologna* (A.A. 2020/2021).

[10] J. L. Schiff: The Laplace transform: theory and applications - *Springer Science & Business* (1999).

[11] K. H. Lundberg, H. R. Miller, D. L. Trumper: Initial conditions, generalized functions, and the Laplace transform - troubles at the origin - *IEEE Control Systems Magazine, 27(1), 22-35* (2007).

[12] C. Andrade: On the Viscous Flow in Metals, and Allied Phenomena - *Physics Research Scholar, University College, London* (1910).

[13] M. Dragoni: Dispense del corso "Sismologia Teorica" - *Università di Bologna* (A.A. 2019/2020).

[14] M. Reiner: The Deborah Number - *Physics Today, 17, 62*, DOI:10.1063/1.3051374 (1964).

[15] N. A. Haskell: The Motion of a Viscous Fluid Under a Surface Load - *Physics 6, 265-269*, https://doi.org/10.1063/1.1745329 (1935).

[16] J. Weertman: Transient mantle rheology - *Nature, 318 19/26* (December 1985).

[17] W. R. Peltier, R. A . Drummond and A . M. Tushingham: Postglacial rebound and transient lower mantle rheology - *Geophysical Journal Review, 87,79 - 116* (1986).

[18] W. R. Peltier, P. Wu, D. A. Yuen: The Viscosities of the Earth's Mantle - *Geodynamics Series*, https://doi.org/10.1029/GD004p0059 (1981).

[19] K. Lambeck et al.: The North American Late Wisconsin ice sheet and mantle viscosity from glacial rebound analyses - *Quaternary Science Reviews, 58, 172-210*, http://dx.doi.org/10.1016/j.quascirev.2016.11.033 (2017).

[20] W. R. Peltier: New constraints on transient lower mantle rheology and internal mantle buoyancy from glacial rebound data - *Nature, 318* (1985).

[21] S. Karato: Rheology of the Earth's mantle: A historical review - *Gondwana Research, Elsevier*, doi:10.1016/j.gr.2010.03.004 (2010).

[22] L. C. Lee, S. J. S. Morris: Anelasticity and grain boundary sliding - *Proc. R. Soc. A, 466, 2651–2671*, doi:10.1098/rspa.2009.0624 (2010).

[23] J. C. Castillo-Rogez, et al.: The tidal history of Iapetus: Spin dynamics in the light of a refined dissipation model - *Journal of Geophysical Research, 116, E09008*, doi:10.1029/2010JE003664 (2011).

[24] F. Mainardi: Fractional calculus and waves in linear viscoelasticity: an introduction to mathematical models - *World Scientific* (2010).

[25] A. E. H. Love: The yielding of the earth to disturbing forces - *Proc. R. Soc. Lond. A*, http://doi.org/10.1098/rspa.1909.0008 (1909).

[26] Wikipedia contributors: Love number - *Wikipedia, The Free Encyclopedia*, https://en.wikipedia.org/w/index.php?title=Love_number&oldid=1030819914 (accessed August 19, 2021).

[27] W. E. Farrell: Deformation of the Earth by surface loads - *Reviews of Geophysics* https://doi.org/10.1029/RG010i003p00761 (1972).

[28] W. Torge: Geodesy, chapter 5 - *Walter de Gruyter, Berlin* (Second Edition, 1991).

[29] W. R. Peltier: The impulse response of a Maxwell earth - *Rev. Geophys. Space Phys., 12, 649–669* (1974).

[30] P. Wu and W. R. Peltier: Viscous gravitational relaxation - *J. Geophys. Res.* (1981).

[31] W. T. Kelvin: Mathematical and Physics Papers - *University Press, vol. 3* (1890).

[32] G. Spada: ALMA, a Fortran program for computing the viscoelastic Love numbers of a spherically symmetric planet - *Computers & Geosciences 34 667–687*, doi:10.1016/j.cageo.2007.12.001 (2008).

[33] G. Spada and L. Boschi: Using the Post–Widder formula to compute the Earth's viscoelastic Love numbers - *Geophys. J. Int. 166, 309–321*, doi: 10.1111/j.1365-246X.2006.02995.x (2006).

[34] R. Sabadini, D.A. Yuen, and E. Boschi: Polar wandering and the forces responses of a rotating, multilayered, viscoelastic planet - *J. Geophys. Res., 87, 2885–2903* (1982).

[35] E. L. Post: Generalized differentiation - *Trans. Amer. Math. Soc., 32, 723–781* (1930).

[36] D. V. Widder: The inversion of the Laplace integral and the related moment problem - *Transactions of the American Mathematical Society Translations 36, 107–200* (1934).

[37] D. V. Widder: The Laplace Transform - *Princeton University Press, Princeton, NJ, 406 pp* (1946).

[38] D. P. Gaver: Observing stochastic processes and approximate transform inversion - *Oper. Res., 14, 444–459* (1966).

[39] J. Abate and P. P. Valkò: Multi-precision Laplace transform inversion - *J. Numer. Meth. Engng., 60, 979–993* (2004).

[40] B. G. Bills, T. S. James: Polar motion of a viscoelastic Earth due to glacial cycle mass loading - *Journal of Geophysical Research 102, 7579–7602* (1997).

[41] L. L. A. Vermeersen, R. Sabadini: A new class of stratified viscoelastic models by analytical techniques - *Geophysical Journal International 129, 531–570* (1997).

[42] L. L. A. Vermeersen, R. Sabadini, G. Spada: Analytical visco-elastic relaxation models - *Geophysical Research Letters 23, 697–700* (1996).

[43] G. Spada et al.: Effects on post-glacial rebound from the hard rheology of the transition zone - *Geophysical Journal International 109, 683–700* (1992).

[44] I. M. Longman: A Green's function for determining the deformation of the earth under surface mass loads - *J. Geophys.Res.* (1962).

[45] J. X. Mitrovica and W. R. Peltier: On postglacial geoid subsidence over the equatorial oceans - *Journal of Geophysics Research, 96, 20053-20071* (1991).

[46] G. Spada and P. Stocchi: The Sea Level Equation: Theory and numerical examples - *Aracne* (2006).

[47] E. Suess: Face of the Earth - *Clarendon Press, Oxford* (1906).

[48] K. Lambeck, C. Smither, P. Johnston: Sea–level change, glacial rebound and mantle viscosity for northern Europe - *Geophys. J. Int., 134, 102–144*, doi:j.1365-246x.1998.00541.x (1998).

[49] A. S. Dyke et al.: The Laurentide and Innuitian ice sheets during the Last Glacial Maximum - *Quaternary Science Reviews, 21, Issues 1–3*, https://doi.org/10.1016/S0277-3791(01)00095-6 (2002).

[50] C. L. Hill: Geologic Framework and Glaciation of the Central Area, *Boise State University Scholar Works, 1-1-2006; Boise, Idaho* (2006).